An investigation of the sensitivity of LHC dark matter searches at $\sqrt{s} = 13$ TeV to dark Higgs models

Yingpu Xiahou

School of Physics

University of Bristol

Supervisors:

Henning Flaecher

Bjoern Penning

Word Count:

13555

November 2018

A dissertation submitted to the University of Bristol in accordance with the requirements of the degree of Msc(R) in the Faculty of Science, School of Physics, University of Bristol.

Declaration of Authorship

I declare that the work in this dissertation was carried out in accordance with the requirements of the University's Regulations and Code of Practice for Research Degree Programmes and that it has not been submitted for any other academic award. Except where indicated by specific reference in the text, the work is the candidate's own work. Work done in collaboration with, or with the assistance of, others, is indicated as such. Any views expressed in the dissertation are those of the author.

SIGNED: ..... DATE:.....

Acknowledgements

I am very thankful to the University of Bristol High Energy Physics Group for giving me the opportunity to work on dark matter collider searches. Thanks to my supervisors, Bjoern Penning and Henning Flaecher, for introducing me to the High Energy Physics and for their encouragements and many useful discussions through my study. Thanks to everyone else in the CMS UK SUSY/DM group.

Thanks to my parents, Daohua Li and Wei Xiahou, for financial support and for their encouragements.

Yingpu Xiahou

Abstract

The 'Higgs Portal Dark Matter' model is introduced in this thesis. A dark Higgs boson is responsible for generating masses for dark sector particles. Since this thesis focuses on dark Higgs decaying to a pair of b-tagged jets, the experimental signature is one boosted double b-tagged jet with large missing energy. Two different and complementary search methods have been investigated in this thesis: the large-radius mono-jet search and the more "generic" missing energy + jets search using the CMS α_T analysis. The former is carried out by the ATLAS experiment, searching for a boosted double b-tagged large-radius jet with large missing energy. The latter is based on a CMS search, searching for resolved b-jets with specific kinematic variables and large missing energy.

In the recast of the large-radius search, all signal events are generated by **MadGraph5_aMC@NLO v2.3.3** in the two coupling scenarios presented in Section 3.2. **Pythia 8** and **Rivet v2.5.2** are used for showering and event selection. Finally, **HiggsCombineTool** from **CMSSW_8_1_0** is applied to calculate the expected exclusion upper limits at 95% confidence level (CL) with an integrated luminosity of 35.9 fb^{-1}. The recast of the large-radius search shows that signals with couplings according to the LHC recommendation can obtain significant exclusion limits. When the mass of the dark Higgs (m_s) is 50, 70 and 90 GeV, the mass of the Z' ($m_{Z'}$) up to 1800, 2000 and 1800 GeV are respectively excluded. The recast of the large-radius search shows that signals with couplings set to fulfil the DM relic abundance constraint can obtain significant exclusion limits. For m_s = 50, 70 and 90 GeV, $m_{Z'}$ up to 3300, 3450 and 3500 GeV are respectively excluded.

In the reinterpretation of the CMS α_T search, all signal events are generated by **MadGraph5_aMC@NLO v2.3.3** using the same coupling scenarios as the large-radius search recast. To estimate backgrounds in this reinterpretation, we use the data recorded by the CMS experiment in 2016 together with the estimated background numbers provided in Ref. [12]. **Pythia 8** and **Rivet v2.5.2** are used for showering and event selection. We use the same event selection as in Ref. [12]. As the dataset in Ref. [12] is binned in 224 bins, we select the most sensitive ones for our analysis using the Asimov Test. Finally, **HiggsCombineTool** from **CMSSW_8_1_0** is again applied here to calculate the expected and observed sensitivities at 95% CL with an integrated luminosity of 35.9 fb^{-1} based on the selected most sensitive bins. The reinterpretation of the CMS α_T search shows that signals with couplings according to the LHC recommendation cannot obtain significant exclusion limits. However, the reinterpretation of the CMS α_T search shows that signals with couplings set to fulfil the DM relic abundance constraint can obtain significant exclusion limits. For m_s = 50, 70 and 90 GeV, $m_{Z'}$ up to 3600, 3700 and 3700 GeV are respectively excluded.

Both the recast of the large-radius search and the reinterpretation of the CMS α_T search give new experimental sensitivities to dark matter searches through the 'Higgs Portal Dark Matter' model.

Contents

1 Introduction **18**
1.1 The evidence of dark matter . . . 18
1.2 Techniques of DM detection . . . 20
1.3 Current collider dark matter production review: mono-jet and mono-V productions . . . 21
1.3.1 mono-jet and mono-V productions . . . 22
1.3.2 Event selections and background estimation . . . 23
1.3.3 Results . . . 24
1.4 Thesis outline . . . 27

2 Standard Model and 'Higgs Portal DM' model **28**
2.1 Introduction to Standard Model . . . 28
2.1.1 Cross-section and decay rate . . . 29
2.1.2 Local gauge symmetry . . . 30
2.2 The Higgs Mechanism . . . 31
2.2.1 Motivation . . . 31
2.2.2 Spontaneous Symmetry Breaking . . . 32
2.3 Introduction to 'Higgs Portal DM' model . . . 33

3 Dark Higgs searches at the LHC **36**
3.1 Overview of ATLAS and CMS detectors . . . 36
3.2 Signal generation . . . 38
3.2.1 Coupling scenario in consistence with LHC collaborations . . . 38
3.2.2 Coupling scenario considering the DM relic abundance constraint from the universe . . . 39
3.2.3 Signal events with coupling scenario considering the DM relic abundance constraint from the universe . . . 40

4 Dark Higgs search with large-radius jets **42**
4.1 Interpretation of large-radius jets analysis . . . 42
4.1.1 Expected main backgrounds . . . 43
4.1.2 Event selection . . . 44
4.2 Validation . . . 46
4.2.1 Comparison with ATLAS analysis . . . 46
4.2.2 Comparison with DESY analysis . . . 47
4.3 Results . . . 48
4.3.1 Scaling to 35.9 fb^{-1} . . . 48
4.3.2 Higgs mass window optimisations . . . 49
4.3.3 Expected signal and background yields . . . 51
4.3.4 Exclusion limits . . . 53

5 Dark Higgs search with jets and MET (α_T) analysis **60**
5.1 Interpretation of the α_T analysis . . . 61
5.1.1 Event selections . . . 61
5.2 Validation . . . 63
5.2.1 Cutflow tables . . . 64
5.2.2 Kinematic distributions . . . 67
5.3 Results . . . 68
5.3.1 Expected signal yields . . . 68

5.3.2 Exclusion limits 71

6 Discussion **77**
6.1 Large-radius jet analysis comparison 77
6.2 α_T analysis comparison 78

7 Conclusion **80**

References **82**

Appendices **87**

A Exclusion limits at fixed m_{DM} for different signal samples according to the large-radius mono-jet search **88**

B Exclusion limits at fixed m_{DM} for different signal samples according to the α_T multi-jet search **94**

List of Figures

1.1 The rotation curve of galaxy M33. Figure taken from [19]. 19

1.2 BulletCluster. The colour scale indicates the distribution of visible matter as observed with X-ray data and the green lines follow the distribution of all gravitating matter. Figure taken from [18]. 20

1.3 Annual modulation signature from DAMA, as shown in [20]. 21

1.4 Mono-jet and mono-V production diagrams for a spin-0 mediator, as shown in [25]. 22

1.5 Mono-jet and mono-V production diagrams for a spin-1 mediator, as shown in [25]. 23

1.6 Observed MET distribution in mono-jet and mono-V signal regions with an integrated luminosity of 35.9 fb^{-1}. Left: the mono-jet search. Right: the mono-V search. MET $>$ 1250 (750) GeV for the mono-jet (mono-V) search has been applied for the last bin. Two signal events are drawn here: one from 125 GeV Higgs boson decaying to invisible particles and the other from 2 TeV axial-vector mediator decaying to 1 GeV dark matter particles. Ratios of data with pre-fit background distributions (red points) and postfit expected background distributions (blue points) are performed. The gray bands refer uncertainties. The difference between data and prediction over the sum of uncertainties is also shown at the bottom. Figure taken from [24]. . 25

1.7 Exclusion limits at 95% CL with an integrated luminosity of 35.9 fb^{-1}. Left: the vector mediator. Right: the axial-vector mediator. The solid (dotted) red (blue) line refers the observed (expected) exclusion. One standard deviation has been drawn due to theoretical uncertainties from observed exclusion and statistical and systematic uncertainties from expected exclusion. The Planck satellite experiment constraints [35] are shown with dark blue lines. Figure taken from [24]. 26

1.8 The cross-section ratio plot at 95% CL is shown with an integrated luminosity of 35.9 fb^{-1}. Left: the scalar mediator. The benchmark for DM particle mass in this plot is 1 GeV. The dotted black line (solid balck line) refers to the expected (observed) upper limits on cross-section ratio. The red solid line refers to the cross-section from theoretical prediction is exactly the maximum cross-section which would be allowed at 95% CL. Exclusion limits at 95% CL with an integrated luminosity of 35.9 fb^{-1}. Right: the pseudoscalar mediator. The solid (dotted) red (blue) line refers the observed (expected) exclusion. One standard deviation has been drawn due to theoretical uncertainties from observed exclusion and statistical and systematic uncertainties from expected exclusion. The Planck satellite experiment constraints [35] are shown with dark blue lines. Figure taken from [24]. 26

2.1 All the generations of elementary fermions and interaction mediators included in the Standard Model together with the Higgs boson. Figure taken from [38]. 28

2.2 Three types of Feynman diagrams together with the respective Lorentz-invariant quantities. 29

2.3 The distribution of potential energy for a complex scalar field. ϕ_1 and ϕ_2 are the real and imaginary parts of the complex scalar field. Figure taken from [39]. 33
2.4 Processes leading to missing energy signatures at the LHC. Left: a conventional mono-jet event. Right: a process leading to a mono-dark-Higgs signal. Figure taken from [1]. 34
3.1 Schematic view of the ATLAS detector as shown in [8]. 37
3.2 Schematic view of the CMS detector as shown in [10]. 37
3.3 y_x and g_x distributions under relic abundance for $m_s = 70$ GeV and $g_q = 0.25$. $g_x > 4\pi^{1/2}$ is the limitation of this process as g_x should remain perturbative. m_χ is the same as m_{DM}. Figure taken from [1]. . 39
3.4 g_x distribution under DM relic abundance for $m_s = 70$ GeV and $g_q = 0.25$. 40
4.1 Feynman diagrams for most relevant Standard Model backgrounds. Top: W, Z and diboson events leading to MET. Bottom: $t\bar{t}$ background resulting from semi-leptonic decays of top pair production. . . 43
4.2 SM background under the reconstructed large-radius jet mass distributions with an integrated luminosity of 3.2 fb^{-1}. All event selection requirements except sensitive mass windows have applied to generate this plot. The reconstructed large-radius jet mass is shown up to 280 GeV to give an overall SM background distribution. 47
4.3 SM background in the reconstructed large-radius jet mass distribution with an integrated luminosity of 35.9 fb^{-1}. All event selection requirements except sensitive mass windows have been applied to generate this plot. The reconstructed large-radius jet mass is shown up to 140 GeV as our signal sensitive region for the dark Higgs search are within this area. 49
4.4 Reconstructed large-radius jet mass distributions for signal processes with different m_s and different $m_{Z'}$ with an integrated luminosity of 35.9 fb^{-1}. Signal processes are chosen according to the Ref. [1] preference and the coupling scenarios are the same as the LHC preference [37]. 50
4.5 The expected exclusion region of the large-radius jet analysis at 95% CL with an integrated luminosity of 35.9 fb^{-1} at a centre-of-mass energy of 13 TeV. The inputs all correspond to $m_s = 50$, 70 and 90 GeV. The couplings are set according to the LHC recommendation [37]. The solid red line shows the expected upper limit and one (two) standard deviations arising from experimental uncertainties have been drawn using dashed red (purple) lines. 55
4.6 The expected exclusion region of the large-radius jet analysis at 95% CL with an integrated luminosity of 35.9 fb^{-1} at a centre-of-mass energy of 13 TeV. The inputs all correspond to $m_s = 50$, 70 and 90 GeV. The coupling g_x is chosen to fulfil the relic density constraint [2]. The solid red line shows the expected upper limit and one (two) standard deviations from experimental uncertainties have been drawn using dashed red (purple) lines. All the regions below the expected upper limits are excluded. The dashed blue line indicates the region where $g_x = (4\pi)^{1/2}$. 57
4.7 Expected 95% CL limits for $m_s = 70$ GeV with $m_{\mathrm{DM}} = 100$ and 301 GeV. The couplings are set according to the LHC recommendation [37]. The theoretical cross-section is shown as the blue solid line. 58

5.1 Diagram of the SUSY T2bb model. The diagram shows the direct production of bottom squarks. The dashed area represents a model-dependent process that can produce a pair of bottom squarks. Figure taken from [11]. 64
5.2 Comparison of distributions for (a) H_T, (b) n_b, (c) H_T^{miss}, and (d) n_{jet} between Ref. [11] and this analysis for SUSY T2bb(375,300). Before and after selection distributions for (a) H_T, (b) n_b, (c) H_T^{miss}, and (d) n_{jet} are all considered. Event selection includes $H_T > 200$ GeV, $H_T^{miss} > 130$ GeV and $n_{jet} > 2$. 67
5.3 Comparison of distributions for (a) H_T, (b) n_b, (c) H_T^{miss}, and (d) n_{jet} between Ref. [11] and this analysis for SUSY T2bb(800,50). Before and after selection distributions for (a) H_T, (b) n_b, (c) H_T^{miss}, and (d) n_{jet} are all considered. Event selection includes $H_T > 200$ GeV, $H_T^{miss} > 130$ GeV and $n_{jet} > 2$. 68
5.4 The expected exclusion region of the α_T analysis at 95% CL with an integrated luminosity of 35.9 fb^{-1} at a centre-of-mass energy of 13 TeV. The inputs all correspond to $m_s = 50$ GeV. The couplings are set according to LHC recommendations [37]. The solid red line shows the expected upper limit and one (two) standard deviations arising from experimental uncertainties have been drawn using dashed red (purple) lines. 72
5.5 Expected and observed 95% CL limits for $m_s = 70$ and 90 GeV with $m_{\mathrm{DM}} = 100$ GeV, respectively. The couplings are set according to LHC recommendations [37]. The theoretical cross-section is shown as the blue solid line. 73
5.6 The expected exclusion region of the α_T analysis at 95% CL with an integrated luminosity of 35.9 fb^{-1} at a centre-of-mass energy of 13 TeV. The inputs correspond to $m_s = 50$, 70 and 90 GeV. The coupling g_x is chosen to fulfil the relic density constraint [2]. The solid black line shows the observed upper limits. The solid red line shows the expected upper limits and one (two) standard deviations from experimental uncertainties have been drawn using dashed red (purple) lines. All the regions below the observed upper limits are excluded. The dashed blue line indicates the region where $g_x = (4\pi)^{1/2}$. 75
5.7 Expected and observed 95% CL limits for $m_s = 70$ GeV with $m_{\mathrm{DM}} = 100$ and 449 GeV. The couplings are set to fulfil the relic density constraint [2]. The theoretical cross-section is shown as the blue solid line. 76
A.1 Expected 95% CL limits for $m_s = 50$ GeV, $g_x = 1.0$ and $g_q = 0.25$ with $m_{\mathrm{DM}} = 100$ GeV. 88
A.2 Expected 95% CL limits for $m_s = 50$ GeV, $g_x = 1.0$ and $g_q = 0.25$ with $m_{\mathrm{DM}} = 301$ GeV. 89
A.3 Expected 95% CL limits for $m_s = 90$ GeV, $g_x = 1.0$ and $g_q = 0.25$ with $m_{\mathrm{DM}} = 100$ GeV. 89
A.4 Expected 95% CL limits for $m_s = 90$ GeV, $g_x = 1.0$ and $g_q = 0.25$ with $m_{\mathrm{DM}} = 276$ GeV. 90
A.5 Expected 95% CL limits for $m_s = 50$ GeV, $g_x < (4\pi)^{1/2}$ and $g_q = 0.25$ with $m_{\mathrm{DM}} = 100$ GeV. 90
A.6 Expected 95% CL limits for $m_s = 50$ GeV, $g_x < (4\pi)^{1/2}$and $g_q = 0.25$ with $m_{\mathrm{DM}} = 566$ GeV. 91

A.7 Expected 95% CL limits for $m_s = 70$ GeV, $g_x < (4\pi)^{1/2}$ and $g_q = 0.25$ with $m_{\mathrm{DM}} = 100$ GeV. 91
A.8 Expected 95% CL limits for $m_s = 70$ GeV, $g_x < (4\pi)^{1/2}$ and $g_q = 0.25$ with $m_{\mathrm{DM}} = 566$ GeV. 92
A.9 Expected 95% CL limits for $m_s = 90$ GeV, $g_x < (4\pi)^{1/2}$ and $g_q = 0.25$ with $m_{\mathrm{DM}} = 100$ GeV. 92
A.10 Expected 95% CL limits for $m_s = 90$ GeV, $g_x < (4\pi)^{1/2}$ and $g_q = 0.25$ with $m_{\mathrm{DM}} = 566$ GeV. 93
B.1 Expected and observed 95% CL limits for $m_s = 50$ GeV, $g_x = 1.0$ and $g_q = 0.25$ with $m_{\mathrm{DM}} = 100$ GeV. 94
B.2 Expected and observed 95% CL limits for $m_s = 50$ GeV, $g_x = 1.0$ and $g_q = 0.25$ with $m_{\mathrm{DM}} = 129$ GeV. 95
B.3 Expected and observed 95% CL limits for $m_s = 50$ GeV, $g_x = 1.0$ and $g_q = 0.25$ with $m_{\mathrm{DM}} = 140$ GeV. 95
B.4 Expected and observed 95% CL limits for $m_s = 50$ GeV, $g_x = 1.0$ and $g_q = 0.25$ with $m_{\mathrm{DM}} = 153$ GeV. 96
B.5 Expected and observed 95% CL limits for $m_s = 50$ GeV, $g_x < (4\pi)^{1/2}$ and $g_q = 0.25$ with $m_{\mathrm{DM}} = 100$ GeV. 96
B.6 Expected and observed 95% CL limits for $m_s = 50$ GeV, $g_x < (4\pi)^{1/2}$and $g_q = 0.25$ with $m_{\mathrm{DM}} = 449$ GeV. 97
B.7 Expected and observed 95% CL limits for $m_s = 90$ GeV, $g_x < (4\pi)^{1/2}$ and $g_q = 0.25$ with $m_{\mathrm{DM}} = 100$ GeV. 97
B.8 Expected and observed 95% CL limits for $m_s = 90$ GeV, $g_x < (4\pi)^{1/2}$ and $g_q = 0.25$ with $m_{\mathrm{DM}} = 449$ GeV. 98

List of Tables

1.1 Astroparticles for indirect dark matter searches, experiments, advantages, and challenges. Table taken from [23]. 22

3.1 The parameter ranges considered in this project with two coupling scenarios. In this table, LHC refers to the coupling scenario consistent with the LHC recommendation and Astrophysics refers to the coupling scenario considering the DM relic abundance constraint from the universe. 38

4.1 Predicted number of events with 80 GeV $\leq m_J \leq$ 280 GeV according to this analysis, simulation from Ref. [1] and ATLAS simulation [9], as well as the resulting rescaling factors. 46

4.2 Expected mass windows in the different m_s distributions of the reconstructed large-radius jet mass. Mass windows are set to maximise the expected significance. 51

4.3 Predicted yield numbers for SM background and different signal samples with an integrated luminosity of 35.9 fb^{-1}. The signal samples are chosen as $g_x = 1$, $g_q = 0.25$ and $m_{\mathrm{DM}} = 100$ GeV at $m_s = 50$ GeV as in Ref. [1]. The SM background uncertainties are computed by taking the relative uncertainties from the ATLAS paper [9]. 52

4.4 Predicted yield numbers for SM background and different signal samples with an integrated luminosity of 35.9 fb^{-1}. The signal samples are chosen as $g_x = 1$, $g_q = 0.25$ and $m_{\mathrm{DM}} = 100$ GeV at $m_s = 70$ GeV as in Ref. [1]. The SM background uncertainties are computed by taking the relative uncertainties from the ATLAS paper [9]. 52

4.5 Predicted yield numbers for SM background and different signal samples with an integrated luminosity of 35.9 fb^{-1}. The signal samples are chosen as $g_x = 1$, $g_q = 0.25$ and $m_{\mathrm{DM}} = 100$ GeV at $m_s = 90$ GeV as in Ref. [1]. The SM background uncertainties are computed by taking the relative uncertainties from the ATLAS paper [9]. 52

5.1 The event selection requirements used in signal regions and control regions. Table taken from [12]. 62

5.2 Inclusive and exclusive signal efficiency comparison for T2bb(375,300) between CMS-SUS-15-005 α_T analysis (RA1) [11] and this search (Rivet). The CMS-SUS-15-005 analysed samples correspond to an integrated luminosity of 2.3 fb^{-1} at a centre-of-mass energy of 13 TeV. 65

5.3 Inclusive and exclusive signal efficiency comparison for T2bb(800,50) between CMS-SUS-15-005 α_T analysis (RA1) [11] and this search (Rivet). The CMS-SUS-15-005 analysed samples correspond to an integrated luminosity of 2.3 fb^{-1} at a centre-of-mass energy of 13 TeV. 65

5.4 Inclusive and exclusive signal efficiency comparison for T2bb(1000,100) between CMS-SUS-16-038 α_T analysis (RA1) [12] and this search (Rivet). The CMS-SUS-16-038 analysed samples correspond to an integrated luminosity of 35.9 fb^{-1} at a centre-of-mass energy of 13 TeV. 66

5.5 Inclusive and exclusive signal efficiency comparison for T2bb(550,450) between CMS-SUS-16-038 α_T analysis (RA1) [12] and this search (Rivet). The CMS-SUS-16-038 analysed samples correspond to an integrated luminosity of 35.9 fb^{-1} at a centre-of-mass energy of 13 TeV. 66

5.6 The CMS-SUS-16-038 α_T analysis (RA1) dataset [12] and 5 'Higgs Portal DM' model benchmarks' final yield numbers after all selections in 17 chosen most sensitive bins. The 5 benchmarks are shown as (m_s, $m_{Z'}$, m_{DM}). 70

1 Introduction

Our current knowledge of dark matter (DM) is very limited and comes from astrophysical and cosmological observations. Detecting and studying DM is very challenging, as it interacts very weakly with visible matter. Therefore, DM properties like its mass, coupling to visible matter, and structure are still unknown.

There are three DM discovery strategies: the first is by directly producing DM particles in particle colliders; the second is by directly searching for already-existing DM in the universe using low-background detectors; the final strategy is by looking for DM annihilation or decay products coming from the universe.

In this thesis we investigate direct DM production in particle colliders. To this purpose, the dark Higgs model [1] will be introduced. In this model a new mediator, the dark Higgs, provides a new DM annihilation channel, relaxing constraints from DM relic abundance in the universe [1]. Astrophysical searches for DM are evaded in this model, as DM annihilation rate is suppressed by the velocity of current DM from the universe [2,3]. We probe this model by producing a $Z^{'}$ that first radiates a dark Higgs and then decays into DM particles. The dark Higgs particle later decays into highly-boosted Standard Model (SM) particles [1]. In contrast to looking for DM produced back-to-back to initial-state radiation (ISR), DM recoils against the dark Higgs boson into a pair of boosted heavy quarks in this search. Strongest constraints to this model come from mono-Higgs searches at the LHC [4] [5–7]. However, these constraints are relaxed as the dark sector is highly decoupled from the SM in our model. Concluding, this model is extremely interesting as it cannot be excluded by the already-existing experimental constraints.

This thesis will focus on recasting and reinterpreting two existing DM searches at the LHC. A large-radius jet search from the ATLAS experiment [8] [9] and sub-jet kinematic variable search like α_T and $\Delta\phi^*_{min}$ from the CMS experiment [10] [11,12] will be respectively recast and reinterpreted in this thesis. Large missing transverse momentum (MET) will be required in both of these analyses to take DM production into account.

1.1 The evidence of dark matter

The concept of DM was first introduced by Fritz Zwicky [13]. In 1933, when calculating the mass of the Coma Cluster, Fritz Zwicky used the Virial Theorem to point

out the discrepancy between visible matter and total matter.

After the 1970s, DM had been accepted by the scientific community after detailed studies of galaxy rotation curves [14–17]. A rotation curve describes the dependence of the tangential velocity component (v_T) of gas or stars rotating around the galaxy to its distance (r) from the centre. As most of the luminous matter is located in the centre of the galaxy, a decrease of v_T as $1/\sqrt{r}$ would be expected if this was the only matter present. Figure 1.1 shows the observed rotation curve and the expected rotation curve from visible matter. As the tangential velocity increases at large radii, there must be other non-visible matter in the universe, which cannot produce electromagnetic radiation, but can contribute through gravitation. The huge discrepancy between the observed rotation curve and the expected rotation curve at large radii is a strong evidence for the existence of DM.

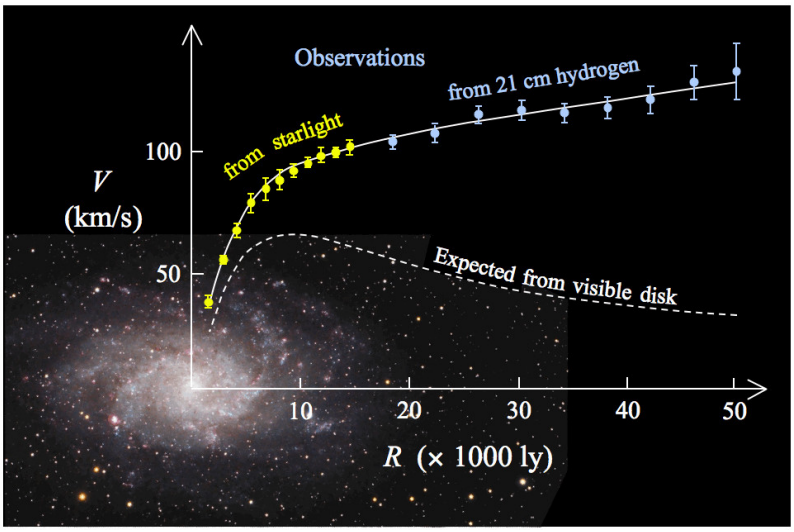

Figure 1.1: The rotation curve of galaxy M33. Figure taken from [19].

More recent proof of DM existence comes from the observation of the Bullet Cluster, two colliding galaxy clusters, in association with both X-ray and gravitational lensing measurements [18]. As shown in Fig. 1.2, the gravitational lensing map, which shows the total gravitational potential of the Bullet Cluster, does not follow the dominant baryonic mass component observed with X-ray data. From this discrepancy, one can conclude that the total matter distribution can not be explained by the baryonic component. This proves that another source of matter must be present in this system.

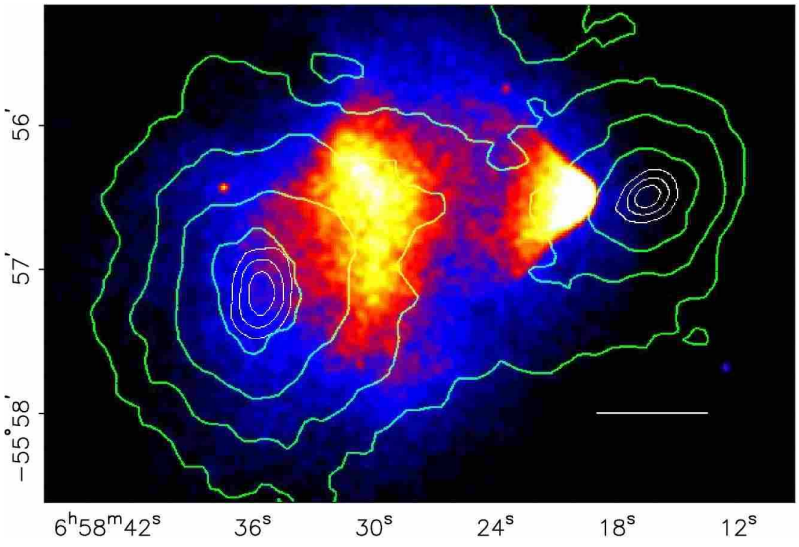

Figure 1.2: BulletCluster. The colour scale indicates the distribution of visible matter as observed with X-ray data and the green lines follow the distribution of all gravitating matter. Figure taken from [18].

1.2 Techniques of DM detection

There are three main methods of probing DM: production, direct and indirect detection.

Production In order to find out the properties of DM, experiments are trying to detect DM directly produced in high-energy collisions at particle colliders. Since DM candidates do not interact through electromagnetic and strong forces, detectors cannot directly measure DM candidates when they are produced in these kind of experiments. Therefore, the common signal in DM searches at colliders is missing transverse momentum (MET). We will discuss this method in more detail with 'mono-jet' and 'mono-V' methods in Section 1.3.

Direct detection In this method, detectors are employed to probe for already-existing dark matter through the measurement of interactions between DM and target nuclei. When a DM particle interacts with a nucleus, the recoil can ionise the matter in the detector, freeing electrons as an experimental signature. Because the probability of DM-nucleus scattering is quite small [20, 21], detectors are usually located in deep underground laboratories in order to reduce the large background. In 2008, DAMA (DArk MAtter) experiment observed an annual modulation signature, which might be caused by the relative speed of DM to the earth [20]. The annual modulation signature detected by DAMA experiment can be found in Fig. 1.3.

However, the DAMA signal is difficult to reconcile with constraints from other experiments. Therefore, an unambiguous test for DAMA is required. The SABRE experiment [21] is designed to achieve this with lower residual background than DAMA.

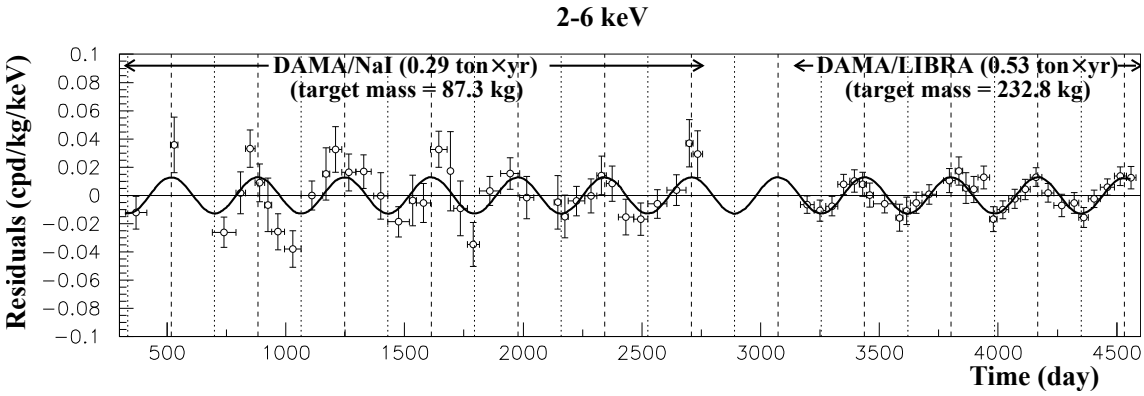

Figure 1.3: Annual modulation signature from DAMA, as shown in [20].

Indirect detection Indirect DM detections are based on DM annihilations and decays. The DM decay (annihilation) products can quickly decay and hadronize into stable SM states, which can leave clear signatures in the universe. This SM states can also leave secondary radiation by interacting with the environment, leaving additional traces of DM decay or annihilation. By looking at the energy spectrum of cosmic charged particles, photons, and neutrinos, theory-based measurements of DM properties can be performed [22]. In order to set stronger limits to DM properties, the most important part of this detection method is to find sensitive energy ranges where the background coming from ordinary astrophysics processes can be minimised. Table 1.1 taken from Ref. [23] shows a brief introduction to the recent, current and planned indirect DM experiments with the relative advantages and challenges.

1.3 Current collider dark matter production review: mono-jet and mono-V productions

As a dark Higgs model introduced in Ref. [1] will be exploited to search for DM at colliders in this thesis, a more detailed explanation of the current DM searches at colliders based on the work in Ref. [24] will be given here. Reference [24] focuses on DM particles in final state with an energetic jet (mono-jet) or a hadronically

Particles	Experiments	Advantages	Challenges
Gamma-ray, photons	Fermi LAT, MAGIC	point back to sources, spectral signatures	backgrounds
Neutrinos	IceCube, Super-Kamiokande	point back to sources, spectral signatures	backgrounds, low statistics
Cosmic rays	PAMELA, Fermi LAT	spectral signatures, low backgrounds for antimatter searches	diffusion, do not point back to sources

Table 1.1: Astroparticles for indirect dark matter searches, experiments, advantages, and challenges. Table taken from [23].

decaying W or Z vector boson (mono-V) at colliders.

1.3.1 mono-jet and mono-V productions

As DM particles cannot produce any observable signals in the detector, a mono-jet search can be performed by looking for jets radiated from the initial state that are recoiling against the produced dark matter. A typical signal in these searches is a single jet with a high transverse momentum (p_T) in association with large MET. In mono-V searches, typical final states are DM pairs in association with a weak vector boson. If the weak boson is at high p_T, its hadronic decay can be reconstructed as a large-radius jet due to the highly boosted decay products. Figure 1.4 and 1.5 show the main mono-jet and mono-V production mechanisms for spin-0 (scalar or pesudoscalar, S) and spin-1 (Z') mediators.

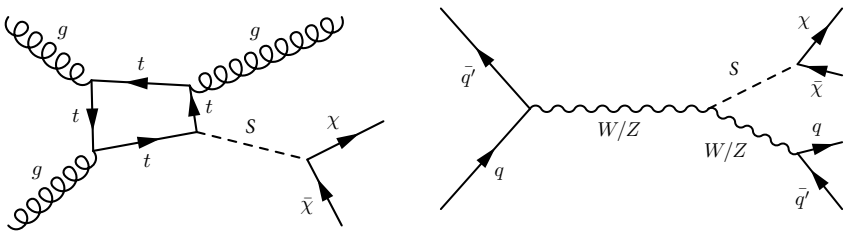

(a) Mono-jet (b) Mono-V

Figure 1.4: Mono-jet and mono-V production diagrams for a spin-0 mediator, as shown in [25].

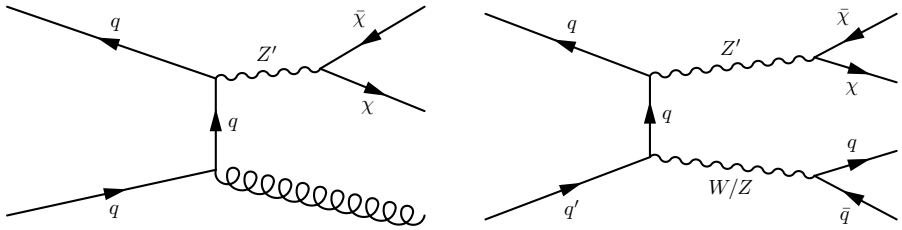

(a) Mono-jet (b) Mono-V

Figure 1.5: Mono-jet and mono-V production diagrams for a spin-1 mediator, as shown in [25].

1.3.2 Event selections and background estimation

Jets are reconstructed by the particle flow algorithm [26, 27] and anti-k_t algorithm [28]. The jet momentum is calibrated to account for pileup [29] and further corrected for resolution [30].

In mono-jet searches, jets are reconstructed using the anti-k_t algorithm with a radius of 0.4 (AK4 jets). The leading jet is required to have $p_T > 100$ GeV and $|\eta| < 2.5$ and events are required to have MET > 250 GeV. The QCD background is suppressed by setting the minimum azimuthal angle between missing transverse momentum $\vec{p}_T^{miss}$ and the first 4 leading jets with p_T >30 GeV greater than 0.5. The minimum azimuthal angle mentioned above will be referenced as $\Delta\phi(j_{1234}, \vec{p}_T^{miss})_{min}$. More details can be found in Ref. [24].

In mono-V searches, jets are reconstructed with a radius of 0.8 (AK8 jets) because reconstructing the W and Z boson decay as one AK8 jet is more efficient than by using two AK4 jets when the p_T of the weak bosons is high enough. In this analysis, W and Z bosons have $p_T > 250$ GeV, therefore the leading AK8 jet must have $p_T > 250$ GeV. Additionally, the leading jet is required to have $|\eta| < 2.4$. To be consistent with the masses of the gauge bosons, the leading jet invariant mass is required to be between 65 and 105 GeV. MET is required to be over 250 GeV and $\Delta\phi(j_{1234}, \vec{p}_T^{miss})_{min}$ is required to be greater than 0.5. In order to suppress boosted objects from the background of QCD jets with large invariant masses, the N-subjettiness variable τ_N [31] is introduced in this analysis. τ_N can probe the number of sub-jets within a jet. The lower τ_N is, the more likely a jet is to come from a N-prong decay. In this analysis, the ratio τ_2/τ_1 is an effective discriminating variable able to isolate 2-prong decays of W and Z bosons from the background of QCD jets with large invariant masses. In this analysis, the ratio of τ_2/τ_1 is required

to be less than 0.6.

In both mono-jet and mono-V searches, the most dominant background comes from Z boson invisible decay, $Z(\rightarrow \nu\nu)$ + jets, and W boson leptonic decay in which the lepton fails to be detected, $W(\rightarrow\ l\nu)$ + jets.

1.3.3 Results

Figure 1.6 shows the MET distributions in mono-jet and mono-V searches with an integrated luminosity of 35.9 fb^{-1}. The mediator-dependent exclusion region are drawn in Fig. 1.7 and Fig. 1.8 with an integrated luminosity of 35.9 fb^{-1}.

The upper limits at 95% confidence level (CL) [32,33] are calculated based on the ratio of the signal cross-section to the predicted cross-section, σ/σ_{th}. The asymptotic approximation [34] is also used in computing upper limits here. The limits are drawn in the $m_{med} - m_{DM}$ plane, where m_{med} stands for the mass of the mediator and m_{DM} is the DM mass. The region where the ratio σ/σ_{th} is less than one is excluded. And the region where the ratio σ/σ_{th} is over one is considered as a sensitive region for these analyses. Figure 1.7 shows the exclusion region for vector and axial-vector mediators at 95% CL and Fig. 1.8 shows the exclusion region for pseudoscalar mediators at 95% CL. The upper limits for scalar mediators at 95% CL are drawn through cross-section ratio σ/σ_{th} at $m_{DM} = 1$ GeV. Vector and axial-vector mediators with mass up to 1.8 TeV are excluded at 95% CL. And pseudoscalar mediators with mass up to 400 GeV are excluded at 95% CL. However, no significant exclusion region is expected in the scalar models at 95% CL. Cosmological constraints from the Planck satellite experiments [35] are also shown in Fig. 1.7 and Fig. 1.8. These limits have been found by computing the expected DM abundance for each model and comparing it to the satellite's measurement $\Omega_c h^2 = 0.12$ [36], where h is the Hubble constant and Ω_c is the DM relic abundance [24].

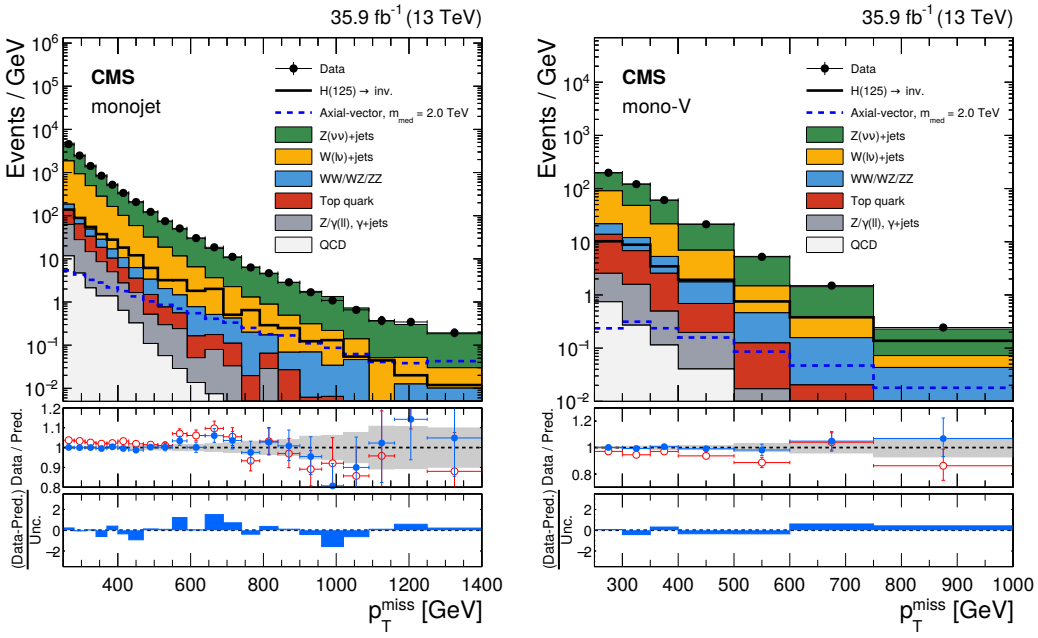

(a) Mono-jet (b) Mono-V

Figure 1.6: Observed MET distribution in mono-jet and mono-V signal regions with an integrated luminosity of 35.9 fb^{-1}. Left: the mono-jet search. Right: the mono-V search. MET $>$ 1250 (750) GeV for the mono-jet (mono-V) search has been applied for the last bin. Two signal events are drawn here: one from 125 GeV Higgs boson decaying to invisible particles and the other from 2 TeV axial-vector mediator decaying to 1 GeV dark matter particles. Ratios of data with pre-fit background distributions (red points) and postfit expected background distributions (blue points) are performed. The gray bands refer uncertainties. The difference between data and prediction over the sum of uncertainties is also shown at the bottom. Figure taken from [24].

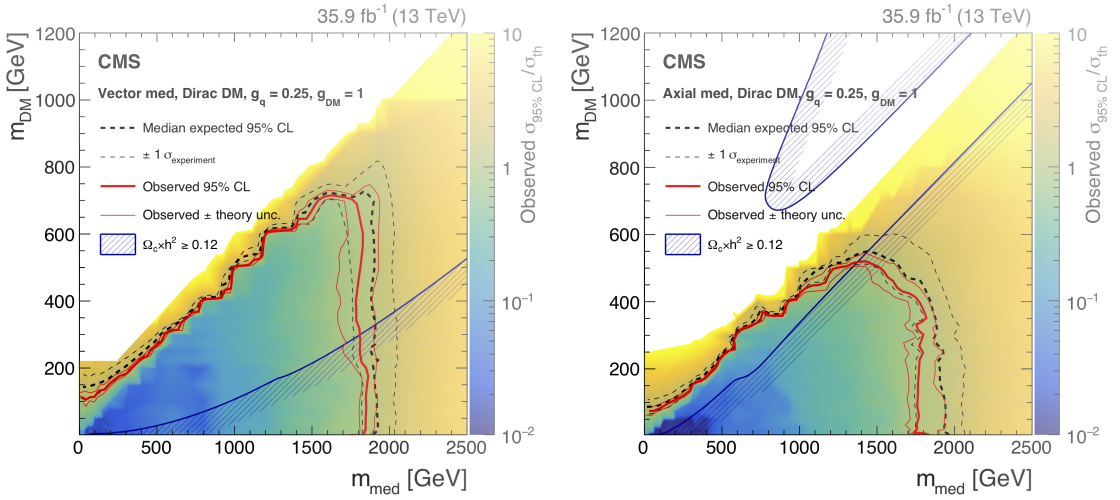

(a) Vector mediator (b) Axial-vector mediator

Figure 1.7: Exclusion limits at 95% CL with an integrated luminosity of 35.9 fb^{-1}. Left: the vector mediator. Right: the axial-vector mediator. The solid (dotted) red (blue) line refers the observed (expected) exclusion. One standard deviation has been drawn due to theoretical uncertainties from observed exclusion and statistical and systematic uncertainties from expected exclusion. The Planck satellite experiment constraints [35] are shown with dark blue lines. Figure taken from [24].

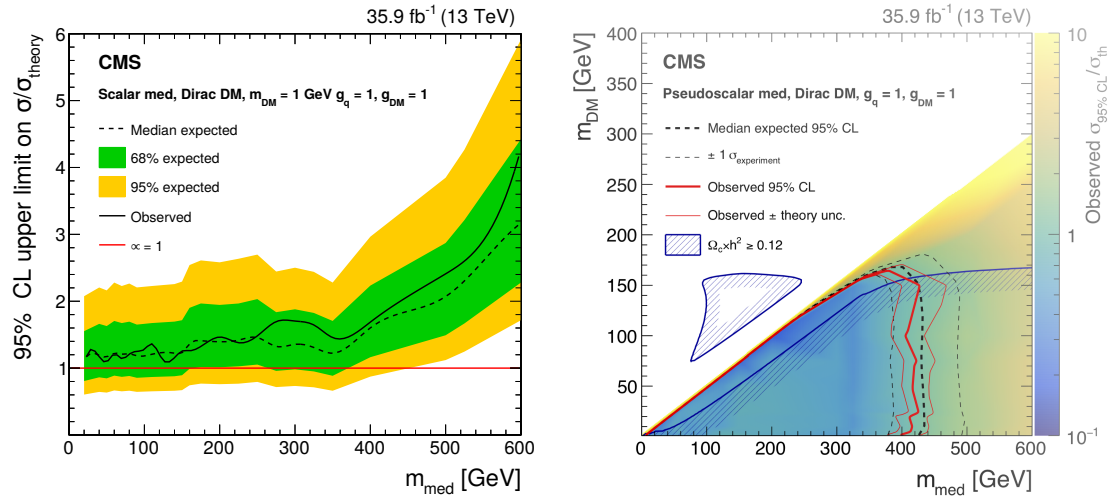

(a) Scalar mediator (b) Pseudoscalar mediator

Figure 1.8: The cross-section ratio plot at 95% CL is shown with an integrated luminosity of 35.9 fb^{-1}. Left: the scalar mediator. The benchmark for DM particle mass in this plot is 1 GeV. The dotted black line (solid balck line) refers to the expected (observed) upper limits on cross-section ratio. The red solid line refers to the cross-section from theoretical prediction is exactly the maximum cross-section which would be allowed at 95% CL. Exclusion limits at 95% CL with an integrated luminosity of 35.9 fb^{-1}. Right: the pseudoscalar mediator. The solid (dotted) red (blue) line refers the observed (expected) exclusion. One standard deviation has been drawn due to theoretical uncertainties from observed exclusion and statistical and systematic uncertainties from expected exclusion. The Planck satellite experiment constraints [35] are shown with dark blue lines. Figure taken from [24].

1.4 Thesis outline

This thesis aims to demonstrate that a search for the dark Higgs boson can be performed in the ongoing run at the Large Hadron Collider (LHC) and the dark Higgs can be in models of DM coupled to the spin-1 ($Z^{'}$) mediator. Until now, a review of the DM evidence, three DM measurement techniques, and current DM searches at colliders based on the work in Ref. [24] have been given. Some particle physics basic concepts and essential theories together with 'Higgs Portal Dark Matter' model will be introduced in Section 2. Section 3 will begin with a brief introduction to ATLAS and CMS, two general-purpose LHC detectors currently employed to search for new physics. Signal event generation will be also presented in Section 3. In this project, two different coupling sets will be used to generate signal events: one will apply the LHC recommendations [37], and the other will take the DM relic abundance constraint [2] into account. Based on Ref. [9] and Ref. [12], a large-radius mono-jet search from the ATLAS experiment and a more "generic" MET + jets search using α_T analysis from the CMS experiment will be respectively recast and reinterpreted in Section 4 and Section 5. Discussion and conclusion for these two searches will be given in Section 6 and Section 7.

2 Standard Model and 'Higgs Portal DM' model

2.1 Introduction to Standard Model

The Standard Model (SM) is a theoretical model describing three known fundamental forces out of four and classifying all known elementary particles. The SM can describe strong, weak, and electromagnetic interactions using a SU(3) × SU(2) × U(1) local gauge symmetry. Each type of interaction has at least one gauge boson as the interaction mediator. Z^0 and $W^{\pm}$ bosons are the mediators for weak interaction; out of these two bosons, only $W^{\pm}$ can mediate flavour-changing interactions. Photons (γ) mediate the electromagnetic interaction, and gluons (g) are the mediators of strong interaction. SM also encompasses three generations of elementary fermions, which are further divided into quarks and leptons. Both quarks and leptons can interact through the electromagnetic and weak force. Additionally, quarks can interact via strong force. Interaction strengths are described by constants. For the strong force, its value is around 1 ($\alpha_S \approx 1$); for the electromagnetic force is around 1/137 ($\alpha \simeq 1/137$); and for the weak force is around 10^{-6} ($\alpha_{W/Z} \approx 10^{-6}$). Finally, the Higgs boson is included in the SM in order to generate masses for particles through the spontaneous symmetry breaking mechanism, which will be explained in further details in Section 2.2.

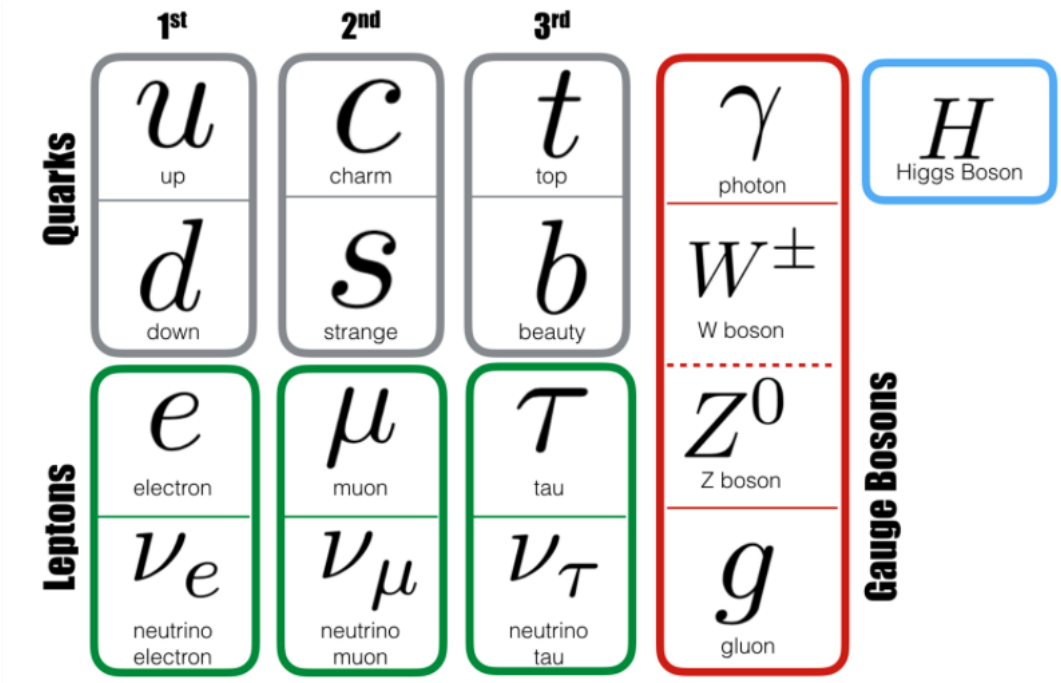

Figure 2.1: All the generations of elementary fermions and interaction mediators included in the Standard Model together with the Higgs boson. Figure taken from [38].

All the particle interactions can be described by Feynman diagrams. In these diagrams, the x-axis is interpreted as time and the y-axis as space. By reading from left to right, the evolution from the initial to the final state of a system can be read. Anti-particles are drawn in Feynman diagrams as particles moving backwards in time. Energy, momentum, angular momentum and charge are conserved in all interaction vertices in Feynman diagrams. Based on the Lorentz-invariant quantity carried by the mediator, defined in Eq. (2.1), Feynman diagrams can be categorised into s-, t- and u-channels. $\sqrt{s}$ is the total collision energy in the centre-of-mass frame.

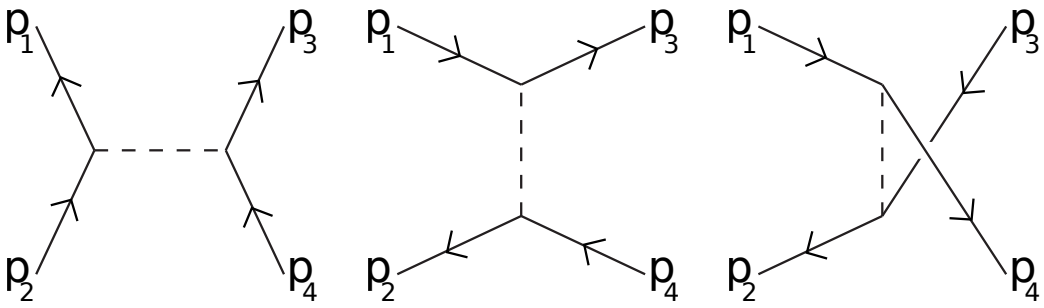

(a) s-channel (b) t-channel (c) u-channel

$$s = (p_1 + p_2)^2, t = (p_1 - p_3)^2, u = (p_1 - p_4)^2. \tag{2.1}$$

Figure 2.2: Three types of Feynman diagrams together with the respective Lorentz-invariant quantities.

2.1.1 Cross-section and decay rate

When measuring particle interactions and decays, cross-sections and decay rates are the main experimental observables. Cross-section is a parameter directly connected to the probability for a certain process to happen. It is defined as

$$\sigma = \frac{\text{Number of events per unit time per target}}{\text{Incident flux}}. \tag{2.2}$$

In particle accelerator physics, the incident flux is also called instantaneous luminosity ($\mathcal{L}_{inst}$), a parameter that can be directly computed starting from the properties of the particle beam. The cross-section for any two-body $\rightarrow$ two-body scattering interaction process in the centre-of-mass frame is given by

$$\sigma = \frac{1}{64\pi^2 s}\frac{p_f^*}{p_i^*}\int |M_{fi}|^2 d\Omega^*, \tag{2.3}$$

where p_i^* and p_f^* are respectively the momentum of the initial and final state. $d\Omega^*$ stands for the solid angle element computed in the centre-of-mass frame. Finally, $|M_{fi}|^2$ is the square of the interaction matrix element, which is Lorentz-invariant and can be computed from theory. The invariant differential cross section for any two-body scattering interactions can be written as

$$\frac{d\sigma}{dt} = \frac{1}{64\pi s|p_i^*|^2}|M_{fi}|^2. \tag{2.4}$$

Here, $|p_i^*|^2$ is a constant and it is calculated from energy and momentum conservation:

$$|p_i^*|^2 = \frac{1}{4s}[s - (m_1 + m_2)^2][s - (m_1 - m_2)^2]. \tag{2.5}$$

Eq. (2.4) applies to any rest frame because all quantities in the expression of $d\sigma/dt$ are Lorentz-invariant. Particle decay rate can be calculated from Fermi's Golden Rule,

$$\Gamma_{fi} = 2\pi|T_{fi}|^2\rho(E_f), \tag{2.6}$$

where Γ_{fi} is the number of transitions per unit time from initial state $|i\rangle$ to final state $\langle f|$, T_{fi} is transition matrix element and $\rho(E_f)$ is the density of final state. Γ_{fi} depends on the matrix element and the density of states. The former is computed from theory, the latter from kinematics. The two-body decay rate can be written in the rest frame ($E_i = m_i$) as

$$\Gamma_{fi} = \frac{|p^*|}{32\pi^2 m_i^2}\int |M_{fi}|^2 d\Omega, \tag{2.7}$$

where p^* is

$$p^* = \frac{1}{2m_i}\sqrt{[m_i^2 - (m_1 + m_2)^2][m_i^2 - (m_1 - m_2)^2]} \tag{2.8}$$

and m_1, m_2 stand for the masses of decay products from initial state $|i\rangle$.

2.1.2 Local gauge symmetry

The gauge bosons described in the SM are derived from the localisation of the SU(3) × SU(2) × U(1) gauge symmetry. To understand the importance of local gauge invariance in the SM, local U(1) gauge invariance will be considered as an example.

Under a U(1) local gauge transformation, the wave function $\psi(x)$ transforms as

$\psi(x) \rightarrow \psi^{'}(x) = e^{iq\chi(x)}\psi(x)$. To keep physics consistent, the Lagrangian must be invariant under this transformation. The Lagrangian of a free relativistic electron, $\mathcal{L}_0 = \overline{\psi}(i\gamma^\mu\partial_\mu - m_e)\psi$, is not invariant under a local U(1) transformation:

$$\mathcal{L}_0 \rightarrow \mathcal{L}_0 + \psi(x)\gamma^\mu\overline{\psi}\partial_\mu\chi e. \tag{2.9}$$

In order to obtain a gauge-invariant Lagrangian, the covariant derivative is introduced (here is $\partial_\mu \rightarrow D_\mu = \partial_\mu - ieA_\mu$). After applying the covariant derivative into $\mathcal{L}_0$, the final gauge-invariant Lagrangian of quantum electrodynamics (QED) is obtained:

$$\mathcal{L}_{QED} = \overline{\psi}(i\gamma^\mu\partial_\mu - m_e)\psi + e\overline{\psi}\gamma^\mu\psi A_\mu - \frac{1}{4}F_{\mu\nu}F^{\mu\nu}. \tag{2.10}$$

The term $e\overline{\psi}\gamma^\mu\psi A_\mu$ is directly obtained from the covariant derivative and stands for the interaction between the massless gauge boson (here is photon) and the electron. The term $1/4F_{\mu\nu}F^{\mu\nu}$ has been added in order to consider the energy of the photon's electromagnetic field. The photon field A_μ transforms as $A_\mu \rightarrow A_\mu^{'} = A_\mu - \partial_\mu\chi$ under a U(1) local gauge symmetry. By using a similar mechanism, gluon, $W^\pm$ and Z^0 gauge bosons can be respectively introduced into SM when SU(3) and SU(2) local gauge symmetries are applied.

2.2 The Higgs Mechanism

2.2.1 Motivation

Although the local gauge invariance works well in describing the interactions in the Standard Model, it can only work for massless particles. As an example, if the photon were massive in QED, an additional term, $\frac{1}{2}m_\gamma^2 A_\mu A^\mu$, should be added up in Eq. (2.10). This term transforms as

$$\frac{1}{2}m_\gamma^2 A_\mu A^\mu \rightarrow \frac{1}{2}m_\gamma^2(A_\mu - \partial_\mu\chi)(A^\mu - \partial^\mu\chi) \neq \frac{1}{2}m_\gamma^2 A_\mu A^\mu \tag{2.11}$$

under U(1) local gauge transformation, which breaks the U(1) local gauge symmetry. This happens not only in U(1) local gauge symmetry of QED, but also in SU(2) $\times$ U(1) and SU(3) local gauge symmetries of electroweak and quantum chromodynamics (QCD). This implies that it is impossible to introduce masses for $W^\pm$ and Z^0 bosons, which are observed to be massive. In order to generate particle

masses in SM, spontaneous symmetry breaking mechanism is necessary.

2.2.2 Spontaneous Symmetry Breaking

Spontaneous symmetry breaking (SSB) happens when a system falls from a symmetric state to a non-symmetric one in order to maintain the minimum energy level. To show how SSB can be used to introduce particle masses, the Lagrangian of a complex scalar field under the potential $V(\phi) = \mu^2(\phi^*\phi) + \lambda(\phi^*\phi)^2$ will be considered:

$$\mathcal{L} = \frac{1}{2}(\partial_\mu\phi_1)(\partial^\mu\phi_1) + \frac{1}{2}(\partial_\mu\phi_2)(\partial^\mu\phi_2) - \frac{1}{2}\mu^2(\phi_1^2 + \phi_2^2) - \frac{1}{4}\lambda(\phi_1^2 + \phi_2^2)^2. \tag{2.12}$$

ϕ_1 and ϕ_2 are the real and imaginary parts of the complex scalar field. If we only concentrate on the vacuum state, which is the lowest energy state with minimal potential energy, the λ corresponding to potential term in Equation (2.12) must be over zero in order to keep finite minimum for potential energy. If μ^2 is positive as well, the potential energy will have a minimum at $\phi_1 = \phi_2 = 0$ as shown in Fig. 2.3. However, if μ^2 is negative, the distribution of potential energy in ϕ_1 and ϕ_2 will look as in Fig. 2.3. In this case, the potential has infinite minima at

$$\phi_1^2 + \phi_2^2 = \frac{-\mu^2}{\lambda} = \nu^2, \tag{2.13}$$

where ν is called vacuum expectation value. By choosing the vacuum state, the global U(1) symmetry has been spontaneously broken. In SM, a new field called Higgs field and the corresponding scalar boson called Higgs boson (H) is introduced. Through the SSB mechanism, Higgs field assumes a non-zero vacuum expectation value, and by interacting with particles, it generates their masses. Interaction terms between Higgs and vector bosons are naturally introduced in the SM Lagrangian when SSB is implemented. These terms enable to relate the masses of the $W^\pm$ and Z^0 to one of the main parameters of the SM, the electroweak mixing angle, θ_W:

$$\frac{m_W}{m_Z} = cos\,\theta_W. \tag{2.14}$$

The SSB mechanism does not provide interaction terms which are able to provide masses to fermions. However, Yukawa couplings between the Higgs bosons and the fermions are manually introduced in the SM to this purpose, which was firstly

formalised in Ref. [40]. Yukawa couplings are the interaction strengths between fermions and Higgs bosons [40]. These couplings are related to the Higgs vacuum expectation value and the fermion masses through

$$m_f = \frac{\sqrt{2}}{2} g_f \nu. \tag{2.15}$$

where m_f is the fermion mass, g_f is the Yukawa coupling of this fermion and ν is the Higgs vacuum expectation value, which is ≈ 246 GeV. From Eq. (2.15), it can be concluded that the heavier a fermion is, the higher Yukawa coupling will be. Therefore, Higgs is more likely to interact with heavy particles and decay into them.

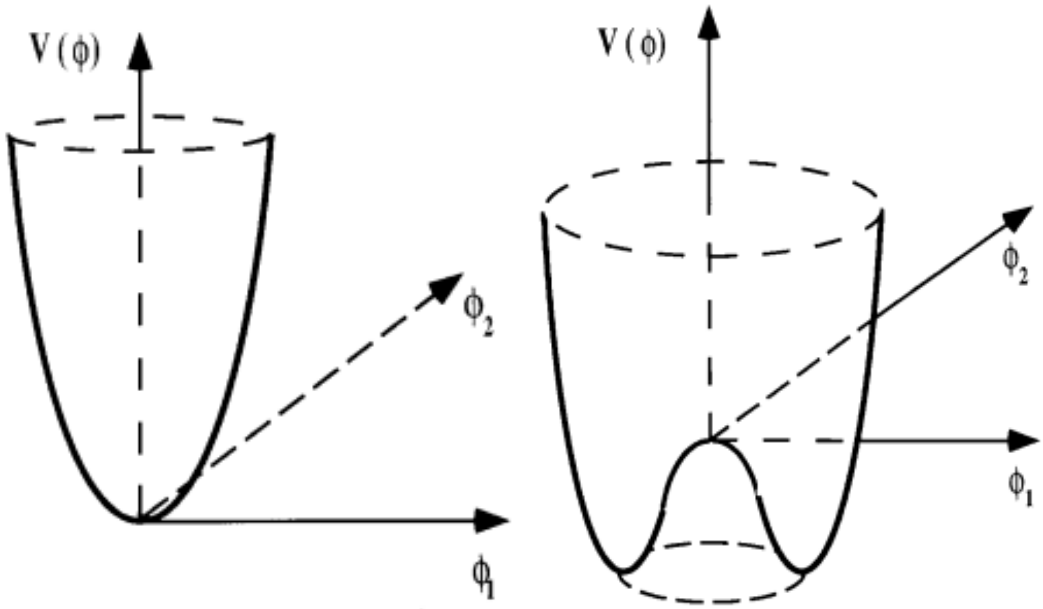

(a) the minimum potential energy at both fields = 0

(b) the minimum potential energy at $\phi_1^2 + \phi_2^2 = \nu^2$

Figure 2.3: The distribution of potential energy for a complex scalar field. ϕ_1 and ϕ_2 are the real and imaginary parts of the complex scalar field. Figure taken from [39].

2.3 Introduction to 'Higgs Portal DM' model

The 'Higgs Portal DM' model was firstly introduced in Ref. [1]. Three new types of particles are introduced in this model: Z', DM, and dark Higgs. Z' boson can couple to both SM quarks and DM. DM from this model is assumed to be the sole candidate for all the existing DM in the universe. In this thesis, the nature of this DM candidate will not be discussed. As the SM Higgs cannot generate mass for dark matter sectors in this model, the dark Higgs boson (s) has been introduced

to provide a mechanism to generate masses for the dark matter particles. This mechanism enables to relax constraints coming from the dark matter relic abundance by opening up a new annihilation channel. The dark matter relic abundance is defined as $\Omega_c h^2 = 0.12$ [36], where h is the Hubble constant and Ω_c is the DM relic abundance [24]. The two mediators introduced in the 'Higgs Portal DM' model, Z' and dark Higgs, open up a large number of DM annihilation channels such as $\chi\chi \to s \to q\bar{q}$, $\chi\chi \to Z' \to q\bar{q}$, $\chi\chi \to sZ' \to q\bar{q}$, and $\chi\chi \to s \to Z'Z'$ [2,41–43]. The main annihilation channels of this model will be discussed in Section 3.2.2.

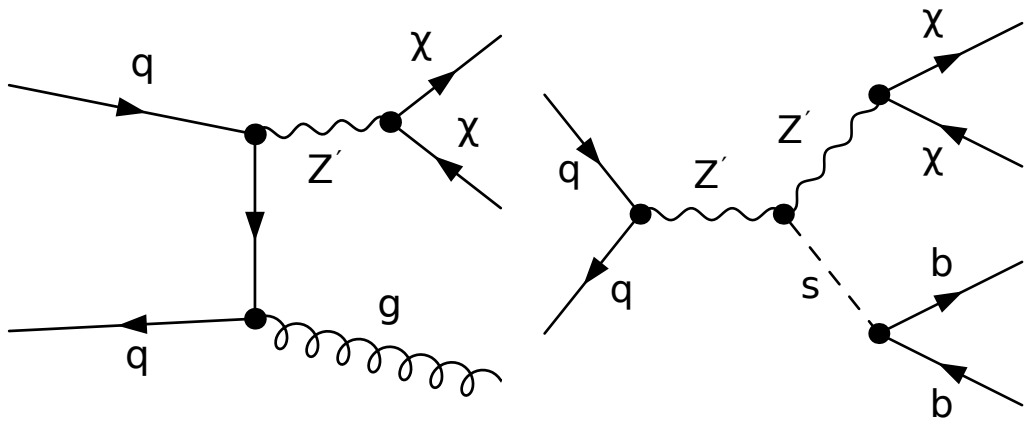

(a) Conventional mono-jet (b) Mono-dark-Higgs

Figure 2.4: Processes leading to missing energy signatures at the LHC. Left: a conventional mono-jet event. Right: a process leading to a mono-dark-Higgs signal. Figure taken from [1].

If the dark Higgs boson decays into SM particles via a small mixing with the SM Higgs boson, an experimental proof of the existence of such bosons can be found by looking for characteristic large-radius boosted jets in association with large missing transverse momentum (MET). In this project, we only look for the dark Higgs decaying to a pair of b-tagged jets. The expected experimental signatures are double b-tagged jets from the dark Higgs decay and large MET from escaping DM particles. As the double b-tagged jets from the dark Higgs decay can possibly merge into one large-radius jet if the dark Higgs is sufficiently boosted, this large-radius jet can be used to efficiently discriminate signal from background as jets coming from dark Higgs processes would look differently than the ones from conventional mono-jet events, as shown in Fig. 2.4. Figure 2.4 (a) shows the conventional mono-jet process and Figure 2.4 (b) shows the mono-dark-Higgs process. $q\bar{q} \to Z' \to q\bar{q}$ does not contaminate our signal as it does not produce large MET and a large-radius jet that are back to back with each other. In order to have a clear signature for our

signal process, the only requirement is the production of any dark sector state with sufficient large momentum.

There are five free parameters in 'Higgs Portal DM' model: the mass of DM candidate (m_{DM}), two mediators' masses, $Z^{'}$ ($m_{Z'}$) and the dark Higgs (m_s), the coupling between mediator $Z^{'}$ and quarks (g_q), and the coupling between dark sector and mediator $Z^{'}$ (g_x). In this parametrisation, the coupling of the dark Higgs is not a free parameter as it is completely defined by setting the above five parameters.

3 Dark Higgs searches at the LHC

3.1 Overview of ATLAS and CMS detectors

Because a large-radius mono-jet search from the ATLAS experiment [9] and a MET + jets search using α_T analysis from the CMS experiment [12] will be both reinterpreted in this project, a brief overview of ATLAS and CMS detectors is given here.

ATLAS [8] and CMS [10] are two general-purpose detectors currently employed to search for new physics. Although with different and complementary technologies, the two detectors are both formed by a set of concentric cylindrical layers which will be presented in the following paragraph from the innermost to the outermost one.

The innermost part of these two detectors holds the tracking system, whose purpose is to measure the momenta and charge of charged particles. This layer is followed by the electromagnetic calorimeter, which is used to measure the properties of electrons and photons. Together with the electromagnetic calorimeter, the hadron calorimeter measures both charged and neutral hadrons. Finally, the outermost layer holds the muon chambers, which are employed to detect muons.

The two detectors are enveloped in different magnetic fields, that bend the tracks of charged particles and enable the measurement of their momentum and charge using the tracking system. In ATLAS, one solenoid and three toroid magnets are employed to generate the field, while one massive solenoid magnet is used in CMS.

A smearing based on the ATLAS and CMS detector resolutions has been applied to specific jet kinematic variables in both analyses. The ATLAS detector jet reconstruction performance at $\sqrt{s} = 13$ TeV is approximated in the large-radius mono-jet recast by taking the ATLAS off-line jet mass resolution [44], b-tagging performance [9], and MET resolution [45] into account. The CMS detector b-tagging performance [12] at $\sqrt{s} = 13$ TeV is simulated in a similar manner in the MET + jets search using the α_T analysis.

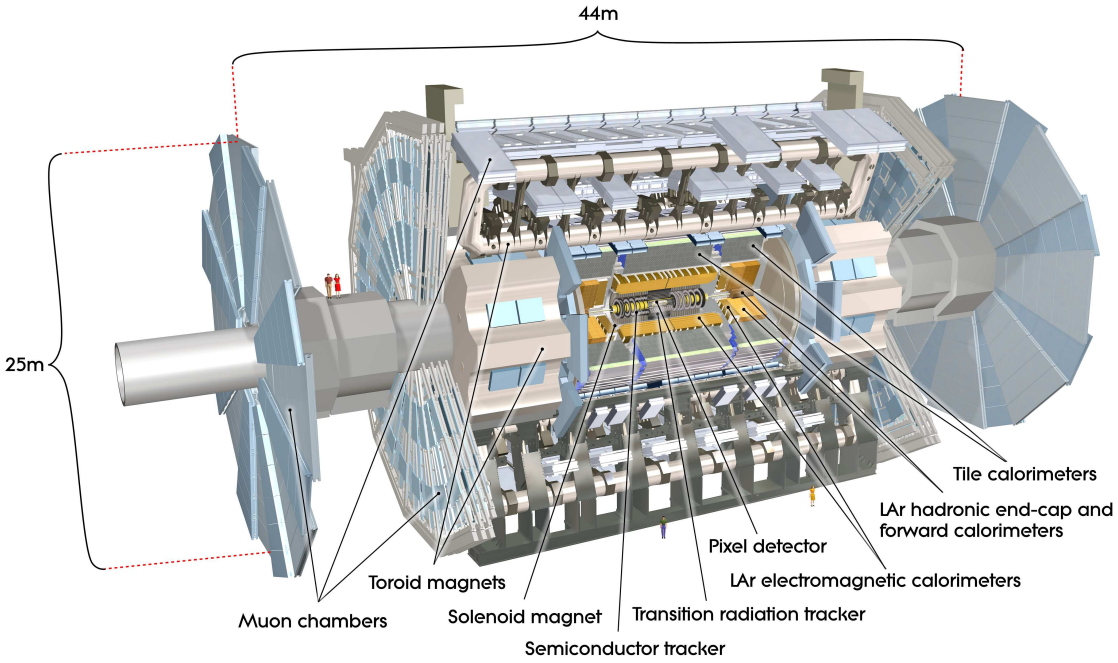

Figure 3.1: Schematic view of the ATLAS detector as shown in [8].

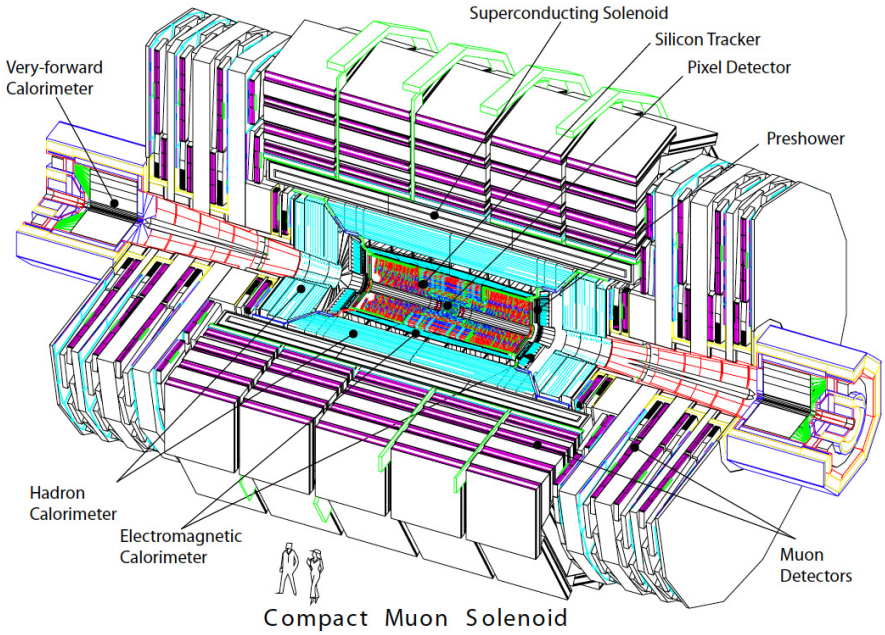

Figure 3.2: Schematic view of the CMS detector as shown in [10].

3.2 Signal generation

In this project, two different methods have been used to define the five free parameters of the 'Higgs Portal DM' model as introduced in Section 2.3. One is to consider couplings as recommended by LHC where g_x, the coupling strength between Z' and the DM candidate, is set to 1 and g_q, the coupling strength between Z' and quarks, is set to 0.25 [37]. The other is to define couplings based on the DM relic abundance constraint from the universe and by assuming possible DM annihilation channels [2]. In both scenarios we assume the Z' decay width to be 10 GeV. Parameter ranges considered in this project are shown in Table 3.1.

Coupling set	LHC	Astrophysics
g_x	1	$< (4\pi)^{1/2}$
g_q	0.25	0.25
m_s [GeV]	50, 70, 90	50, 70, 90
$m_{Z'}$ range [GeV]	(200, 3000)	(500, 4000)
m_{DM} range [GeV]	(100, 500)	(100, 800)

Table 3.1: The parameter ranges considered in this project with two coupling scenarios. In this table, LHC refers to the coupling scenario consistent with the LHC recommendation and Astrophysics refers to the coupling scenario considering the DM relic abundance constraint from the universe.

We use the same code to present both types of coupling scenario as described in Ref. [1]: both types of coupling scenario are generated through **micrOMEGAs v4.2.5** [46]. All signal events are generated by **MadGraph5_aMC@NLO v2.3.3** [47]. **Pythia 8** [48] and **Rivet v2.5.2** [49] are used for showering and event selection.

3.2.1 Coupling scenario in consistence with LHC collaborations

LHC working groups recommends considering $g_x = 1$ and $g_q = 0.25$ for both vector and pseudovector mediators [37]. In vector models, the ratio of width/mass for the mediator has to be $\ll 1$ due to perturbativity constraints. In order for the width of the mediator to be smaller than its mass, g_q is set below unity so that the Narrow Width Approximation can be applicable [50]. As Z' is a spin-1 mediator, signal events have been generated using $g_x = 1$ and $g_q = 0.25$ in this project. This coupling scenario has been widely used in current DM searches at colliders like Ref. [9], Ref. [24] and Ref. [51].

3.2.2 Coupling scenario considering the DM relic abundance constraint from the universe

Based on the mediators involved in the 'Higgs Portal DM' model and the astrophysical constraint of DM relic abundance from the universe, there are two characteristic DM annihilation channels in this model [1, 2]. The first annihilation channel can produce $Z^{'}$ through DM particles annihilating and $Z^{'}$ can then decay to SM particles. This process can be described as $\chi\chi \to Z' \to q\bar{q}$. The second annihilation channel can produce the dark Higgs s through DM particles annihilating and the dark Higgs s can then decay into SM particles. This process can be described as $\chi\chi \to s \to q\bar{q}$. Each annihilation channel is related to one coupling parameter [1,2]. In the annihilation involving the dark Higgs, DM Yukawa coupling y_x should be considered and for the annihilation channel mediated by the $Z^{'}$ boson, coupling g_x should be considered [1,2]. In 'Higgs Portal DM' model, there is a specific relation between these two parameters

$$g_x = \frac{m_{Z'}}{m_{\mathrm{DM}}} \frac{y_x}{2\sqrt{2}}, \tag{3.1}$$

as the dark Higgs generates both the DM mass and the $Z^{'}$ mass [1]. Figure 3.3 taken from Ref. [1] shows the two parameters' distributions in a $m_{Z'} - m_{\mathrm{DM}}$ plane with fixed m_s and g_q numbers.

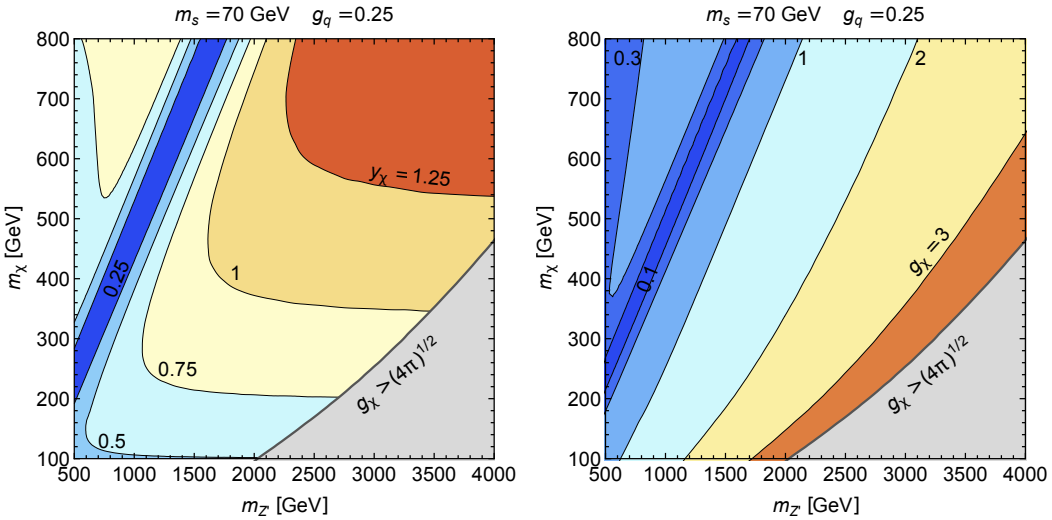

(a) y_x distribution (b) g_x distribution

Figure 3.3: y_x and g_x distributions under relic abundance for $m_s = 70$ GeV and $g_q = 0.25$. $g_x > 4\pi^{1/2}$ is the limitation of this process as g_x should remain perturbative. m_χ is the same as m_{DM}. Figure taken from [1].

It can be concluded from Fig. 3.3 that $\chi\chi \to s \to$SM is the dominant DM annihilation channel when $m_{Z'} \gg m_{\mathrm{DM}}$ as y_x tend to become a small constant while g_x is quite large for $m_{Z'} \gg m_{\mathrm{DM}}$. It also can be observed from Fig. 3.3 that for $m_{\mathrm{DM}} \approx m_{Z'/2}$, $\chi\chi \to Z' \to q\bar{q}$ is the leading DM annihilation channel with a sufficient small g_x to provide relic abundance. $\chi\chi \to sZ' \to q\bar{q}$, $\chi\chi \to s \to Z'Z'$ and other types of annihilation channels [2, 41–43] are not discussed in this analysis as they are less important in the considered regime where m_{DM} is not greater than $m_{Z'}$.

As can be seen from Fig. 3.3, in order to fulfil the relic density constraint, g_x needs to vary strongly as a function of $m_{Z'}$ and m_{DM}. In particular, the region of parameter space cannot be studied where $g_x > 4\pi^{1/2}$ for large $m_{Z'}$ because the theory becomes non-perturbative in this region.

3.2.3 Signal events with coupling scenario considering the DM relic abundance constraint from the universe

Since we use the same tools as in Ref. [1] to compute the coupling scenario from the DM relic abundance constraint, for consistency we can compare the g_x distribution used in our analysis with the one in Ref. [1]. As shown in Section 3.2.2, Figure 3.3 taken from Ref. [1] displays the g_x distribution under the constraint from the DM relic abundance for $m_s = 70$ GeV and $g_q = 0.25$. Figure 3.4 shows our g_x distribution under the DM relic abundance constraint for $m_s = 70$ GeV and $g_q = 0.25$.

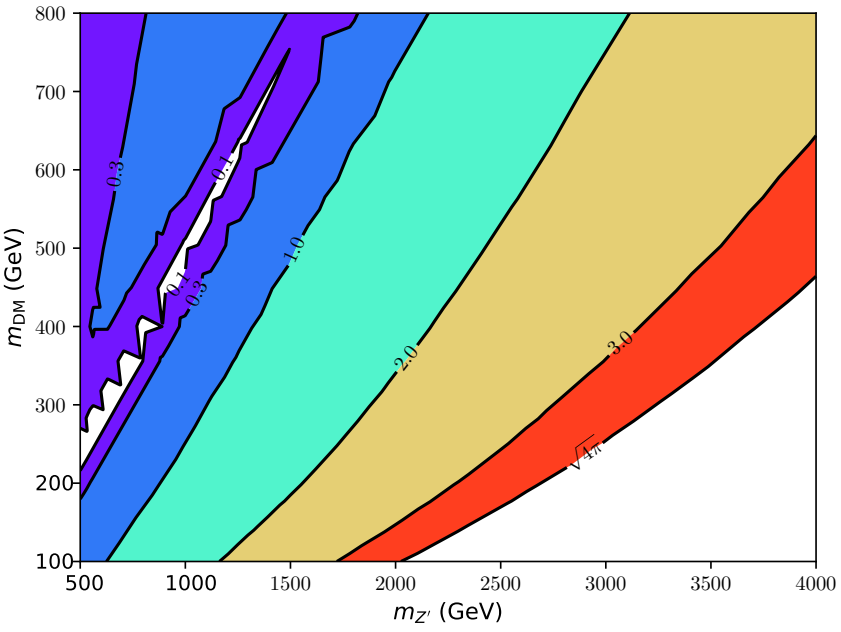

Figure 3.4: g_x distribution under DM relic abundance for $m_s = 70$ GeV and $g_q = 0.25$.

By comparing Fig. 3.3 and 3.4, it can be concluded that the couplings used in our signal generation are consistent with the one used in Ref. [1] and the tool can be reliably used to generate signal events under the DM relic abundance constraint.

4 Dark Higgs search with large-radius jets

In this chapter a recast of the large-radius mono-jet search from the ATLAS experiment [9] will be performed. All signal and the dominant background events are generated by **MadGraph5_aMC@NLO v2.3.3** [47]. Signal events are generated in the two coupling scenarios presented in Section 3.2 for the dark Higgs mass m_s ranging from 50 GeV to 90 GeV. **Pythia 8** [48] and **Rivet v2.5.2** [49] are used for showering and event selection. The dominant background uncertainties are computed by taking relative uncertainties from the published ATLAS paper [9]. Finally, **HiggsCombineTool** [52] from **CMSSW_8_1_0** [53] is applied to calculate the expected exclusion upper limits at 95% confidence level (CL) [32,33]. The upper limits are calculated based on the excluded ratio of the signal cross-section to the predicted cross-section, σ/σ_{th}, with an integrated luminosity of 35.9 fb^{-1}.

In this chapter, the dominant background samples and event selection requirements for the large-radius mono-jet search are discussed in Section 4.1. Validation between our analysis and the published ATLAS analysis is examined in Section 4.2 and our results for the recast of this search are presented in Section 4.3.

4.1 Interpretation of large-radius jets analysis

The large-radius mono-jet analysis from the ATLAS experiment searches for large missing transverse momentum (MET) from DM production together with a SM Higgs decaying to $b\bar{b}$ [9]. Here, we reinterpret this analysis into our 'Higgs Portal DM' model. The expected signal signatures are double b-tagged large-radius jets from the high p_T dark Higgs decay and large MET from DM particles. Therefore, the main SM backgrounds to this search are: processes ending up with double b-tagged large-radius jets; processes ending up with large-radius jets containing both b-quark jets and c-quark jets, where c-quark jets can be misidentified as b-quark jets. In both cases, large-radius jets must be produced in association with large MET.

4.1.1 Expected main backgrounds

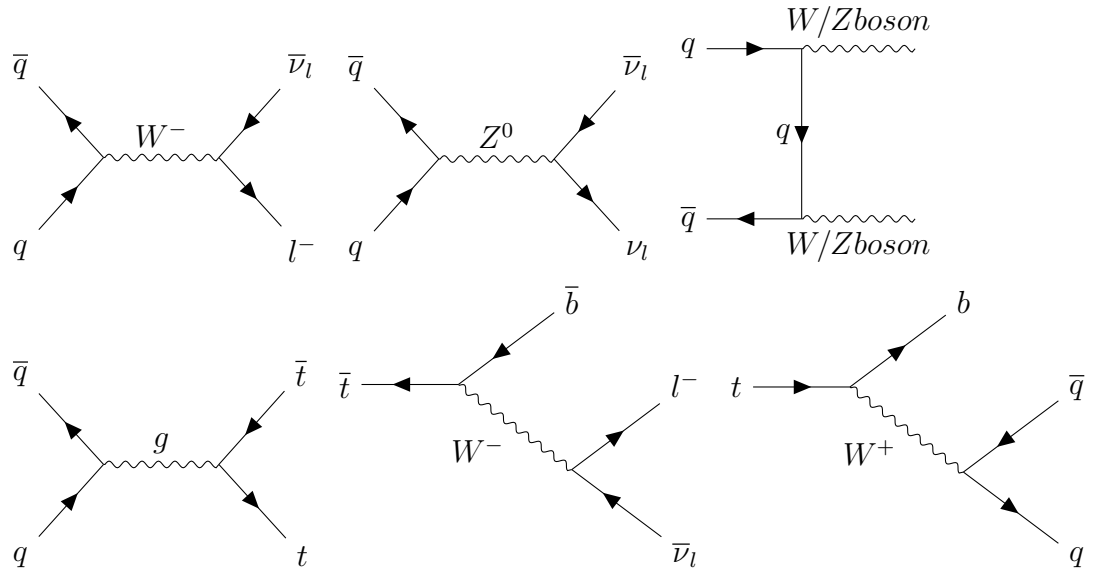

Figure 4.1: Feynman diagrams for most relevant Standard Model backgrounds. Top: W, Z and diboson events leading to MET. Bottom: $t\bar{t}$ background resulting from semi-leptonic decays of top pair production.

Figure 4.1 shows the dominant background samples for our dark Higgs search with large-radius jets.

***Z* + *bb̄*:** One Z boson decay can contaminate our signal if the Z boson decays into a neutrino-antineutrino pair ($\nu\overline{\nu}$) together with a $b\bar{b}$ pair from gluon splitting. This process can be described as $pp \to Z(\to \nu\overline{\nu})\ b\bar{b}$.

***W* + *bb̄*:** One W boson decay can contaminate our signal if the W boson decays leptonically and the charged lepton from the W decay is not identified. $b\bar{b}$ pair can come from gluon splitting. This process can be described as $pp \to W(\to l\nu)\ b\bar{b}$.

***tt̄*:** $t\bar{t}$ can contaminate the signal through semi-leptonic decays. If a t-quark decays semi-leptonically, a large amount of MET can be measured when the charged lepton is not identified. If the other t-quark decays hadronically into a c-quark and a b-quark, double b-tagged large-radius jets can originate when this t-quark's p_T is large enough and the c-quark is mistagged as a b-quark. In the circumstance that the remaining t-quark hadronic decay does not produce a misidentified b-tagged signal, another b-tagged signal can be imitated by gluon splitting or misidentified light-flavour jets.

Diboson: Z boson pair-decays can contaminate our signal if one Z boson decays into a neutrino-antineutrino pair ($\nu\overline{\nu}$) and the other Z boson decays into a $b\bar{b}$ pair. This process can be described as $pp \to Z(\to \nu\overline{\nu})\ Z(\to b\bar{b})$. WZ pair-decays can also contribute when W boson decays leptonically and the charged lepton from W decay is not reconstructed, and Z boson decays into a $b\bar{b}$ pair. We describe this process as $pp \to W(\to l\nu)\ Z(\to b\bar{b})$. In addition, WW pair-decays can also contaminate the signal if one W boson decays leptonically and the charged lepton from its decay is not identified, and a c-quark from another W boson decay is misidentified as a b-quark. Another b-quark can be produced from gluon splitting.

We use the same background samples mentioned in Ref. [1]. Background samples have been generated using **MadGraph5_aMC@NLO v2.3.3** [47]. **Pythia 8** [48] is applied to background samples for showering. Finally, we run the same **Rivet v2.5.2** [49] analysis to both background samples and signals.

4.1.2 Event selection

The event reconstruction and selection are set up in the **Rivet v2.5.2** analysis following Ref. [9].

Event reconstruction: Large-radius jets are built using the anti-k_t algorithm [28] implementation in **FastJet v3.2.0** [54] with radius R = 1.0 [9]. All the final state particles except leptons are used in this large-radius jet reconstruction process. Large-radius jets are required to have both $p_T > 250$ GeV and pseudo-rapidity $|\eta| < 2.0$ to keep consistent with Ref. [9]. Sub-jets are implemented in this analysis with the purpose of identifying fat-jet flavour. Sub-jets are built using the anti-k_t algorithm implementation in **FastJet v3.2.0** with radius R = 0.2 as recommended by Ref. [9]. Sub-jets are required to have $p_T > 10$ GeV as well as $|\eta| < 2.5$ [9]. Sub-jets can only contribute to a large-radius jet if Δ R (sub-jet, fat-jet) < 1.1. We use the same b-tagging technique, the 'ghost-association' technique, as described in Ref. [55]. The ghost-association technique is used to match sub-jets to large-radius jets. A large-radius jet is double b-tagged only if two sub-jets inside the large-radius jet are b-tagged. In order to remove the soft part of the large-radius jet, we use the same trimming procedure described in Ref. [56]: sub-jets have been formed inside the large-radius jet with a radius of 0.2 by the k_t algorithm and discarded if they

carry less than 5% of the total large-radius jet energy. We use the same muon correction as described in Ref. [1] to find muons coming from b-quark decays: muons are counted as a constituent of the large-radius jet if the distance between the $b-$tagged sub-jets which has been geographically matched to a large-radius jet, and the closest muon is less than 0.2, ΔR (b-tagged sub-jet, closest muon) < 0.2.

In this **Rivet v2.5.2** analysis, contributions from pile-up are not considered. A smearing has been applied to specific jet kinematic variables in order to take account for the ATLAS detector jet reconstruction performance. The ATLAS detector at $\sqrt{s} = 13$ TeV response is approximated by taking the ATLAS off-line jet mass resolution [44], b-tagging performance [9], and MET resolution [45] into account. We use the same mass resolution procedure mentioned in Ref. [44]: the large-radius jet is smeared with a 10% mass resolution. Also, we use the same b-tagging efficiency as the ATLAS experiment [9]: an average efficiency of 70% is used in identifying track jets containing b-hadrons with probabilities of 18% for c-quark jets misidentification and 0.6% for light-flavoured jets misidentification. Finally, we use the same MET resolution as described in Ref. [45]: MET resolution follows $k\sqrt{\sum E_T}$, where the parameter k is around 0.5 GeV$^{1/2}$.

In order to suppress background samples and maximise the expected signal over background ratio (SG/BG), the event selection is applied as follows.

Event selection: In order to avoid low MET events, MET > 500 GeV is applied in this **Rivet v2.5.2** analysis. In **Rivet v2.5.2**, the negative sum of all visible object momentum is calculated as MET. In this large MET scenario, the dark Higgs decay products can merge into a large-radius jet and boost against the large MET resulting from DM production. In order to keep our analysis consistent with 'Higgs Portal DM' model predictions and avoid pile-up or initial state radiation smearing, we require the number of large radius jets to be one. In our analysis, we also reject isolated leptons only allowing leptons that originate from the large-radius jet. This rejects background events in which leptons are produced in pile-up interactions or SM gauge boson decays. As the dark Higgs decay products are merged at high energies, we expect the reconstructed large-radius jet mass to be equivalent to the mass of the dark Higgs. Therefore, mass windows in the reconstructed large-radius jet mass distribution can be used in order to improve our SG/BG ratio. Signals

with different m_s can have different mass windows, which will be further discussed in Section 4.3.2.

4.2 Validation

In order to validate our **Rivet v2.5.2** analysis results, we compare them with the published ATLAS paper [9] and Ref. [1] as follows.

4.2.1 Comparison with ATLAS analysis

Since the ATLAS analysis [9] uses the same types of SM background as ours in the large-radius jet search with large MET, we apply our **Rivet v2.5.2** analysis to our SM background samples and compare our predicted number of events with ATLAS results. The event selection requirements are the same between our and ATLAS analyses. In Ref. [9], SM background distributions are presented over the mass window 80 GeV $< M_J <$ 280 GeV. Therefore, we simply apply the same mass window into our **Rivet v2.5.2** analysis. Table 4.1 shows the predicted number of events in our analysis and the ATLAS simulation [9].

3.2 fb^{-1}	$t\bar{t}$	$W + b\bar{b}$	$Z + b\bar{b}$	Diboson
ATLAS prediction from [9]	4.83±0.88	2.48±0.71	3.80±0.44	1.20±0.12
Prediction from [1]	2.83±0.12	1.16±0.06	2.42±0.07	0.56±0.02
Rescaling factors from [1]	1.7±0.3	2.1±0.6	1.6±0.2	2.1±0.2
Prediction from this analysis	3.00	1.32	2.34	0.98
Rescaling factors from this analysis	1.61	1.88	1.62	1.22

Table 4.1: Predicted number of events with 80 GeV $\leq m_J \leq$ 280 GeV according to this analysis, simulation from Ref. [1] and ATLAS simulation [9], as well as the resulting rescaling factors.

We present our results with an integrated luminosity of 3.2 fb^{-1} to be able to compare with both ATLAS [9] and Ref. [1] results. It can be concluded from Table 4.1 that our prediction is generally smaller than the ATLAS simulation by a factor of 1.2 to 1.9 among all the types of SM background. This discrepancy may result from the detector reconstruction in our **Rivet v2.5.2** analysis. There is no dedicated detector reconstruction applied in this analysis and we only use mass resolution for the large-radius jet, MET resolution and b-tagging efficiency as the detector response. However, a full simulation has been applied in Ref. [9] to all the types of SM background. To obtain consistent background numbers, we scale our results to the ATLAS background yields with the help of rescaling factors.

4.2.2 Comparison with DESY analysis

We observe a similar discrepancy between our simulation and the ATLAS analysis [9] as reported in the DESY analysis [1]. This DESY analysis [1] focused on recasting the large-radius jet search from Ref. [9] using a fast simulation method. From Table 4.1, it can been concluded that our scaling factors are within the DESY rescaling factor uncertainties except diboson samples, in which we predict a number closer to ATLAS simulation than the DESY prediction. Figure 4.2 shows the SM background in the distribution of the reconstructed large-radius jet. The SM background samples are drawn after applying rescaling factors with an integrated luminosity of 3.2 fb^{-1}. Figure 4.2 agrees with SM background in the reconstructed large-radius jet mass distributions from Ref. [1].

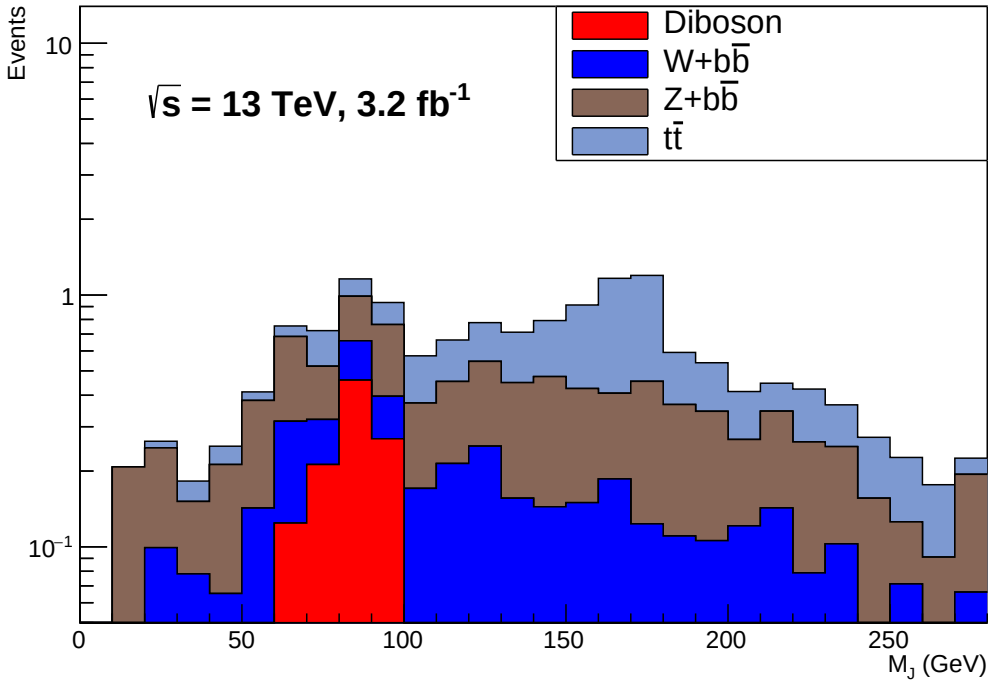

Figure 4.2: SM background under the reconstructed large-radius jet mass distributions with an integrated luminosity of 3.2 fb^{-1}. All event selection requirements except sensitive mass windows have applied to generate this plot. The reconstructed large-radius jet mass is shown up to 280 GeV to give an overall SM background distribution.

By comparing our simulation results with ATLAS simulation results and DESY simulation results, we can conclude that our **Rivet v2.5.2** analysis is valid.

4.3 Results

This section will cover the results of our recast of the large-radius mono-jet search from the ATLAS experiment [9]. We scale our simulated samples to an integrated luminosity of 35.9 fb^{-1}, the same amount recorded by the ATLAS and CMS experiments in the 2016 data taking period, as mentioned in Section 4.3.1. As mentioned in Section 4.1.2, different m_s signals have different sensitive mass windows in the distribution of the reconstructed large-radius jet mass. We will use our generated signal events with m_s = 50, 70, and 90 GeV to optimise for different dark Higgs mass windows. In Section 4.3.2, we will present the large-radius jet mass window for each m_s signal taken into consideration in this study. The expected signal and background yield numbers will be shown in Section 4.3.3. Finally, Section 4.3.4 will present the exclusion limits we generated for both LHC [37] and relic density [2] coupling scenarios with different m_s.

In order to be consistent with Ref. [1] and Ref. [9], signal samples with coupling scenarios same as the LHC preference [37] will be presented from Section 4.3.2 to Section 4.3.3.

4.3.1 Scaling to 35.9 fb^{-1}

Figure 4.3 shows the SM background distribution after applying rescaling factors with an integrated luminosity of 35.9fb^{-1}. The reconstructed large-radius jet mass range shown in Fig. 4.3 covers our sensitive region for the dark Higgs search. The sensitive region for the dark Higgs search will be discussed in Section 4.3.2.

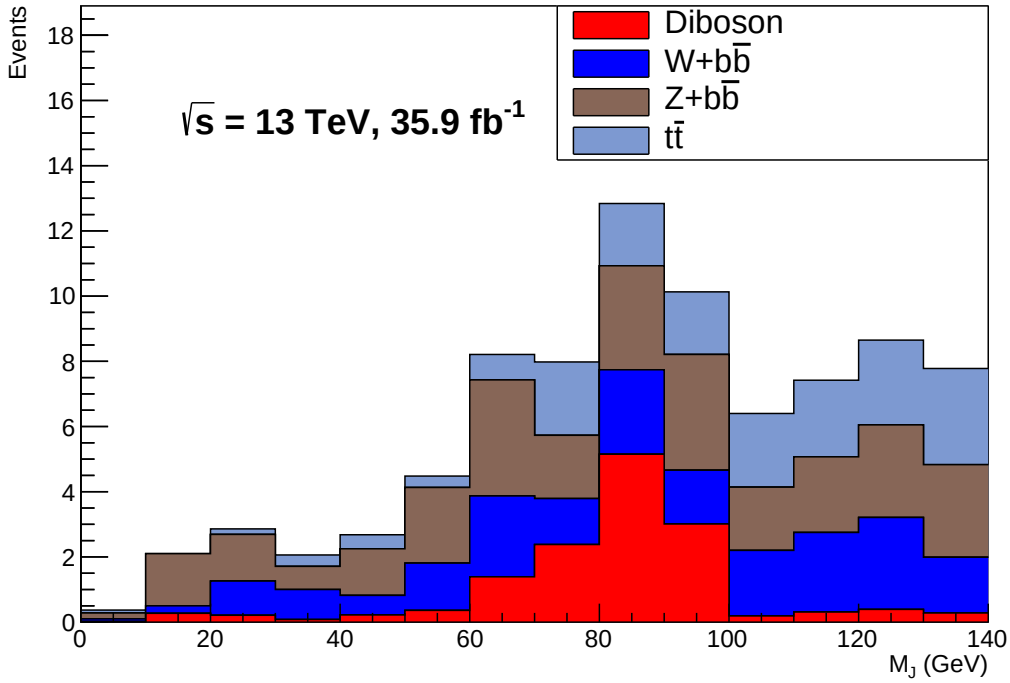

Figure 4.3: SM background in the reconstructed large-radius jet mass distribution with an integrated luminosity of 35.9 fb^{-1}. All event selection requirements except sensitive mass windows have been applied to generate this plot. The reconstructed large-radius jet mass is shown up to 140 GeV as our signal sensitive region for the dark Higgs search are within this area.

4.3.2 Higgs mass window optimisations

Different m_s signals have different sensitive mass windows in the distribution of the reconstructed large-radius jet mass. In order to optimise the dark Higgs mass windows for different m_s signals, we choose the same signal samples as Ref. [1]. The dark Higgs mass windows are set to maximise the expected significance. Figure 4.4 shows the reconstructed large-radius mass distribution for signal processes with different m_s and different $m_{Z'}$ with an integrated luminosity of 35.9 fb^{-1}. The signal processes are chosen according to the Ref. [1], using the coupling scenario suggested by the LHC working group [37]. Figure 4.4 shows that signal events always peak around the dark Higgs masses. Table 4.2 displays the mass windows chosen for different m_s signals.

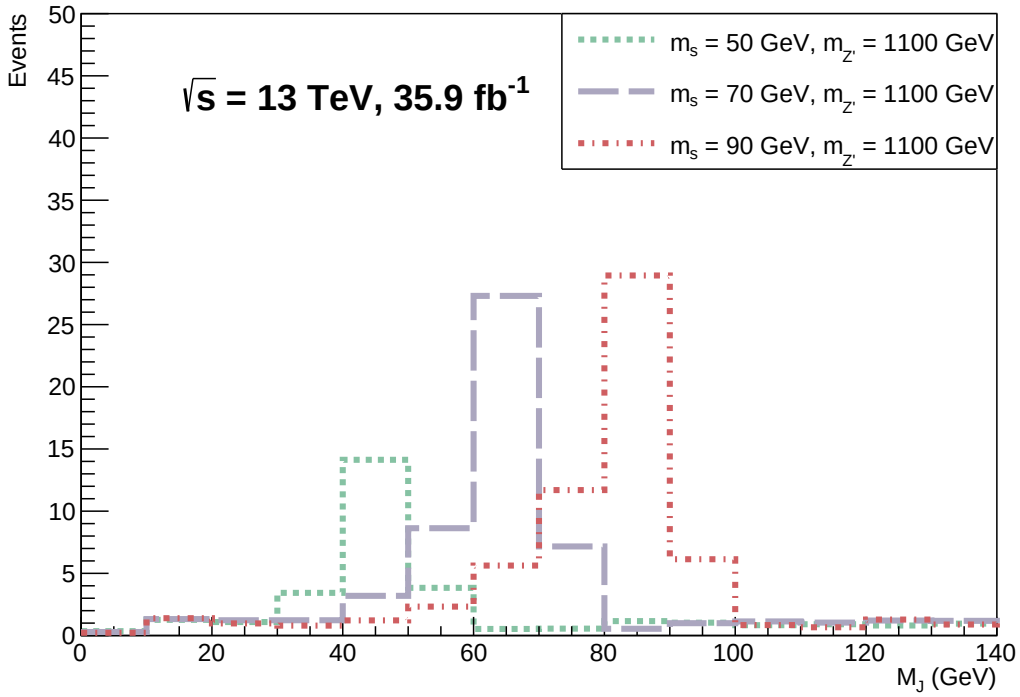

(a) Signal processes with different m_s

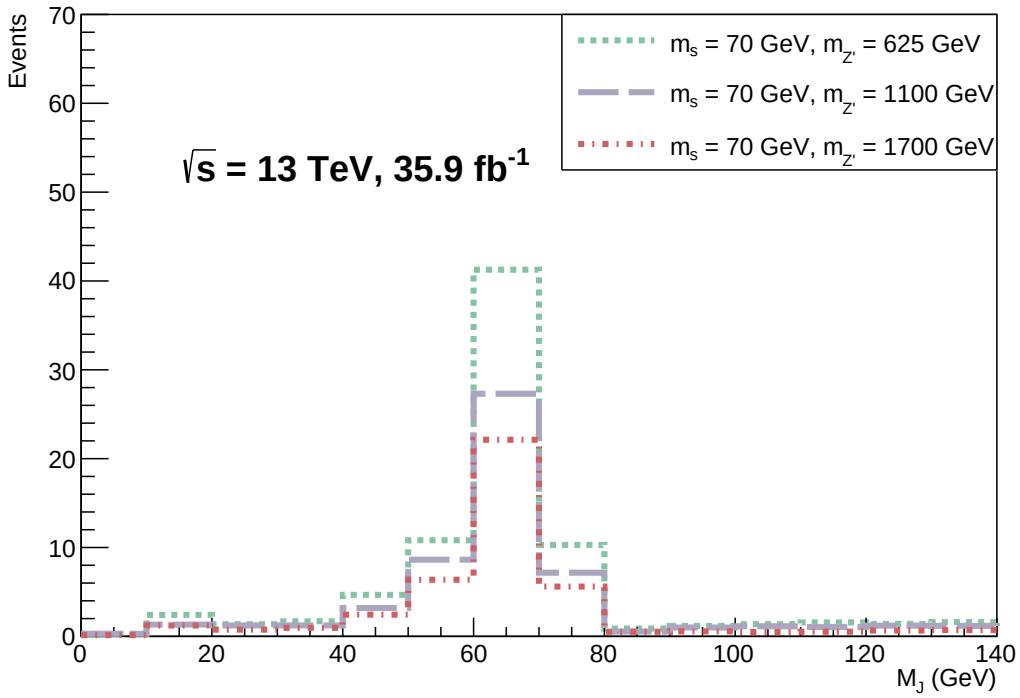

(b) Signal processes with different $m_{Z'}$

Figure 4.4: Reconstructed large-radius jet mass distributions for signal processes with different m_s and different $m_{Z'}$ with an integrated luminosity of 35.9 fb^{-1}. Signal processes are chosen according to the Ref. [1] preference and the coupling scenarios are the same as the LHC preference [37].

m_s [GeV]	mass range for the reconstructed large-radius jet
50	(30, 60)
70	(50, 80)
90	(60, 90)

Table 4.2: Expected mass windows in the different m_s distributions of the reconstructed large-radius jet mass. Mass windows are set to maximise the expected significance.

4.3.3 Expected signal and background yields

Table 4.3, Table 4.4 and Table 4.5 respectively show the yield numbers of three different m_s values after each event selection using the mass windows presented in Table 4.2. The background yield numbers are also presented in the same tables and the SM background uncertainties are computed by taking the relative uncertainties from the ATLAS paper [9]. The coupling scenario used by the LHC working group [37] has been assumed in this study. The signal samples are chosen to cover a wide range of $m_{Z'}$ as in Ref. [1]. All the simulated yield numbers for signal and background samples have been scaled to an integrated luminosity of 35.9 fb^{-1}.

Table 4.3, Table 4.4 and Table 4.5 show the number of events in the mass window for each signal we have taken into consideration.

By comparing SG/BG (signal over background) ratios in Table 4.3 with Table 4.4 and Table 4.5, one can easily conclude that the cut $N_{fat-jet} = 1$ does not provide any improvement to this ratio for the dark Higgs mass $m_s = 50$ GeV. Further studies can determine a m_s threshold for which this selection provides a sensible improvement to the overall SG/BG ratio. Removing the $N_{fat-jet} = 1$ selection for the $m_s = 50$ GeV study may increase the overall number of collected signal events, thus reducing the relative statistical uncertainty.

All these selections are applied in a no-pile-up scenario, which represents the most optimistic situation. However, this may change once pile-up is introduced and a re-optimisation of these selections may be required.

35.9fb^{-1}	MET > 500 GeV	$N_{fat-jet} = 1$	No isolated leptons	30 GeV < M_J < 60 GeV
SM BG	4898.00	403.15	180.90	9.22±1.04
$m_{Z'} = 0.5$ TeV	654.41	58.72	58.67	32.07
$m_{Z'} = 1$ TeV	387.69	45.88	45.88	25.28
$m_{Z'} = 2$ TeV	142.75	18.03	18.03	10.25

Table 4.3: Predicted yield numbers for SM background and different signal samples with an integrated luminosity of 35.9 fb^{-1}. The signal samples are chosen as $g_x = 1$, $g_q = 0.25$ and $m_{\mathrm{DM}} = 100$ GeV at $m_s = 50$ GeV as in Ref. [1]. The SM background uncertainties are computed by taking the relative uncertainties from the ATLAS paper [9].

35.9fb^{-1}	MET > 500 GeV	$N_{fat-jet} = 1$	No isolated leptons	50 GeV < M_J < 80 GeV
SM BG	4898.00	403.15	180.90	20.68±1.95
$m_{Z'} = 0.5$ TeV	538.85	110.06	110.02	76.92
$m_{Z'} = 1$ TeV	349.80	75.37	75.32	48.70
$m_{Z'} = 2$ TeV	140.02	37.38	37.32	25.73

Table 4.4: Predicted yield numbers for SM background and different signal samples with an integrated luminosity of 35.9 fb^{-1}. The signal samples are chosen as $g_x = 1$, $g_q = 0.25$ and $m_{\mathrm{DM}} = 100$ GeV at $m_s = 70$ GeV as in Ref. [1]. The SM background uncertainties are computed by taking the relative uncertainties from the ATLAS paper [9].

35.9fb^{-1}	MET > 500 GeV	$N_{fat-jet} = 1$	No isolated leptons	60 GeV < M_J < 90 GeV
SM BG	4898.00	403.15	180.90	29.06±2.49
$m_{Z'} = 0.5$ TeV	458.83	128.77	128.62	86.13
$m_{Z'} = 1$ TeV	317.72	83.11	83.11	51.98
$m_{Z'} = 2$ TeV	134.40	45.69	45.61	29.64

Table 4.5: Predicted yield numbers for SM background and different signal samples with an integrated luminosity of 35.9 fb^{-1}. The signal samples are chosen as $g_x = 1$, $g_q = 0.25$ and $m_{\mathrm{DM}} = 100$ GeV at $m_s = 90$ GeV as in Ref. [1]. The SM background uncertainties are computed by taking the relative uncertainties from the ATLAS paper [9].

4.3.4 Exclusion limits

HiggsCombineTool from **CMSSW_8_1_0** [53] is used to calculate the median experimental sensitivity together with one (two) standard deviation confidence intervals [52]. Different methods are provided by **HiggsCombineTool** to generate expected sensitivities [52]. In this analysis expected sensitivities are computed using the the asymptotic approximation [34], the fastest and simplest technique provided by the tool. In this method, CL is calculated using an asymptotic approximation of the statistic under the signal and background hypotheses [57]. The excluded ratio of the signal cross-section to the predicted cross-section, σ/σ_{th}, with an integrated luminosity of 35.9 fb^{-1} is obtained after running **HiggsCombineTool**. Finally, the upper limits are drawn using the linear interpolation [58] because our signal samples are discrete. The results are displayed in the $m_{Z'} - m_{\mathrm{DM}}$ plane and regions where σ/σ_{th} ratio is less than one are considered as excluded regions. 95% CL means that if the signal were to be there, there is only a 5% (100% - 95%) chance we would miss it.

The number of background and signal events, together with their relative statistic and systematic uncertainties, are inputs in **HiggsCombineTool**. The SM background statistic uncertainties are computed by taking the relative uncertainties from the ATLAS paper [9]. As in Ref. [59, 60], we use an additional 8% as our SM background systematic uncertainties for the large-radius jet tagging. A DM search with a SM Higgs decaying into a boosted $b\bar{b}$ pair is performed in Ref. [61]. In this search, a large-radius jet is also reconstructed to find the Higgs decay products. Based on the similarities between our implementation and Ref. [61], we use 15% as our signal systematic uncertainty.

In this section, signal events with two types of coupling scenario are considered under m_s ranging from 50 GeV to 90 GeV. The 95% CL upper limits for fixed m_{DM} will be given as examples. Here, we choose $m_s = 70$ GeV, $g_x = 1$ and $g_q = 0.25$ as an example. For the rest of signal samples, their 1-D projections for fixed m_{DM} can be found in Appendix A.

Signal samples with coupling scenario same as the LHC recommendation: Figure 4.5 (a), (b) and (c) respectively show the upper limits of $m_s = 50$, 70 and 90 GeV at 95% CL with an integrated luminosity of 35.9 fb^{-1}. The solid red line is the

expected upper limit. One (two) standard deviation curves due to experimental uncertainty have been drawn in dashed red (purple). The region below the expected upper limit is excluded at 95% CL.

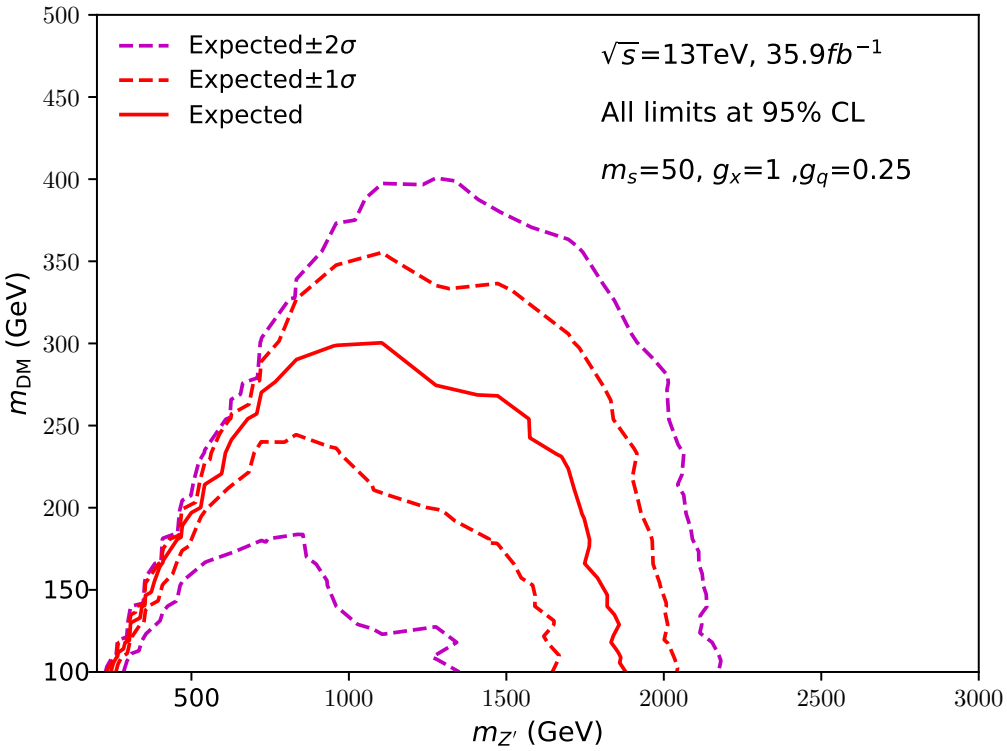

(a) $m_s = 50$ GeV, $g_x = 1$ and $g_q = 0.25$

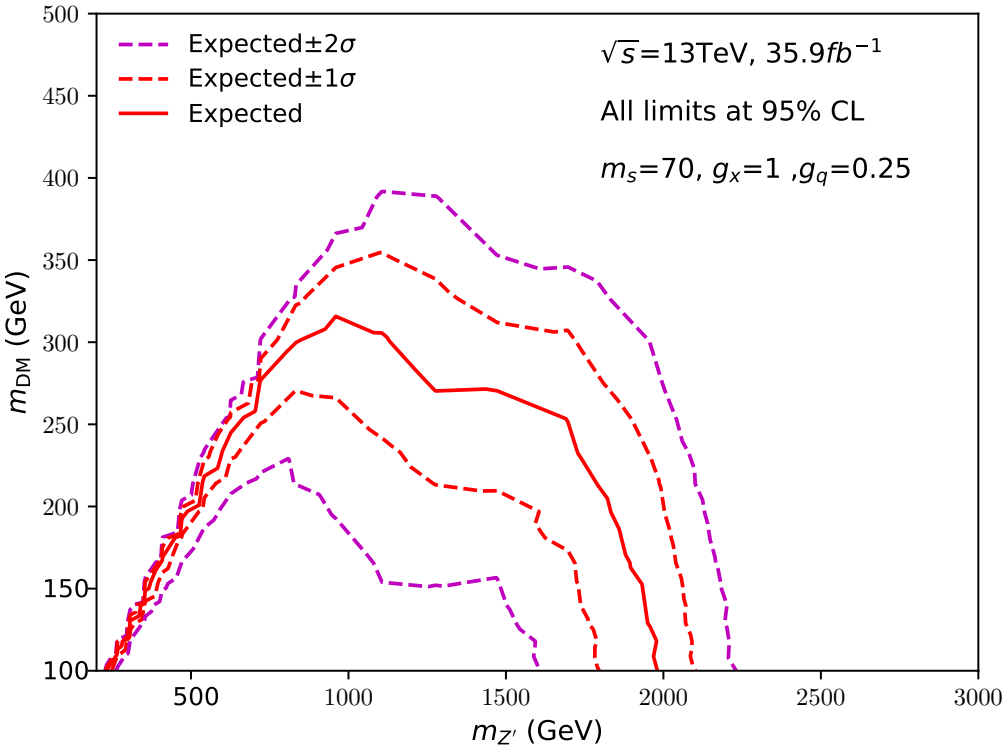

(b) $m_s = 70$ GeV, $g_x = 1$ and $g_q = 0.25$

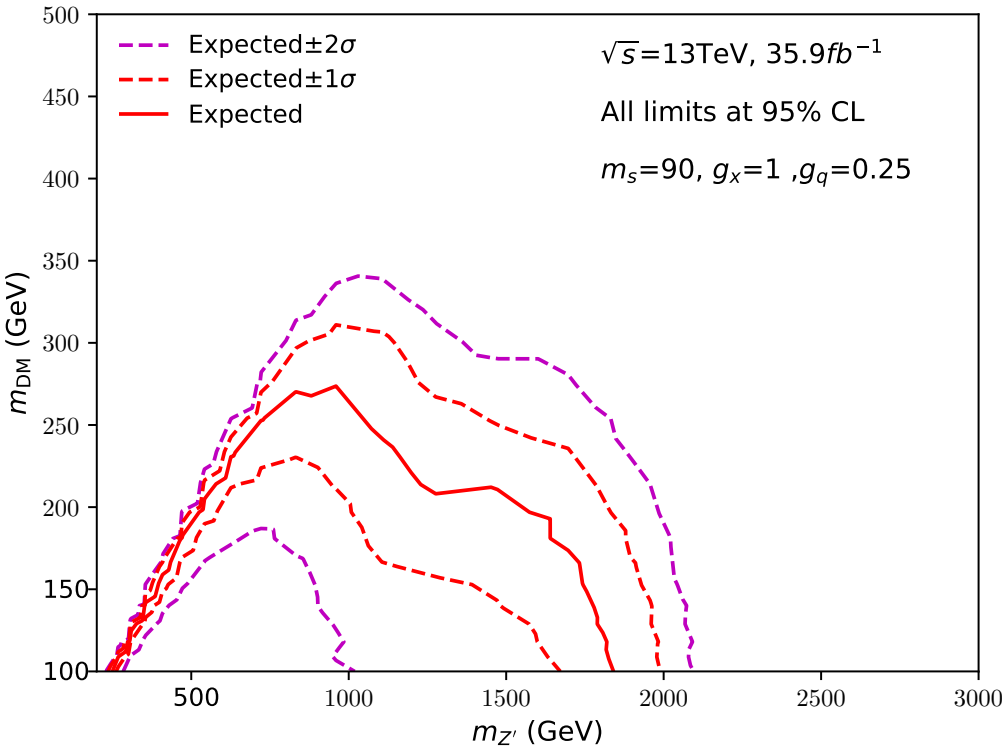

(c) $m_s = 90$ GeV, $g_x = 1$ and $g_q = 0.25$

Figure 4.5: The expected exclusion region of the large-radius jet analysis at 95% CL with an integrated luminosity of 35.9 fb^{-1} at a centre-of-mass energy of 13 TeV. The inputs all correspond to $m_s = 50$, 70 and 90 GeV. The couplings are set according to the LHC recommendation [37]. The solid red line shows the expected upper limit and one (two) standard deviations arising from experimental uncertainties have been drawn using dashed red (purple) lines.

Signal events with coupling scenario considering DM relic abundance constraints from the universe: Figure 4.6 (a), (b) and (c) respectively show the upper limits for $m_s = 50$, 70 and 90 GeV at 95% CL with an integrated luminosity of 35.9 fb^{-1}. The solid red line is the expected upper limit and one (two) standard deviations have been drawn using dashed red (purple) lines from experimental uncertainties. All the regions below the expected upper limit is excluded at 95% CL. The dashed blue line indicates the region with $g_x = (4\pi)^{1/2}$ beyond which the theory becomes non-perturbative.

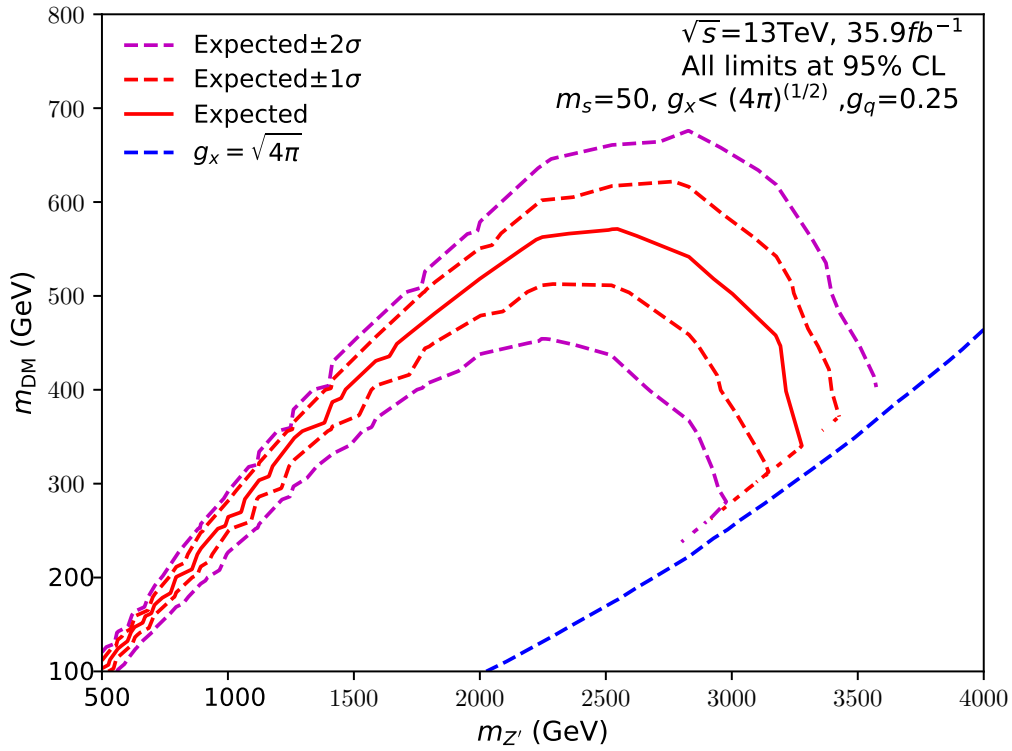

(a) $m_s = 50$ GeV, $g_x < (4\pi)^{1/2}$ and $g_q = 0.25$

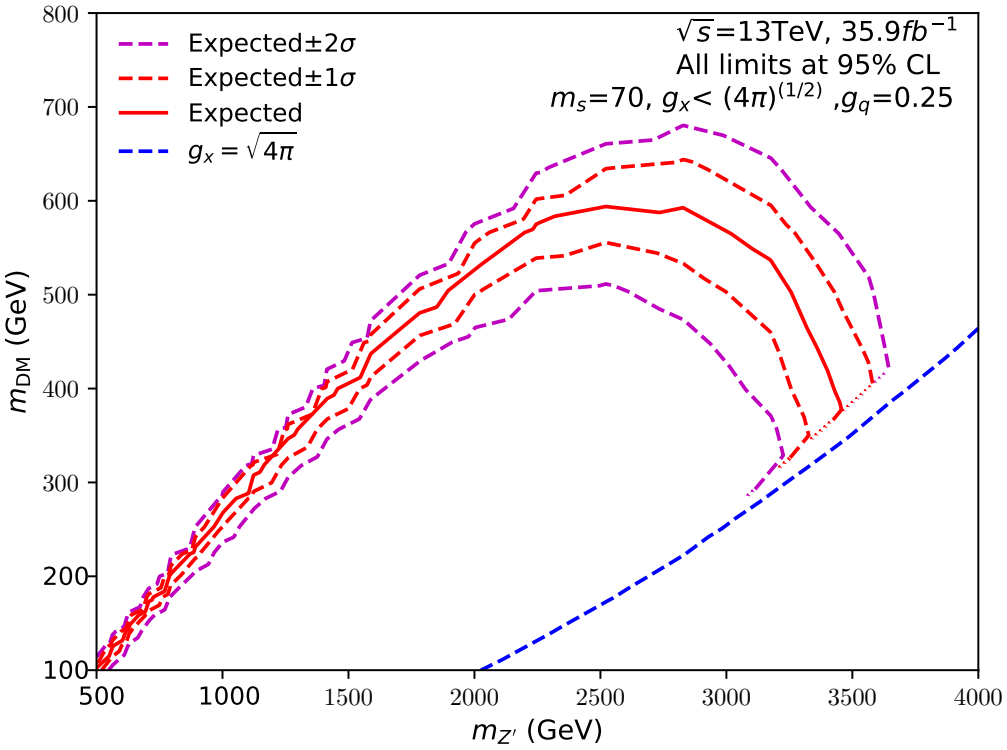

(b) $m_s = 70$ GeV, $g_x < (4\pi)^{1/2}$ and $g_q = 0.25$

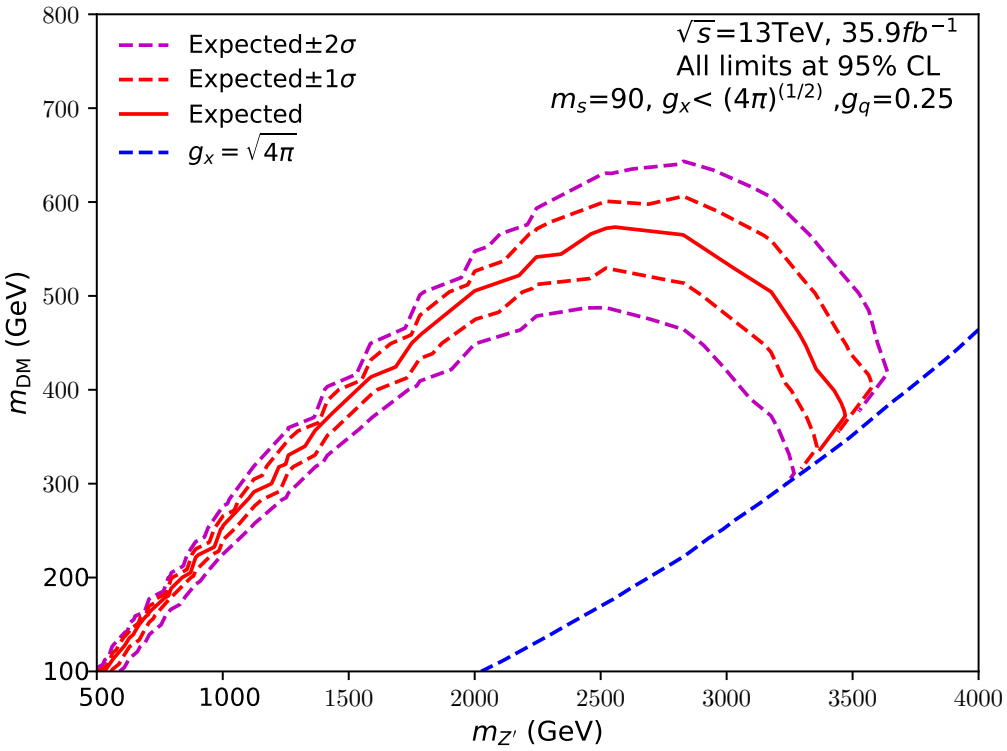

(c) $m_s = 90$ GeV, $g_x < (4\pi)^{1/2}$ and $g_q = 0.25$

Figure 4.6: The expected exclusion region of the large-radius jet analysis at 95% CL with an integrated luminosity of 35.9 fb^{-1} at a centre-of-mass energy of 13 TeV. The inputs all correspond to $m_s = 50$, 70 and 90 GeV. The coupling g_x is chosen to fulfil the relic density constraint [2]. The solid red line shows the expected upper limit and one (two) standard deviations from experimental uncertainties have been drawn using dashed red (purple) lines. All the regions below the expected upper limits are excluded. The dashed blue line indicates the region where $g_x = (4\pi)^{1/2}$.

Figure 4.5 and 4.6 show smaller uncertainties for expected upper limits at low $m_Z^{'}$ than at high $m_Z^{'}$. Higher centre-of-mass energies are required at high $m_{Z'}$. Therefore, lower numbers of signal events are expected at high $m_{Z'}$. This can lead to higher relative statistical uncertainties and larger uncertainty bands on the expected limits at high $m_{Z'}$.

Exclusion limits at fixed $\mathbf{m_{DM}}$ = 100 GeV and 301 GeV for $\mathbf{m_s}$ = 70 GeV, $\mathbf{g_x}$ = 1 and $\mathbf{g_q}$ = 0.25: 95% CL upper limits for fixed m_{DM} can help in understanding the 2-D exclusions. We consider signals with $m_s = 70$ GeV, $g_x = 1$ and $g_q = 0.25$ as an example. Their 1-D projections for fixed m_{DM} are shown in Fig. 4.7.

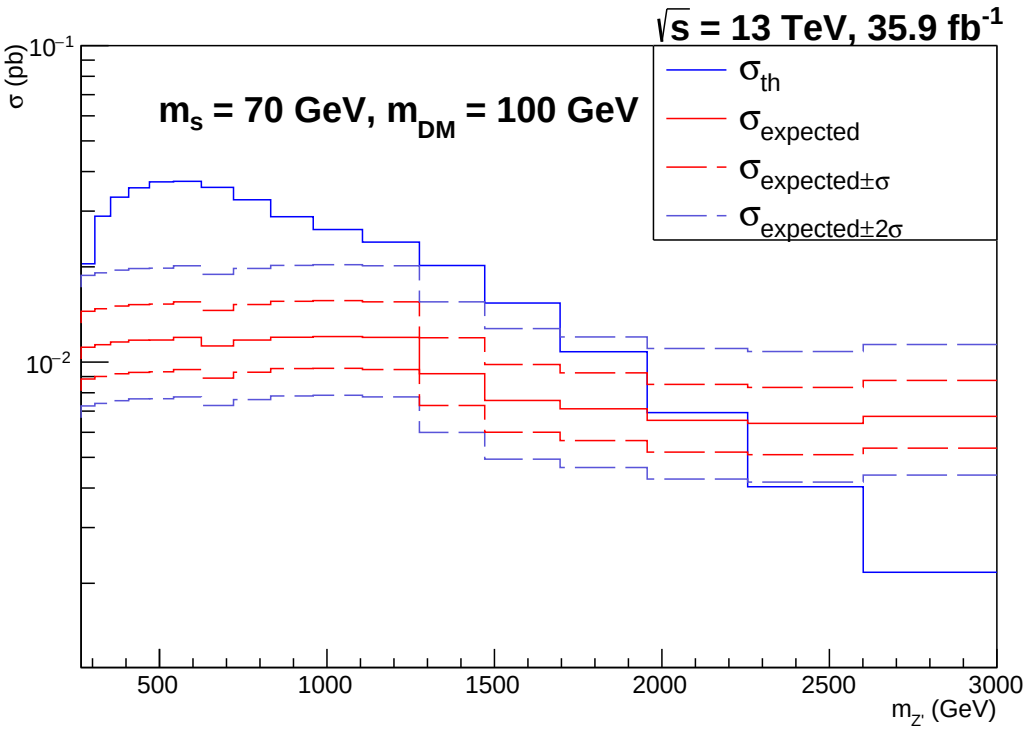

(a) $m_s = 70$ GeV, $m_{\mathrm{DM}} = 100$ GeV, $g_x = 1$ and $g_q = 0.25$

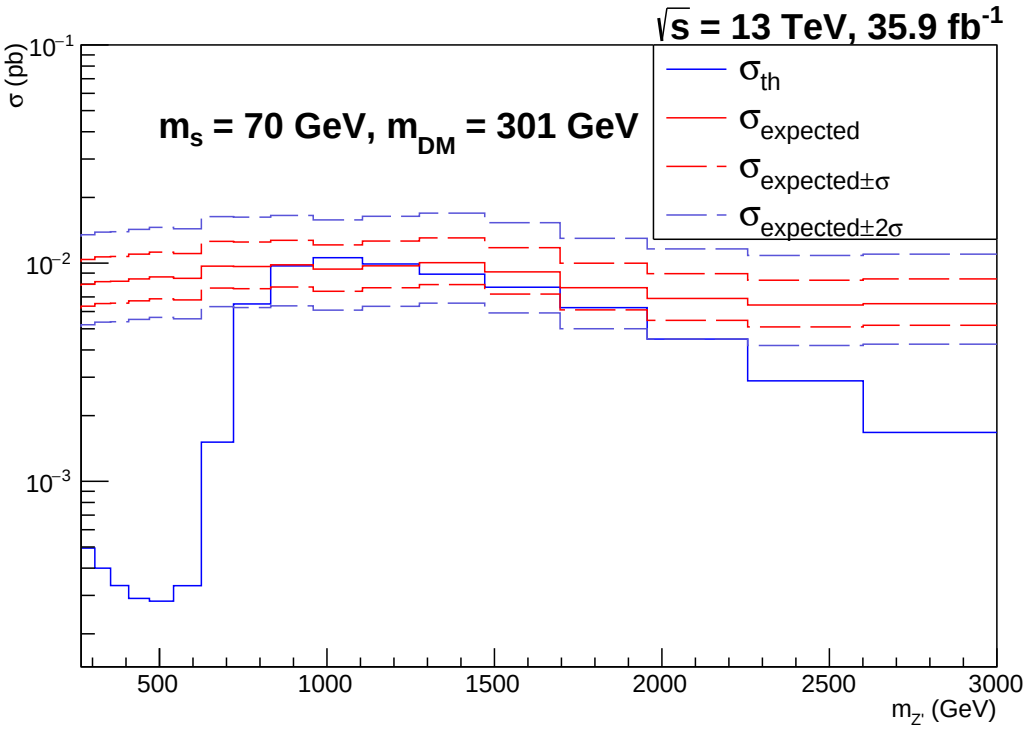

(b) $m_s = 70$ GeV, $m_{\mathrm{DM}} = 301$ GeV, $g_x = 1$ and $g_q = 0.25$

Figure 4.7: Expected 95% CL limits for $m_s = 70$ GeV with $m_{\mathrm{DM}} = 100$ and 301 GeV. The couplings are set according to the LHC recommendation [37]. The theoretical cross-section is shown as the blue solid line.

Figure 4.7 (b) shows the theoretical cross-section and the expected upper limit on the cross-section with an integrated luminosity of 35.9 fb^{-1} for the boosted dark Higgs search as a function of $m_{Z'}$ for $m_s = 70$ GeV, $m_{\mathrm{DM}} = 301$ GeV, $g_x = 1$ and $g_q = 0.25$. For $m_{Z'} < 600$ GeV region, the theoretical cross-section is two orders of magnitude smaller than that in the $m_{Z'} > 600$ region. As shown in Fig. 2.4 (b), $m_{Z'}$ needs to be > 600 GeV so it can decay into two DM particles of 301 GeV. The theoretical cross-section as a function of the generator-level $Z^{'}$ mass is plotted in solid blue in Fig. 4.7 (b). The $Z^{'}$ decay width, which has been set to 10 GeV, influences the slope of the curve in the 600-800 GeV range.

The theoretical cross-section exponentially decreases with the centre-of-mass energy, except for the resonance region where $\sqrt{s} \approx m_{Z'}$. As shown in Fig. 4.7 (b), for $m_{Z'}$ between 600 GeV and 800 GeV, the theoretical cross-section increases as contribution from resonant $Z^{'}$ production adds to this process. For $m_{Z'}$ between 1000 GeV and 3000 GeV in Fig. 4.7 (b), the centre-of-mass energies required to generate the on-shell $Z^{'}$ are suppressed by the parton distribution function (PDF). Therefore, we see a falling cross-section again in this range.

For the rest of signal samples, their 1-D projections for fixed m_{DM} can be found in Appendix A.

5 Dark Higgs search with jets and MET (α_T) analysis

This section focuses on the reinterpretation of the CMS α_T analysis. The α_T analysis is a generic analysis used to search for new physics like supersymmetry (SUSY) and DM. The α_T analysis used in both Ref. [11] and Ref. [12] can be reinterpreted in terms of the 'Higgs Portal DM' model. To estimate backgrounds in this reinterpretation, we use the data recorded by the CMS experiment in 2016 together with the estimated background numbers provided in Ref. [12]. We validate our signal generation procedure by comparing with a SUSY benchmark point that is also used in Ref. [12], and that has a similar final state as the 'Higgs Portal DM' model.

Section 5.1 concentrates on the event reconstruction and selection of the CMS α_T analysis. We employ the very same method as Ref. [12] for consistency. In Section 5.2, we investigate our reconstruction performance for the SUSY T2bb model and we discuss the similarities between SUSY T2bb signature and our simulation. The accuracy of our event selection can be tested by comparing our SUSY T2bb results with published results from Ref. [11] and Ref. [12]. Finally, Section 5.3 contains all the results of our reinterpretation.

The SUSY T2bb samples are generated to compare the accuracy between our reinterpretation and the published results from Ref. [11] and Ref. [12]. The diagram for the SUSY T2bb model can be found in Fig. 5.1: a pair of bottom squarks ($\tilde{b}$) is produced and then decays into bottom quarks and lightest supersymmetric particles (LSPs). This has a very similar experimental signature as our 'Higgs Portal DM' model.

All signal events are generated by **MadGraph5_aMC@NLO v2.3.3** [47] in the two coupling scenarios presented in Section 3.2 for the dark Higgs mass m_s ranging from 50 GeV to 90 GeV. To estimate backgrounds in this reinterpretation, we use the data recorded by the CMS experiment in 2016 together with the estimated background numbers provided in Ref. [12]. **Pythia 8** [48] and **Rivet v2.5.2** [49] are used for showering and event selection. We use the same event selection as in Ref. [12]. As the dataset in Ref. [12] is binned in 224 bins, we select the most sensitive ones for our analysis using the Asimov Test [62]. Finally, **HiggsCombineTool** [52] from **CMSSW_8_1_0** [53] is applied to calculate the expected and observed exclusion

upper limits at 95% confidence level (CL) [32,33] based on the selected most sensitive bins. The upper limits are calculated based on the excluded ratio of the signal cross-section to the predicted cross-section, σ/σ_{th}, with an integrated luminosity of 35.9 fb^{-1}.

5.1 Interpretation of the α_T analysis

The event selection of the CMS α_T analysis has been implemented in this section. In this analysis, jets are defined using the anti-k_t algorithm [28] with ΔR = 0.4. This analysis uses the number of jets, n_{jet}, the number of jets stemming from b-quark decays, n_b, the total visible hadronic energy, H_T, and the missing energy, H_T^{miss}, as discriminating variables. While our expected signal consists of two b-jets and missing energy, we allow for extra jets from initial or final state radiation. All the events are generated by **MadGraph5_aMC@NLO v2.3.3** [47]. **Pythia 8** [48] and **Rivet v2.5.2** [49] are respectively used for showering, and detector modelling and event selection. Table 5.1 taken from Ref. [12] shows the event selection requirements used for the signal region. Pile-up is not simulated for these signal samples. A smearing has been applied to specific jet kinematic variables in order to take account for the detector jet reconstruction performance. An approximated detector response is performed in the **Rivet v2.5.2** analysis by taking the b-tagging efficiency [12] and mass resolution [44] into account. b-tagging [12] is used to identify jets coming from the dark Higgs. As in CMS [12], we assume an average efficiency of 69% in identifying sub-jets containing b-hadrons and a misidentification probability of 18% for c-quark jets and 1% for light-flavoured jets. Mass smearing is applied as in Section 4.1.2 by considering 10% resolution, the same performance as in ATLAS [44]. To simplify this detector approximation, no transverse momentum (p_T) smearing has been applied to this reinterpretation.

5.1.1 Event selections

The **Rivet v2.5.2** analysis has been set up as follows. Both track jets and calo-jets are reconstructed through **FastJet v3.2.0** [54] and anti-k_t algorithm [28] with a size parameter of 0.2 and 0.4, respectively. Events are vetoed if they contain an isolated electron [63] or muon [64] with $p_T > 10$ GeV to exclude charged leptons coming from any source other than b-quark decays. Track jet can be matched to a calo-jet

Physics object acceptances		
Jet	$p_T > 40$ GeV, $\|\eta\| < 2.4$	
Photon	$p_T > 25$ GeV, $\|\eta\| < 2.5$, isolated in cone $\Delta R < 0.3$	
Electron	$p_T > 10$ GeV, $\|\eta\| < 2.5$, $I^{rel} < 0.1$ in cone $0.05 < \Delta R(p_T) < 0.2$	
Muon	$p_T > 10$ GeV, $\|\eta\| < 2.5$, $I^{rel} < 0.2$ in cone $0.05 < \Delta R(p_T) < 0.2$	
Single isolated track (SIT)	$p_T > 10$ GeV, $\|\eta\| < 2.5$, $I^{track} < 0.1$ in cone $\Delta R < 0.3$	
Baseline event selection		
All-jet f nal state	Veto events containing photons, electrons, muons, and SITs within acceptance	
p_T^{miss} quality	Veto events based on f lters related to beam and instrumental effects	
Jet quality	Veto events containing jets that fail identif cation criteria or $0.1 < f_{h^\circ}^{j_1} < 0.95$	
Jet energy and sums	$p_T^{j_1} > 100$ GeV, $H_T > 200$ GeV, $H_T^{miss} > 200$ GeV	
Jets outside acceptance	$H_T^{miss}/p_T^{miss} < 1.25$, veto events containing jets with $p_T > 40$ GeV and $\|\eta\| > 2.4$	
Signal region	Baseline selection +	
α_T threshold (H_T range)	0.65 (200–250 GeV), 0.60 (250–300), 0.55 (300–350), 0.53 (350–400), 0.52 (400–900)	
$\Delta\varphi^*_{min}$ threshold	$\Delta\varphi^*_{min} > 0.5$ ($n_{jet} \geq 2$), $\Delta\varphi^{*_{25}}_{min} > 0.5$ ($n_{jet} = 1$)	
Nominal categorization schema		
n_{jet}	1	(monojet)
	≥2a	(a denotes asymmetric, $40 < p_T^{j_2} < 100$ GeV)
	2, 3, 4, 5, ≥6	(symmetric, $p_T^{j_2} > 100$ GeV)
n_b	0, 1, 2, 3, ≥4	(can be dropped/merged vs. n_{jet})
H_T boundaries	200, 400, 600, 900, 1200 GeV	(can be dropped/merged vs. n_{jet}, n_b)
H_T^{miss} boundaries	200, 400, 600, 900 GeV	(can be dropped/merged vs. n_{jet}, n_b, H_T)

Table 5.1: The event selection requirements used in signal regions and control regions. Table taken from [12].

if the distance between the closest track jet and a calo-jet is less than 0.4. Events are also vetoed if they contain an isolated photon [65] with $p_T > 25$ GeV. Calo-jets are required to have $p_T > 40$ GeV and $|\eta| < 3.0$. Events containing only one calo-jet are vetoed and the most energetic calo-jet in every selected event is required to have $p_T > 100$ GeV and $|\eta| < 2.5$. The missing transverse momentum (MET) is calculated as the negative vector sum of the momentum of all the final-state hadrons and charged leptons. The total hadronic energy in the event H_T is calculated as the total scalar sum of all calo-jets, $H_T = \sum_{i=1}^{N_{jet}} p_T^{j_i}$. The negative vector sum of all calo-jets, defined as $H_T^{miss} = -|\sum_{i=1}^{N_{jet}} \mathbf{p}_T^{j_i}|$, is used in this analysis for estimating MET and H_T^{miss}/MET is required to be less than 1.25.

$H_T > 200$ GeV and $H_T^{miss} > 130$ GeV are required in each event as a baseline selection. The α_T variable [11,66–69] is introduced here to suppress multi-jet events with MET originating from mismeasurements. For di-jets events, α_T is defined as

$$\alpha_T = \frac{p_T^{j_2}}{M_T},$$
$$M_T = \sqrt{(\sum_{i=1}^{2} p_T^{j_i})^2 - (\sum_{i=1}^{2} p_x^{j_i})^2 - (\sum_{i=1}^{2} p_y^{j_i})^2} = \sqrt{(H_T)^2 - (H_T^{miss})^2}, \tag{5.1}$$

where $p_T^{j_2}$ refers to the transverse momentum of the less energetic calo-jet and the M_T is the transverse mass of the di-jet system. For multi-jet events that contain more than 2 jets, an equivalent α_T variable can be reconstructed by combining two pseudo-jets [69]. This equivalent system is formed by finding the di-jet system that minimises the H_T difference(ΔH_T) between the two pseudo-jets. The two pseudo-jets and the definition of α_T for more than 2-jet system is

$$\alpha_T = \frac{1}{2}\frac{H_T - \Delta H_T}{\sqrt{{H_T}^2 - (H_T^{miss})^2}}. \tag{5.2}$$

In this analysis, an H_T-dependent α_T selection has been applied to optimise background suppression. The azimuthal angle variable ($\Delta\phi^*_{min}$) is the minimum angle between one jet and the H_T^{miss} from all the rest jets in the same event [70]. Requiring $\Delta\phi^*_{min} > 0.5$ rejects events where H_T^{miss} is pointing in the direction of a (mismeasured) jet.

5.2 Validation

In order to verify our implementation of the CMS α_T analysis event selection, we compare the selection efficiency at every step of the event selection. All the CMS α_T analysis data shown in Table 5.2, Table 5.3, Table 5.4 and Table 5.5 are taken from both Ref. [11] and Ref. [12]. As will be discussed below, we validated our selection and the kinematic distribution against Ref. [11]. During the course of this work, Ref. [12] appeared and we updated and validated our event selection against this reference which is used for the final results. The modelling of the kinematic distributions should be unaffected by this change. We compare the event selection for two SUSY T2bb models: T2bb(375, 300) and T2bb(800, 50) for comparison with Ref. [11], and T2bb(1000, 100) and T2bb(550, 450) for comparison with Ref. [12]. In all the T2bb sample names, the first number refers to the mass of bottom squark ($m_{\tilde{b}}$) and the second number refers to the mass of lightest supersymmetric particle (m_{LSPs}).

The diagram for the SUSY T2bb model can be found in Fig. 5.1. Bottom squarks ($\tilde{b}$) are generated and decay into b quarks and the lightest supersymmetric particles (LSPs). The SUSY T2bb model is parameterised in terms of the mass of bottom squark ($m_{\tilde{b}}$) and LSP (m_{LSP}). The experimental signature for SUSY T2bb is two

b-tagged jets with large MET from LSPs, which is similar to our 'Higgs Portal DM' experimental signature where we also expect two b-tagged jets with large MET from DM production. Therefore, it is reasonable to compare SUSY T2bb results.

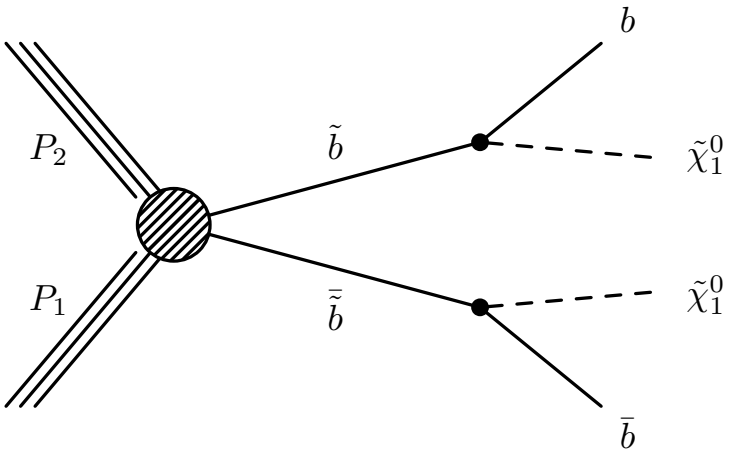

Figure 5.1: Diagram of the SUSY T2bb model. The diagram shows the direct production of bottom squarks. The dashed area represents a model-dependent process that can produce a pair of bottom squarks. Figure taken from [11].

For each T2bb sample considered, a table has been built for comparing the inclusive and exclusive signal efficiency between CMS simulation results and our reinterpretation results after each selection as shown in Section 5.2.1 (Table 5.2 to Table 5.5). The exclusive signal efficiency is the efficiency of that specific selection step and the inclusive signal efficiency is the cumulative efficiency of every selection step. Because the α_T analysis considers four variables (n_{jet}, n_b, H_T, H_T^{miss}), the distributions of these variables are shown in Fig. 5.2 and 5.3 as a comparison with Ref. [11]. The four variables are compared before and after selections as shown in Section 5.2.2.

5.2.1 Cutflow tables

Table 5.2 and Table 5.3 present the comparison between our reinterpretation and the CMS simulation from Ref. [11]. We can conclude that the maximum difference for T2bb(375,300) between our reconstruction and CMS simulation is 9% and the maximum difference for T2bb(800,50) between our reconstruction and CMS simulation is 5%. Following the publication of Ref. [12], we updated our event selection against this reference (see Table 5.4 and Table 5.5). Ref. [12] is used for the final results of our reinterpretation. It can be concluded that the maximum difference

for T2bb(1000,100) between our reconstruction and CMS simulation is 11% and the maximum difference for T2bb(550,450) between our reconstruction and CMS simulation is 14%.

2.3 fb^{-1}	*RA*1		*Rivet*		Diff.(*RA*1/*Rivet*)	
	incl.	excl.	incl.	excl.	incl.	excl.
begin	100		100			
lep veto	99	0.99	100	1.00	0.95	0.99
track jet matching	94	0.95	100	1.00	1.01	0.95
photon veto	94	1.00	99.3	0.99	0.95	1.01
fwd. jet veto	81	0.86	89.9	0.91	1.04	0.95
$N_{jet} > 2$	61	0.75	65.3	0.73	0.98	1.04
$p_T^{j_1} > 100$	36	0.59	39.4	0.60	1.00	0.98
$\lvert\eta^{j_1}\rvert < 2.5$	34	0.94	37.3	0.95	0.99	1.00
$H_T > 200$	30	0.88	33.2	0.89	0.95	0.99
$H_T^{miss} > 130$	18	0.60	21.0	0.63	0.91	0.95
$\frac{H_T^{miss}}{E_T^{miss}} < 1.25$	15	0.83	19.2	0.91	1.07	0.91
α_T	7.2	0.48	8.6	0.45	0.98	1.07
$\Delta\phi^*_{min}$	4.5	0.63	5.5	0.64	0.99	0.98

Table 5.2: Inclusive and exclusive signal efficiency comparison for T2bb(375,300) between CMS-SUS-15-005 α_T analysis (RA1) [11] and this search (Rivet). The CMS-SUS-15-005 analysed samples correspond to an integrated luminosity of 2.3 fb^{-1} at a centre-of-mass energy of 13 TeV.

2.3 fb^{-1}	*RA*1		*Rivet*		Diff.(*RA*1/*Rivet*)	
	incl.	excl.	incl.	excl.	incl.	excl.
begin	100		100			
lep veto	99	0.99	100	1.00	0.97	0.99
track jet matching	96	0.97	100	1.00	1.00	0.97
photon veto	95	0.99	99.1	0.99	0.95	1.00
fwd. jet veto	81	0.85	88.8	0.90	1.00	0.95
$N_{jet} > 2$	80	0.99	88.0	0.99	1.00	1.00
$p_T^{j_1} > 100$	80	1.00	87.9	1.00	1.00	1.00
$\lvert\eta^{j_1}\rvert < 2.5$	80	1.00	87.5	1.00	1.00	1.00
$H_T > 200$	80	1.00	87.5	1.00	1.01	1.00
$H_T^{miss} > 130$	75	0.94	81.6	0.93	1.00	1.01
$\frac{H_T^{miss}}{E_T^{miss}} < 1.25$	72	0.96	78.4	0.96	1.02	1.00
α_T	62	0.86	65.9	0.84	0.98	1.02
$\Delta\phi^*_{min}$	39	0.63	42.5	0.64	0.99	0.98

Table 5.3: Inclusive and exclusive signal efficiency comparison for T2bb(800,50) between CMS-SUS-15-005 α_T analysis (RA1) [11] and this search (Rivet). The CMS-SUS-15-005 analysed samples correspond to an integrated luminosity of 2.3 fb^{-1} at a centre-of-mass energy of 13 TeV.

35.9 fb^{-1}	*RA*1		*Rivet*		Diff.(*RA*1/*Rivet*)	
	incl.	excl.	incl.	excl.	incl.	excl.
begin	100		100			
lep veto	100	1.00	99.9	1.00	0.97	1.00
track jet matching	97	0.97	99.9	1.00	1.00	0.97
photon veto	96	0.99	98.8	0.99	0.99	1.00
$N_{jet} > 2$	95	0.99	98.4	1.00	0.96	0.99
$p_T^{j_1} > 100$	91	0.96	98.4	1.00	1.00	0.96
$H_T > 200$	91	1.00	98.3	1.00	1.00	1.00
$H_T^{miss} > 200$	82	0.90	88.6	0.90	1.11	1.00
fwd. jet veto($\lvert\eta^{j_1}\rvert < 2.4$)	70	0.85	67.9	0.77	1.02	1.11
$\frac{H_T^{miss}}{E_T^{miss}} < 1.25$	70	1.00	66.4	0.98	1.00	1.02
α_T	62	0.89	58.9	0.89	0.97	1.00
$\Delta\phi^*_{min}$	40	0.65	39.2	0.67	1.00	0.97

Table 5.4: Inclusive and exclusive signal efficiency comparison for T2bb(1000,100) between CMS-SUS-16-038 α_T analysis (RA1) [12] and this search (Rivet). The CMS-SUS-16-038 analysed samples correspond to an integrated luminosity of 35.9 fb^{-1} at a centre-of-mass energy of 13 TeV.

35.9 fb^{-1}	*RA*1		*Rivet*		Diff.(*RA*1/*Rivet*)	
	incl.	excl.	incl.	excl.	incl.	excl.
begin	100		100			
lep veto	99	0.99	100.0	1.00	0.96	0.99
track jet matching	95	0.96	100.0	1.00	1.01	0.96
photon veto	95	1.00	99.2	0.99	0.96	1.01
$N_{jet} > 2$	79	0.83	85.5	0.86	0.89	0.96
$p_T^{j_1} > 100$	52	0.66	63.0	0.74	0.95	0.89
$H_T > 200$	45	0.87	57.6	0.91	0.99	0.95
$H_T^{miss} > 200$	18	0.40	23.3	0.40	1.14	0.99
fwd. jet veto($\lvert\eta^{j_1}\rvert < 2.4$)	15	0.83	17.0	0.73	0.97	1.14
$\frac{H_T^{miss}}{E_T^{miss}} < 1.25$	14	0.93	16.3	0.96	1.03	0.97
α_T	9	0.64	10.2	0.63	1.02	1.03
$\Delta\phi^*_{min}$	6.3	0.70	7.0	0.69	0.99	1.02

Table 5.5: Inclusive and exclusive signal efficiency comparison for T2bb(550,450) between CMS-SUS-16-038 α_T analysis (RA1) [12] and this search (Rivet). The CMS-SUS-16-038 analysed samples correspond to an integrated luminosity of 35.9 fb^{-1} at a centre-of-mass energy of 13 TeV.

It can be concluded from above that our reconstruction is compatible with the CMS α_T analysis and our implementation can reproduce CMS official results with sufficient accuracy.

5.2.2 Kinematic distributions

n_{jet}, n_b, H_T, H_T^{miss} distributions are shown in Fig. 5.2 and 5.3 as a comparison with Ref. [11]. The variables' distributions for Ref. [12] are not available.

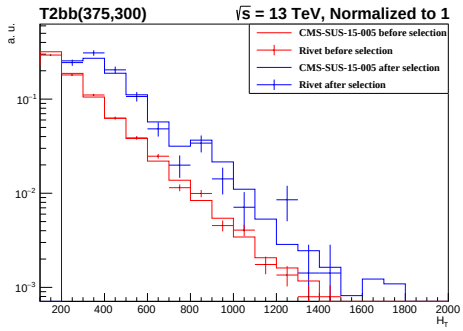

(a) H_T

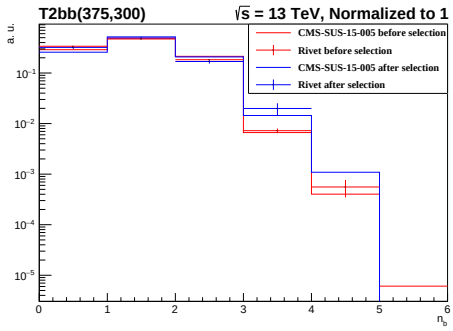

(b) n_b

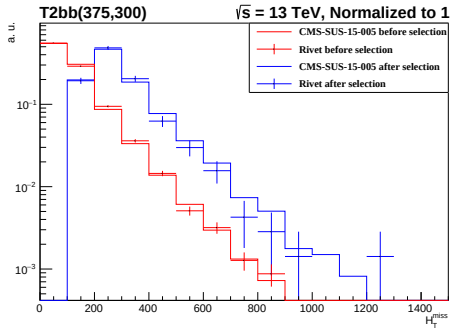

(c) H_T^{miss}

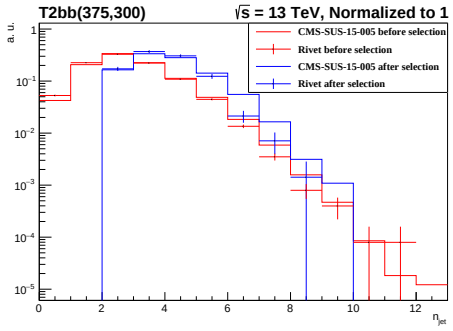

(d) n_{jet}

Figure 5.2: Comparison of distributions for (a) H_T, (b) n_b, (c) H_T^{miss}, and (d) n_{jet} between Ref. [11] and this analysis for SUSY T2bb(375,300). Before and after selection distributions for (a) H_T, (b) n_b, (c) H_T^{miss}, and (d) n_{jet} are all considered. Event selection includes $H_T > 200$ GeV, $H_T^{miss} > 130$ GeV and $n_{jet} > 2$.

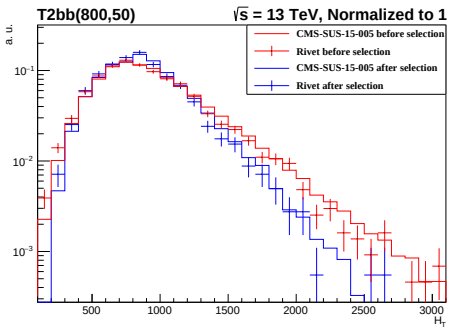

(a) H_T

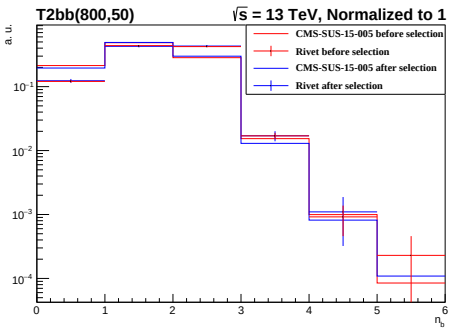

(b) n_b

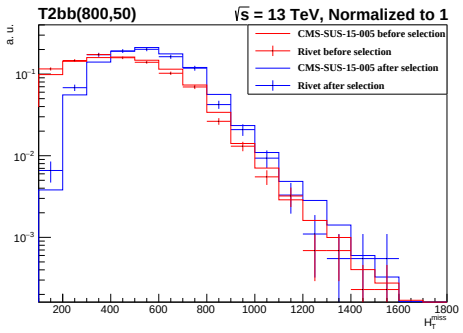

(c) H_T^{miss}

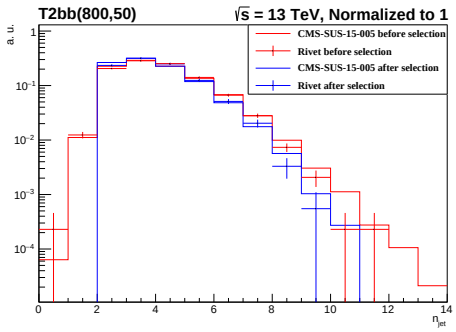

(d) n_{jet}

Figure 5.3: Comparison of distributions for (a) H_T, (b) n_b, (c) H_T^{miss}, and (d) n_{jet} between Ref. [11] and this analysis for SUSY T2bb(800,50). Before and after selection distributions for (a) H_T, (b) n_b, (c) H_T^{miss}, and (d) n_{jet} are all considered. Event selection includes $H_T > 200$ GeV, $H_T^{miss} > 130$ GeV and $n_{jet} > 2$.

It can be concluded from above that our reconstruction is compatible with the CMS α_T analysis within our statistical uncertainties and our implementation can reproduce CMS official results with sufficient accuracy.

5.3 Results

5.3.1 Expected signal yields

The dataset in Ref. [12] is binned in 224 bins as a result of binning in n_{jet}, n_b, H_T, and H_T^{miss}. We identify the most sensitive bins for our analysis using the Asimov Test [62]. The Asimov Test is given by

$$[2((s+b)\ln[\frac{(s+b)(b+\sigma_b^2)}{b^2+(s+b)\sigma_b^2}] - \frac{b^2}{\sigma_b^2}\ln[1+\frac{\sigma_b^2 s}{b(b+\sigma_b^2)}])]^{1/2}, \tag{5.3}$$

where s is the expected number of events from signal, b is the expected number of events from background and σ_b is the background uncertainty. The Asimov Test is a significance calculation taking small statistics and background uncertainties into account [62].

Asimov Test benchmark points are found by assuming the results in Fig. 4.6 to be a reference of the α_T limit behaviour. Based on Fig. 4.6 (b), two points in the exclusion region, (m_s, $m_{Z'}$, m_{DM}) = (70, 2000, 200), (70, 2520, 318), and one point in the boundary region, (m_s, $m_{Z'}$, m_{DM}) = (70, 3175, 318), have been chosen. Additionally, two points to probe the other dark Higgs masses have been chosen:

$(m_s,\ m_{Z'},\ m_{\mathrm{DM}}) = (50,\ 3175,\ 318)$, $(90,\ 3175,\ 318)$. In summary, five benchmark points from signal samples with the DM relic abundance constraint are chosen as signal inputs in Asimov Test: $(m_s,\ m_{Z'},\ m_{\mathrm{DM}}) = (70,\ 2000,\ 200)$, $(70,\ 2520,\ 318)$, $(70,\ 3175,\ 318)$, $(50,\ 3175,\ 318)$, $(90,\ 3175,\ 318)$. We obtain our background numbers and uncertainties from Ref. [12].

After applying Asimov Test, we selected 17 sensitive bins for this dark Higgs search by looking for the best test scores. Table 5.6 shows the 17 sensitive bins we selected.

N_{jet}	N_{bjet}	H_T(low)	H_T(high)	H_T^{miss}(low)	H_T^{miss}(high)	bkg	bkg_{err}	$data$	(70, 2000, 200)	(70, 2520, 318)	(70, 3175, 318)	(50, 3175, 318)	(90, 3175, 318)
2	0	1200	inf	900	inf	20.9	9.39	19	3.89	1.51	2.01	1.98	1.88
2	1	600	900	600	inf	27.1	8.64	31	42.43	16.59	8.04	8.51	7.33
2	1	900	1200	600	900	7.4	2.43	12	15.33	7.58	5.02	4.82	4.11
2	1	900	1200	900	inf	3.2	1.47	6	13.13	8.22	5.98	6.83	6.46
2	1	1200	inf	600	900	2.1	0.70	1	3.26	0.98	0.49	0.77	0.54
2	1	1200	inf	900	inf	2	0.89	4	6.62	4.19	4.19	4.56	4.65
2	2	600	inf	600	inf	2.3	0.76	2	2.31	0.98	0.83	0.69	1.20
3	1	600	900	600	inf	32.7	8.04	42	25.42	7.73	3.99	3.72	4.29
3	1	900	1200	600	900	15.4	3.74	10	14.18	5.84	3.20	3.58	3.26
3	1	900	1200	900	inf	4.4	1.58	6	7.35	4.00	2.36	2.40	2.15
3	1	1200	inf	900	inf	3.5	1.27	4	5.88	3.85	3.10	2.63	2.90
3	2	1200	inf	900	inf	0.3	0.11	0	0.63	0.30	0.28	0.20	0.24
4	1	600	900	600	inf	17.2	4.07	19	8.93	3.32	1.09	1.37	1.35
4	1	900	1200	600	900	12.3	2.98	11	8.51	3.66	1.36	1.71	1.35
4	1	900	1200	900	inf	1.8	0.74	1	1.68	1.17	0.79	0.84	0.69
4	1	1200	inf	900	inf	2.9	1.09	4	3.47	2.19	1.55	1.48	1.22
5	1	1200	inf	900	inf	1.6	0.67	2	1.89	1.09	0.51	0.43	0.47

Table 5.6: The CMS-SUS-16-038 α_T analysis (RA1) dataset [12] and 5 'Higgs Portal DM' model benchmarks' final yield numbers after all selections in 17 chosen most sensitive bins. The 5 benchmarks are shown as (m_s, $m_{Z'}$, m_{DM}).

5.3.2 Exclusion limits

The upper limits at 95% confidence level (CL) [32, 33] are calculated based on the ratio of the signal cross-section to the predicted cross-section, σ/σ_{th}, with an integrated luminosity of 35.9 fb^{-1}. The results are drawn in the $m_{Z'} - m_{\mathrm{DM}}$ plane and regions where σ/σ_{th} ratio is less than one are regarded as excluded regions. 95% CL means that if the signal were to be there, there is only a 5% (100% - 95%) chance we would miss it.

We use **HiggsCombineTool** [52] from **CMSSW_8_1_0** [53] to calculate the exclusion upper limits. More details about this tool can be found in Section 4.3.4. We apply 2016 CMS recorded data, estimated SM background and background statistic uncertainties for each sensitive bin from Ref. [12] into our analysis. We use 8% as our SM background systematic uncertainties as motivated from Ref. [11, 12]. The asymptotic approximation [34] is used in computing exclusion limits. Finally, the upper limits are drawn through the linear interpolation [58] because our signal samples are discrete.

In this section, signal events with two types of coupling scenarios are both considered under m_s ranging from 50 GeV to 90 GeV. The 95% CL upper limits for fixed m_{DM} will be given as examples. Here, we choose $m_s = 70$ GeV, $g_x < (4\pi)^{1/2}$ and $g_q = 0.25$ as an example. For the rest of signal samples, their 1-D projections for fixed m_{DM} can be found in Appendix B.

Signal samples with coupling scenario same as the LHC recommendation: Figure 5.4 shows the 95% CL upper limit for $m_s = 50$ GeV corresponding to an integrated luminosity of 35.9 fb^{-1}. The solid red line is the expected upper limit and one (two) standard deviations have been drawn using dashed red (purple) lines resulting from experimental uncertainties. All the regions below the expected upper limits are excluded.

Figure 5.5 (a) and (b) show the 95% CL upper limits for $m_s = 70$ and 90 GeV with $m_{\mathrm{DM}} = 100$ GeV, respectively. It can be seen that no parameter space can be excluded for $m_s = 70$ GeV nor 90 GeV because the expected upper limit on the cross-section is always higher than the theoretical cross-section.

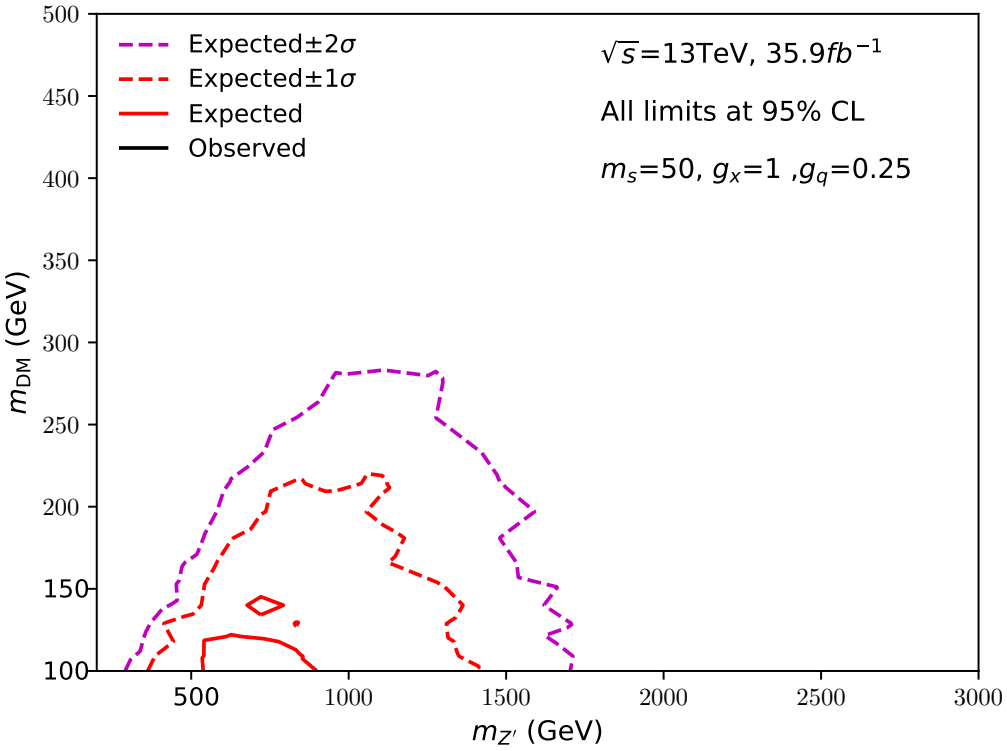

Figure 5.4: The expected exclusion region of the α_T analysis at 95% CL with an integrated luminosity of 35.9 fb^{-1} at a centre-of-mass energy of 13 TeV. The inputs all correspond to $m_s = 50$ GeV. The couplings are set according to LHC recommendations [37]. The solid red line shows the expected upper limit and one (two) standard deviations arising from experimental uncertainties have been drawn using dashed red (purple) lines.

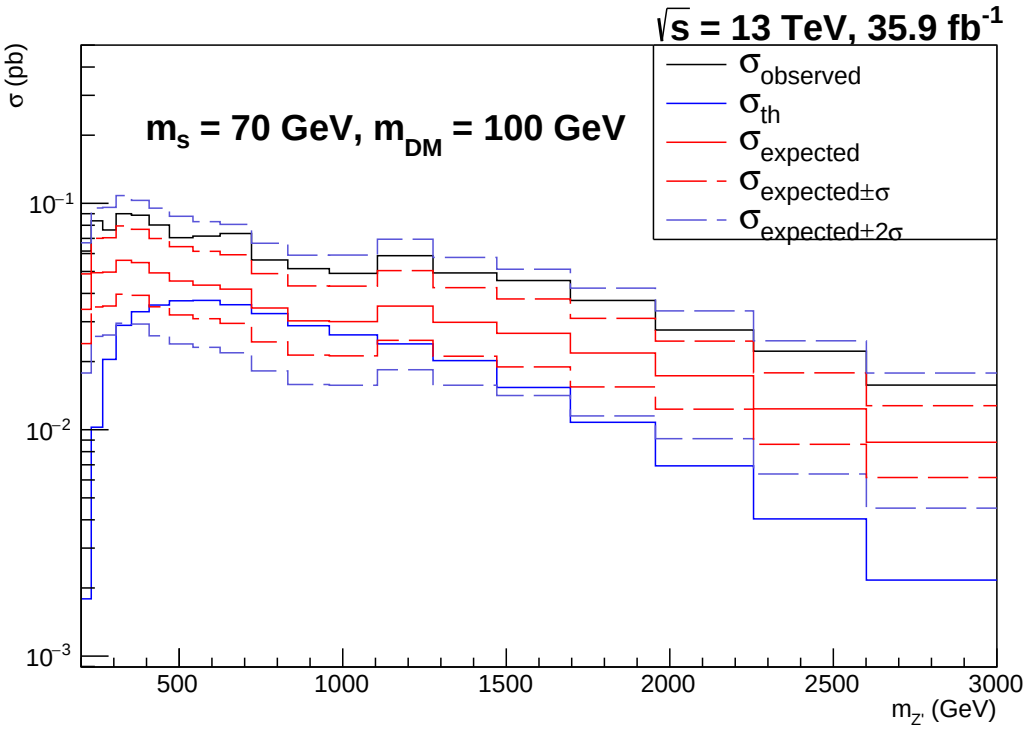

(a) $m_s = 70$ GeV, $g_x = 1$ and $g_q = 0.25$

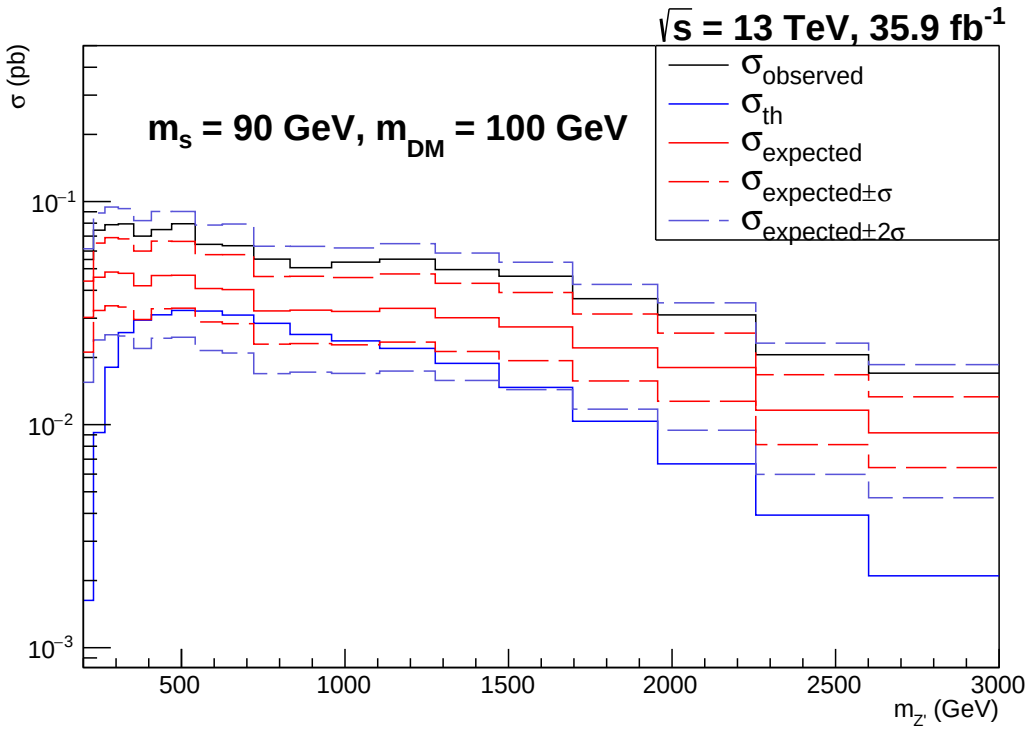

(b) $m_s = 90$ GeV, $g_x = 1$ and $g_q = 0.25$

Figure 5.5: Expected and observed 95% CL limits for $m_s = 70$ and 90 GeV with $m_{\mathrm{DM}} = 100$ GeV, respectively. The couplings are set according to LHC recommendations [37]. The theoretical cross-section is shown as the blue solid line.

Signal events with coupling scenario considering the DM relic abundance constraint from the universe: Figure 5.6 (a), (b) and (c) respectively show the upper limits for $m_s = 50$, 70 and 90 GeV at 95% CL with an integrated luminosity of 35.9 fb^{-1}. The solid black line is the observed upper limit. The solid red line is the expected upper limit and one (two) standard deviations have been drawn using dashed red (purple) lines from experimental uncertainties. All the regions below the observed upper limit is excluded. The dashed blue line indicates the region with $g_x = (4\pi)^{1/2}$ beyond which the theory becomes non-perturbative.

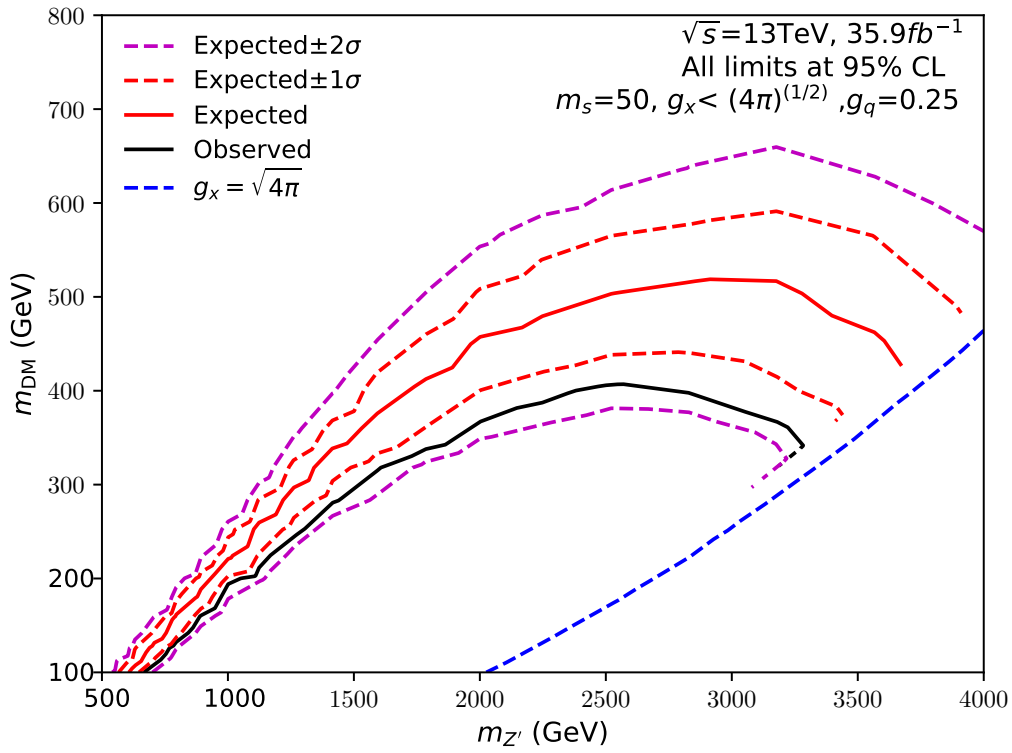

(a) $m_s = 50$ GeV, $g_x < (4\pi)^{1/2}$ and $g_q = 0.25$

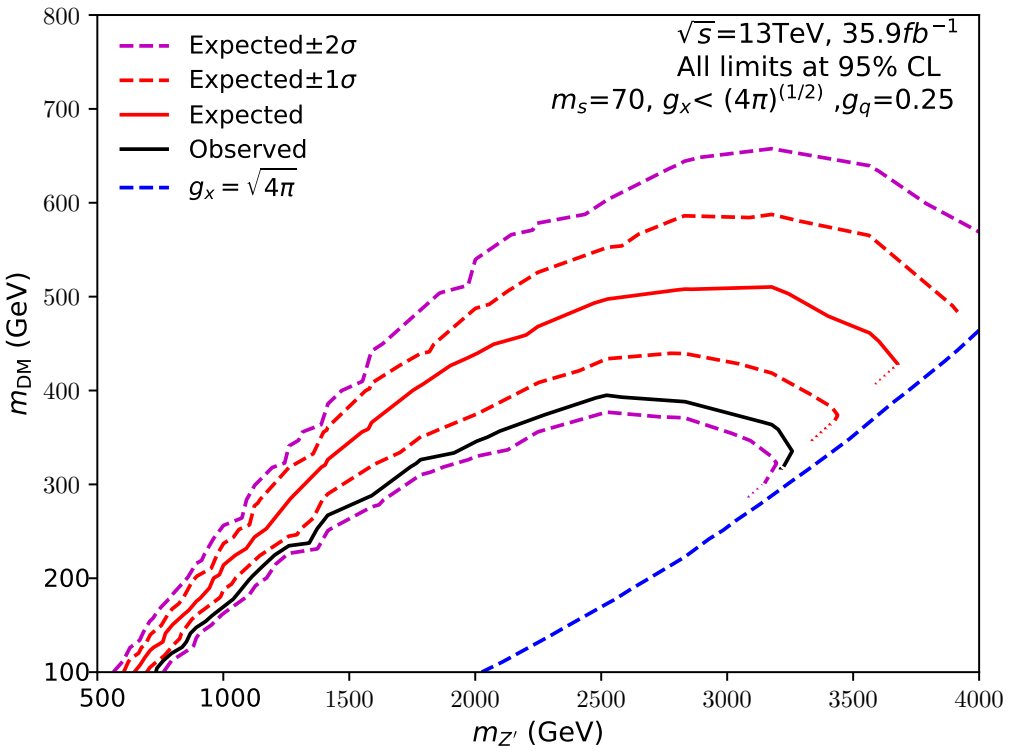

(b) $m_s = 70$ GeV, $g_x < (4\pi)^{1/2}$ and $g_q = 0.25$

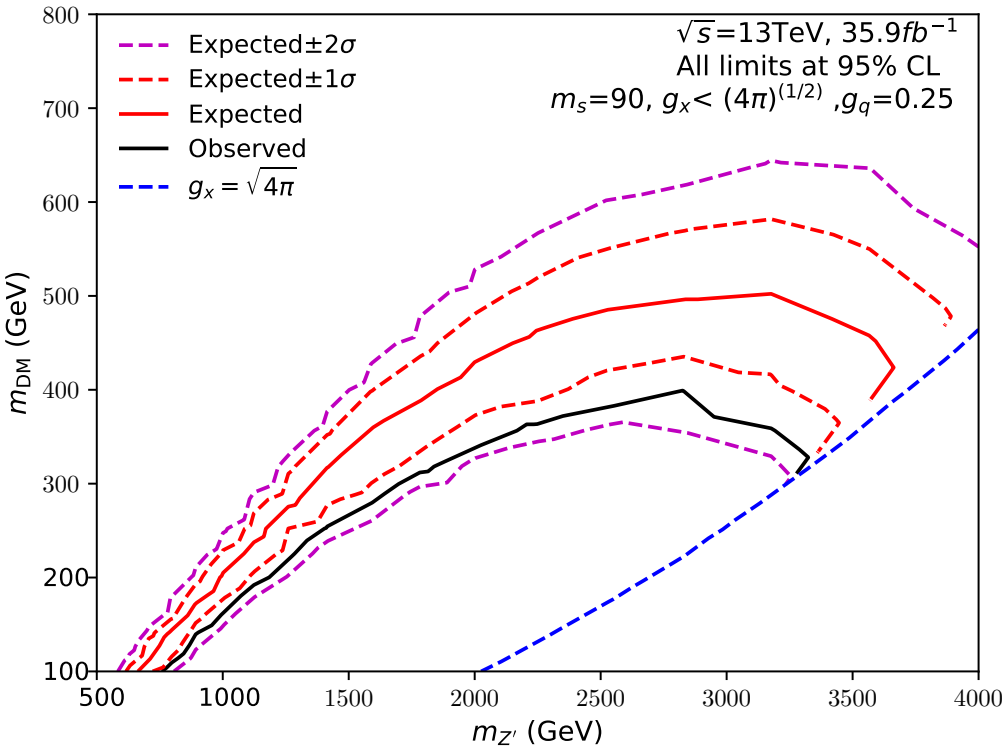

(c) $m_s = 90$ GeV, $g_x < (4\pi)^{1/2}$ and $g_q = 0.25$

Figure 5.6: The expected exclusion region of the α_T analysis at 95% CL with an integrated luminosity of 35.9 fb^{-1} at a centre-of-mass energy of 13 TeV. The inputs correspond to $m_s = 50$, 70 and 90 GeV. The coupling g_x is chosen to fulfil the relic density constraint [2]. The solid black line shows the observed upper limits. The solid red line shows the expected upper limits and one (two) standard deviations from experimental uncertainties have been drawn using dashed red (purple) lines. All the regions below the observed upper limits are excluded. The dashed blue line indicates the region where $g_x = (4\pi)^{1/2}$.

Exclusion limits at fixed $\mathbf{m_{DM}} = 100$ GeV and 449 GeV for $\mathbf{m_s} = 70$ GeV, $\mathbf{g_x} < (4\pi)^{1/2}$ and $\mathbf{g_q} = 0.25$: To help understand the behaviour of the 2-D limit plots, we look at the 95% CL limit for selected fixed DM masses as a function of $m_{Z'}$. We consider signals with $m_s = 70$ GeV, $g_x < (4\pi)^{1/2}$ and $g_q = 0.25$ as an example. Their 1-D projections for fixed $m_{\rm DM}$ are shown in Fig. 5.7.

For the rest of signal samples, their 1-D projections for fixed $m_{\rm DM}$ can be found in Appendix B.

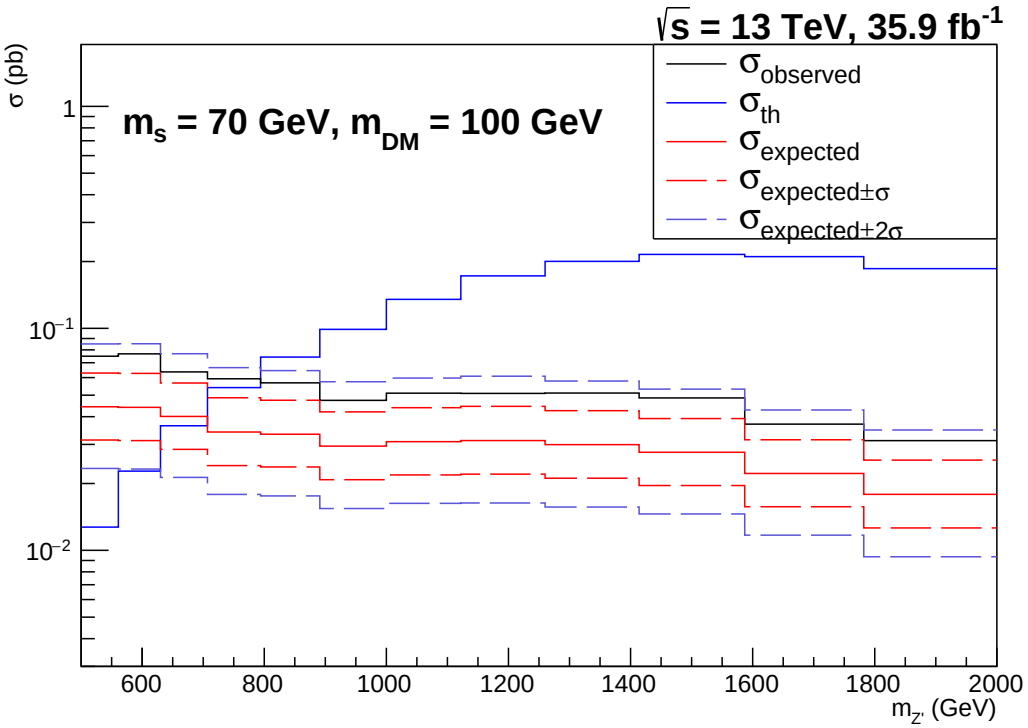

(a) $m_s = 70$ GeV, $m_{\mathrm{DM}} = 100$ GeV, $g_x < (4\pi)^{1/2}$ and $g_q = 0.25$

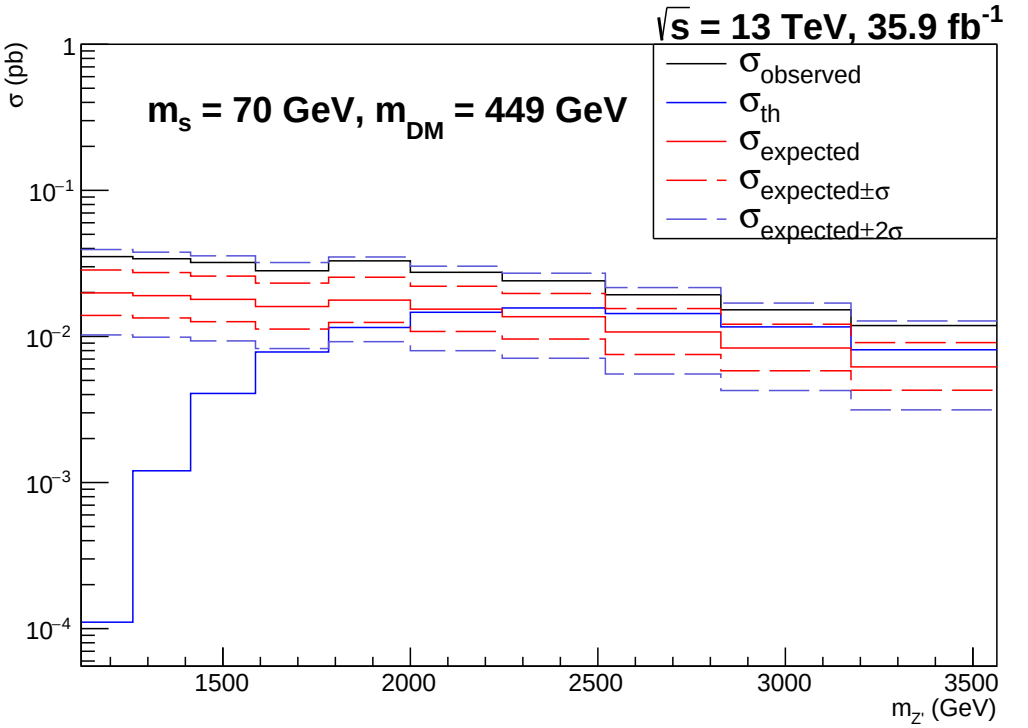

(b) $m_s = 70$ GeV, $m_{\mathrm{DM}} = 449$ GeV, $g_x < (4\pi)^{1/2}$ and $g_q = 0.25$

Figure 5.7: Expected and observed 95% CL limits for $m_s = 70$ GeV with $m_{\mathrm{DM}} = 100$ and 449 GeV. The couplings are set to fulfil the relic density constraint [2]. The theoretical cross-section is shown as the blue solid line.

6 Discussion

6.1 Large-radius jet analysis comparison

Both Ref. [1] and our large-radius jet recast are trying to reproduce the ATLAS simulation [9]. Both analyses are introducing rescaling factors in order to be compatible with ATLAS background estimation [9]. From Table 4.1, it can be concluded that our analysis is compatible with Ref. [1] and the largest rescaling factor difference between our simulation and that of Ref. [1] is less than 0.8. Our simulation is slightly closer to ATLAS background estimation compared to Ref. [1].

Figure 4.4 shows the reconstructed large-radius jet mass distribution for signal processes with different m_s and different $m_{Z'}$. It can be concluded that the signal processes always peak as expected at around the mass of the dark Higgs when reconstructing the mass of the large-radius jet. Ref. [1] and Ref. [9] also obtain the same result, which can be treated as a confirmation of our recast.

We choose different mass windows for different m_s signals in the distributions of large-radius jet mass in order to maximise the expected significance. And by looking at the exclusion limits that we draw for different signal samples, some conclusions can be drawn.

Figure 4.5 (a), (b) and (c) are the expected exclusion limits for $m_s = 50$, 70 and 90 GeV for signal samples with coupling scenario set to the LHC recommendation [37]. It can be seen that for both $m_s = 50$ and 70 GeV, the expected upper limits peak at around $m_{\mathrm{DM}} = 300$ GeV while the expected upper limits peak at around $m_{\mathrm{DM}} = 270$ GeV for $m_s = 90$ GeV. This is because there are more SM background events at around 90 GeV from diboson production. For $m_s = 50$, 70 and 90 GeV, $m_{Z'}$ up to 1800, 2000 and 1800 GeV are respectively excluded.

Figure 4.6 (a), (b) and (c) are the exclusion limits for $m_s = 50$, 70 and 90 GeV for signal samples fulfilling the DM relic abundance constraint. For $m_s = 50$, 70 and 90 GeV, $m_{Z'}$ up to 3300, 3450 and 3500 GeV are respectively excluded. By comparing with Ref. [1], it can be seen that our expected exclusion limits are comparable with Ref. [1].

6.2 α_T analysis comparison

We implemented the CMS α_T analysis and validated it with the help of SUSY T2bb samples by comparing the selection efficiencies at different stages of the event selection. Tables 5.2 and 5.3 show the comparison between our reinterpretation and CMS simulation from Ref. [11]. It can be seen that the maximum difference for T2bb(375, 300) between our reinterpretation and CMS simulation is 9% and the maximum difference for T2bb(800, 50) between our reinterpretation and CMS simulation is 5%. The distributions of the four key variables ($n_{jet}, n_b, H_T, H_T^{miss}$) are shown in Fig. 5.2 and Fig. 5.3 for comparison. As Ref. [12] appeared while working on this analysis, we updated our numbers and reinterpretations (see Table 5.4 and Table 5.5). It can be seen that the maximum difference for T2bb(1000, 100) between our reinterpretation and CMS simulation is 11% and the maximum difference for T2bb(550, 450) between our reinterpretation and CMS simulation is 14%. It can be concluded that our reconstruction is compatible with the CMS α_T analysis and our implementation can reproduce CMS official results with sufficient accuracy.

We use the Asimov Test [62] to find the sensitive bins for our dark Higgs search, taking small statistics and background uncertainties into account [62]. In the end, 17 bins are selected as sensitive bins and Table 5.6 shows those bins in detail. It can be seen that some bins are more sensitive to $m_s = 70$ GeV signals while other bins are more sensitive to $m_s = 50$ and 90 GeV signals. Therefore, our sensitive bins can cover a wide range of m_s distribution in 'Higgs Portal DM' model.

The exclusion limits are drawn in different signal coupling scenarios with different m_s distributions.

Figure 5.4 presents the exclusion limits for $m_s = 50$ GeV and with a coupling scenario following the LHC recommendation [37]. The expected exclusion limit is relatively weak. 95% CL exclusion plots for fixed m_{DM} and $m_s = 50$ GeV are shown in Appendix B. Figure 5.5 (a) and (b) show the 95% CL expected upper limits for $m_s = 70$ and 90 GeV with $m_{\mathrm{DM}} = 100$ GeV. It can be concluded that no significant expected upper limits can be drawn for $m_s = 70$ GeV nor 90 GeV because the expected upper limit on the cross-section is always higher than the theoretical cross-section.

Figure 5.6 (a), (b) and (c) are the 95 % exclusion limits for $m_s = 50$, 70 and 90 GeV for signal samples fulfilling the DM relic abundance constraint. For $m_s = 50$, 70

and 90 GeV, $m_{Z'}$ up to 3600, 3700 and 3700 GeV are excluded.

Figure 5.4 and 4.5 (a) show that CMS α_T analysis provides a worse expected limit than the large-radius jet one in the LHC-recommended coupling scenario [37]. The large-radius jet analysis considers a single bin containing all the events, while the CMS α_T one combines many bins with lower sensitivity. The Asimov Test shows that less events are produced in the LHC-recommended coupling scenario than in the one using the relic density constraint. This implies that in the former scenario, the CMS α_T analysis will have a large number of bins with insufficient statistics that can not be combined to give a strong exclusion limit.

7 Conclusion

In this thesis we have presented two complementary methods to search for dark matter (DM) at high-energy colliders under a 'Higgs Portal Dark Matter' model.

The 'Higgs Portal Dark Matter' model proposes a dark Higgs boson that can generate masses for the dark sector particles. This model enables to relax constraints from DM relic abundance by opening up a new type of annihilation channels like $\chi\chi \to s \to q\bar{q}$, $\chi\chi \to sZ' \to q\bar{q}$ and $\chi\chi \to s \to Z'Z'$. The experimental signature for 'Higgs Portal Dark Matter' model is a large-radius jet from the dark Higgs decay and large missing transverse momentum (MET) from the DM production. Since this thesis focuses on dark Higgs decaying to a pair of b-tagged jets, the experimental signature for our search is one boosted double b-tagged jet from the dark Higgs decay together with large MET from escaping DM particles.

Two different searching methods have been investigated in this thesis: the large-radius mono-jet search and the more "generic" MET + jets search using the CMS α_T analysis. The former was carried out by the ATLAS experiment, searching for a large-radius jet containing at least two b-tagged sub-jets with large MET. The latter is based on a CMS search, searching for resolved b-jets with specific kinematic variables and large missing energy.

The recast of the large-radius search shows that signals with couplings according to the LHC recommendation can obtain significant exclusion limits. When the mass of the dark Higgs (m_s) is 50, 70 and 90 GeV, the mass of the $Z^{'}$ ($m_{Z'}$) up to 1800, 2000 and 1800 GeV are respectively excluded. The recast of the large-radius search shows that signals with couplings set to fulfil the DM relic abundance constraint can obtain significant exclusion limits. For $m_s = 50$, 70 and 90 GeV, $m_{Z'}$ up to 3300, 3450 and 3500 GeV are respectively excluded.

The reinterpretation of the CMS α_T search shows that signals with couplings according to the LHC recommendation cannot obtain significant exclusion limits. However, the reinterpretation of the α_T search shows that signals with couplings set to fulfil the DM relic abundance constraint can obtain significant exclusion limits. For $m_s = 50$, 70 and 90 GeV, $m_{Z'}$ up to 3600, 3700 and 3700 GeV are respectively excluded.

The two search methods are complementary in this 'Higgs Portal Dark Matter' model and they both probe significant regions of parameter space of the model.

The CMS α_T search uses four variables to identify regions of phase-space that are sensitive to a large number of signals, resulting in many signal bins. The large-radius jet search only has one sensitive bin with variable mass windows to identify sensitive regions.

The presented analysis does not use a dedicated detector reconstruction but only applies a resolution smearing to physics objects in particular jets. A future improvement could be to change this and to generate signal samples with a dedicated detector reconstruction to obtain more accurate results.

The analysis presented in this thesis focuses on the dark Higgs s-channel $b\bar{b}$ decay. Searching for dark Higgs t-channel decay could be the next step.

References

[1] Michael Duerr et al., "Hunting the dark Higgs", 2017.arXiv:1701.08780

[2] Duerr, M., Kahlhoefer, F., Schmidt-Hoberg, K. et al., "How to save the WIMP: global analysis of a dark matter model with two s-channel mediators", J. High Energ. Phys., Volume 042, September 2016.arXiv:1606.07609

[3] Nicole F. Bell, Yi Cai, Rebecca K. Leane, "Impact of Mass Generation for Simplified Dark Matter Models", October 2016.arXiv:1610.03063

[4] T. S. Pettersson and P. Lefevre. "The Large Hadron Collider: conceptual design". Tech. rep. CERN-AC-95-05-LHC, 1995. CMS Collaboration, "The CMS experiment at the CERN LHC", JINST, vol.3, 2008.

[5] A. A. Petrov and W. Shepherd, "Searching for dark matter at LHC with Mono-Higgs production", 2013.arXiv:1311.1511

[6] L. Carpenter, A. DiFranzo, M. Mulhearn, C. Shimmin, S. Tulin, et al., "Impact of Mass Generation for Simplified Dark Matter Models", 2014.arXiv:1312.2592

[7] A. Berlin, T. Lin, and L.-T. Wang, "Mono-Higgs Detection of Dark Matter at the LHC", 2014.arXiv:1402.7074

[8] ATLAS Collaboration, "The ATLAS Experiment at the CERN Large Hadron Collider", J.Inst., Volume 3, August 2008.

[9] ATLAS Collaboration, "Search for dark matter in association with a Higgs boson decaying to b-quarks in pp collisions at $\sqrt{s} = 13$ TeV with the ATLAS detector", Phys. Lett. B, vol. 765, 2016.arXiv:1609.04572

[10] CMS Collaboration, "The CMS experiment at the CERN LHC", JINST, vol.3, 2008.

[11] CMS Collaboration, "A search for new phenomena in pp collisions at $\sqrt{s} =$ 13 TeV in final states with missing transverse momentum and at least one jet using the alphaT variable", Eur. Phys. J., vol. 77, 2017.arXiv:1611.00338 Version one : CMS-SUS-15-005, CERN-EP-2016-246.

[12] CMS Collaboration, "Search for natural and split supersymmetry in proton-proton collisions at $\sqrt{s} = 13$ TeV in final states with jets and missing transverse momentum".arXiv:1802.02110 Version one : CMS-SUS-16-038, CERN-EP-2018-003.

[13] F. Zwicky, "Die Rotverschiebung von extragalaktischen Nebeln", Helv. Phys. Acta, vol. 6, pp. 110–127, 1933.

[14] Roberts M. S & Rots A. H., "Comparison of Rotation Curves of Different Galaxy Type", Astron.Astrophys., vol. 26, pp. 483–485, 1973.

[15] Ostriker, J. P., Peebles, P. J. E. & Yahil, A., "The size and mass of galaxies, and the mass of the universe",Astrophysical Journal, vol. 193, p. L1–L4, 1974.

[16] Einasto, J., Kaasik, A. & Saar, E., "Dynamic evidence on massive coronas of galaxies",Nature, vol. 250, pp. 309–310, 1974.

[17] Rubin, V. C., Thonnard, N. & Ford, W. K., Jr., "Extended rotation curves of high-luminosity spiral galaxies. IV - Systematic dynamical properties, SA through SC",Astrophysical Journal, vol. 225, p. L107-L111, 1978.

[18] Douglas Clowe et al., "A direct empirical proof of the existence of dark matter",Astrophysical Journal, vol. 648, p. L109-L113, 2006.arXiv:astro-ph/0608407

[19] Wikipedia. 2018. Galaxy rotation curve. [ONLINE] Available at: https://en.wikipedia.org/wiki/Galaxy_rotation_curve. [Accessed 19 July 2018].

[20] R. Bernabei et al.[DAMA Collaboration], "First results from DAMA/LIBRA and the combined results with DAMA/NaI",Eur.Phys.J.C, vol. 56, pp. 333–355, 2008.arXiv:0804.2741

[21] SABRE Collaboration, "Dark matter search with the SABRE experiment", July 2018. arXiv:1807.08073

[22] Marco Cirelli, "Indirect Searches for Dark Matter: a status review", 2013.arXiv:1202.1454v5

[23] Jennifer M. Gaskins, "A review of indirect searches for particle dark matter", Contemporary Physics, vol. 57, 2016.arXiv:1604.00014

[24] CMS Collaboration, "Search for new physics in final states with an energetic jet, or a hadronically decaying W or Z boson and transverse momentum imbalance at $\sqrt{s} = 13$ TeV", 2018. CMS-EXO-16-048. arXiv:1712.02345

[25] CMS Collaboration, "Search for dark matter in final states with an energetic jet, or a hadronically decaying W or Z boson using 12.9 fb^{-1} of data at $\sqrt{s} =$ 13 TeV", 2016. CMS-PAS-EXO-16-037.

[26] CMS Collaboration, "Particle-Flow Event Reconstruction in CMS and Performance for Jets, Taus, and MET", 2009. CMS-PAS-PFT-09-001.

[27] CMS Collaboration, "Commissioning of the Particle-flow Event Reconstruction with the first LHC collisions recorded in the CMS detector", 2010. CMS-PAS-PFT-10-001.

[28] Matteo Cacciari, Gavin P. Salam & Gregory Soyez, "The anti-k_t jet clustering algorithm",JHEP 0804:063, 2008.arXiv:0802.1189

[29] Matteo Cacciari & Gavin P.Salam, "Pileup subtraction using jet areas", Phys. Lett. B, vol. 659, pp. 119–126, 2008.arXiv:0707.1378

[30] CMS Collaboration, "Determination of jet energy calibration and transverse momentum resolution in CMS", Journal of Instrumentation, vol. 6, 2011.arXiv:1107.4277

[31] J. Thaler & K. Van Tilburg, "Identifying Boosted Objects with N-subjettiness", JHEP, vol. 03, 2011.arXiv:1011.2268

[32] T. Junk, "Confidence level computation for combining searches with small statistics", Nucl. Instrum. Meth., vol. 434, 1999.arXiv:hep-ex/9902006

[33] A. L. Read, "Presentation of search results: the CLs technique", J. Phys., vol. 28, 2002.

[34] G. Cowan, K. Cranmer, E. Gross, and O. Vitells, "Asymptotic formulae for likelihood-based tests of new physics", Eur. Phys. J., vol. 71, 2011.arXiv:1007.1727

[35] Planck Collaboration, "Planck 2015 results. XIII. Cosmological parameters", Astron. Astrophys., vol. 594, 2016.arXiv:1502.01589

[36] Planck Collaboration, "Planck 2013 results. XVI. Cosmological parameters", Astron. Astrophys., vol. 571, 2014.arXiv:1303.5076

[37] D. Abercrombie et al., "Dark Matter Benchmark Models for Early LHC Run-2 Searches: Report of the ATLAS/CMS Dark Matter Forum", 2015.arXiv:1507.00966.

[38] University of Zurich. 2018. Standard Model. [ONLINE] Available at: https://www.physik.uzh.ch/en/researcharea/lhcb/outreach/Standard-Model.html. [Accessed 2 March 2018].

[39] Thomson, M., 2013. Modern Particle Physics. 1st ed. United States of America, New York: Cambridge University Press.

[40] S. Weinberg, "A model of Leptons", Phy. Rev. Lett., 20th Nov., 1967.Phy_Rev_Lett_19_1264_67

[41] N. F. Bell, Y. Cai, and R. K. Leane, "Dark Forces in the Sky: Signals from Z' and the Dark Higgs", JCAP, 2016.1605.09382

[42] F. Kahlhoefer, K. Schmidt-Hoberg, T. Schwetz, and S. Vogl, "Implications of unitarity and gauge invariance for simplified dark matter models", JHEP, volume 16, 2016.1510.02110

[43] N. F. Bell, Y. Cai, and R. K. Leane, "Impact of Mass Generation for Simplified Dark Matter Models", JCAP, 2016.1610.03063

[44] ATLAS Collaboration, "Expected Performance of Boosted Higgs ($\rightarrow b\bar{b}$) Boson Identification with the ATLAS Detector at $\sqrt{s} = 13$ TeV", ATL-PHYS-PUB-2015-035, August 2015.

[45] ATLAS Collaboration, "Performance of Missing Transverse Momentum Reconstruction in Proton-Proton Collisions at $\sqrt{s} = 7$ TeV with ATLAS", Eur. Phys. J. C, Volume 72, 2012.arXiv:1108.5602

[46] G. Belanger, F. Boudjema, A. Pukhov, A. Semenov, "micrOMEGAs4.1: two dark matter candidates", Computer Physics Communications, Volume 192, pp. 322–329, July 2015.arXiv:1407.6129.

[47] J. Alwall, M. Herquet, F. Maltoni, O. Mattelaer & T. Stelzer, "MadGraph 5 : Going Beyond", JHEP, 2011.arXiv:1106.0522

[48] T. Sjostrand, S. Ask, J. R. Christiansen, R. Corke, N. Desai, et al., "An Introduction to PYTHIA 8.2", Comput. Phys. Commun., vol. 191, pp. 159–177, 2015.arXiv:1410.3012

[49] A. Buckley, J. Butterworth, L. Lonnblad, D. Grellscheid, H. Hoeth, et al., "Rivet user manual", , Comput. Phys. Commun., vol. 184, pp. 2803–2819, 2013.arXiv:1003.0694

[50] J. Abdallah etc., "Simplified Models for Dark Matter Searches at the LHC", 2016.1506.03116

[51] ATLAS Collaboration, "Search for dark matter in events with a hadronically decaying vector boson and missing transverse momentum in pp collisions at $\sqrt{s} = 13$ TeV with the ATLAS detector", CERN-EP-2018-083, 2018.arXiv:1807.11471

[52] CMS Collaboration. 2008. Combine. [ONLINE] Available at: https://cms-hcomb.gitbooks.io/combine/content. [Accessed 23 August 2018].

[53] CMS Collaboration. 2016. CMSSW_8_1_X. [ONLINE] Available at: https://github.com/cms-sw/cmssw/tree/CMSSW_8_1_X. [Accessed 22 December 2016].

[54] Matteo Cacciari, Gavin P. Salam & Gregory Soyez, "FastJet user manual",Eur.Phys.J.C 72: 1896, 2012.arXiv:1111.6097

[55] Matteo Cacciari, Gavin P. Salam & Gregory Soyez, "The Catchment Area of Jets",JHEP 0804:005, 2008.arXiv:0802.1188

[56] David Krohn, Jesse Thaler & Lian-Tao Wang, "Jet Trimming",JHEP 1002:084, 2010.arXiv:0912.1342

[57] CMS Collaboration. 2008. Documentation of the RooStats -based statistics tools for Higgs PAG–A_simple_counting_experiment–Computing limits with the asymptotic CL_S method. [ONLINE] Available at: https://twiki.cern.ch/twiki/bin/viewauth/CMS/SWGuideHiggsAnalysis CombinedLimit_A_simple_counting_experiment. [Accessed 23 August 2018].

[58] SciPy. 2008. Interpolation (scipy.interpolate). [ONLINE] Available at: https://docs.scipy.org/doc/scipy/reference/tutorial/interpolate.html. [Accessed 5 May 2018].

[59] ATLAS Collaboration, "Boosted Higgs ($\to b\bar{b}$) Boson Identification with the ATLAS Detector $\sqrt{s} = 13$ TeV", 2016. ATLAS-CONF-2016-039.

[60] ATLAS Collaboration, "Optimisation of the ATLAS b-tagging performance for the 2016 LHC Run", 2016. ATL-PHYS-PUB-2016-012.

[61] ATLAS Collaboration, "Search for Dark Matter Produced in Association with a Higgs Boson Decaying to $b\bar{b}$ Using 36 fb^{-1} of pp Collisions at $\sqrt{s} = 13$ TeV with the ATLAS Detector", Phys. Rev. Lett., Volume 119, November 2017. arXiv:1707.01302v3

[62] G. Cowan, "Discovery Sensitivity for a Counting Experiment with Background Uncertainty", Tech. Rep., Royal Holloway, London, 2012. [ONLINE] Available at: http://www.pp.rhul.ac.uk/ cowan/stat/medsig/medsigNote.pdf

[63] CMS Collaboration, "Electron reconstruction and identification at $\sqrt{s} = 7$ TeV", CMS-PAS-EGM-10-004, 2010.

[64] CMS Collaboration, "Performance of CMS muon reconstruction in pp collision events at $\sqrt{s} = 7$ TeV", JINST, vol. 7, 2012.arXiv:1206.4071

[65] CMS Collaboration, "Isolated Photon Reconstruction and Identification at $\sqrt{s} = 7$ TeV", CMS-PAS-EGM-10-006, 2010.

[66] CMS Collaboration, "Search for Supersymmetry in pp Collisions at 7 TeV in Events with Jets and Missing Transverse Energy", Phys. Lett. B, vol. 698, pp. 196–218, 2011.arXiv:1101.1628

[67] L. Randall & D. Tucker-Smith, "Dijet Searches for Supersymmetry at the Large Hadron Collider", Phys. Rev. Lett., vol. 101, 2008.arXiv:0806.1049

[68] CMS Collaboration, "Search for Supersymmetry at the LHC in Events with Jets and Missing Transverse Energy", Phys. Rev. Lett., vol. 107, 2011.arXiv:1109.2352

[69] CMS Collaboration, "Search for supersymmetry in final states with missing transverse energy and 0, 1, 2, or at least 3 b-quark jets in 7 TeV pp collisions using the variable alphaT", JHEP, vol. 01, 2013.arXiv:1210.8115

[70] CMS Collaboration, "An inclusive search for new phenomena in final states with one or more jets and missing transverse momentum at 13 TeV with the AlphaT variable", CMS PAS SUS-16-016, 2016.

Appendices

A Exclusion limits at fixed m_{DM} for different signal samples according to the large-radius monojet search

Figure A.1 to Figure A.4 are from signals with g_x =1 and $g_q = 0.25$. Figure A.5 to Figure A.10 are from signals with $g_x < (4\pi)^{1/2}$ and $g_q = 0.25$.

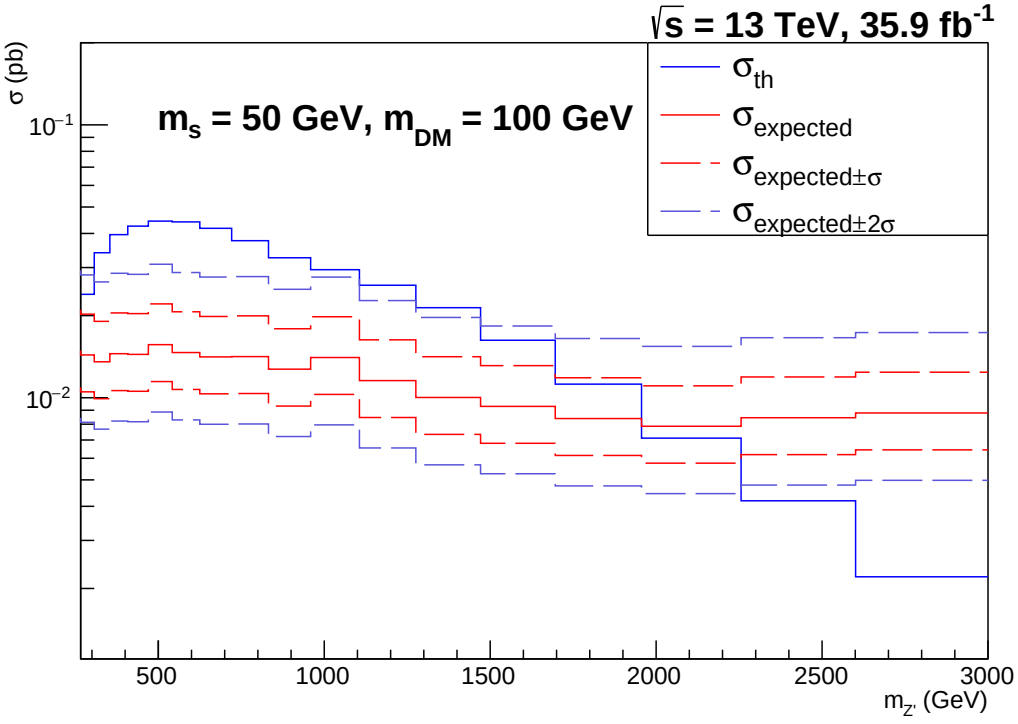

Figure A.1: Expected 95% CL limits for $m_s = 50$ GeV, $g_x = 1.0$ and $g_q = 0.25$ with $m_{\mathrm{DM}} = 100$ GeV.

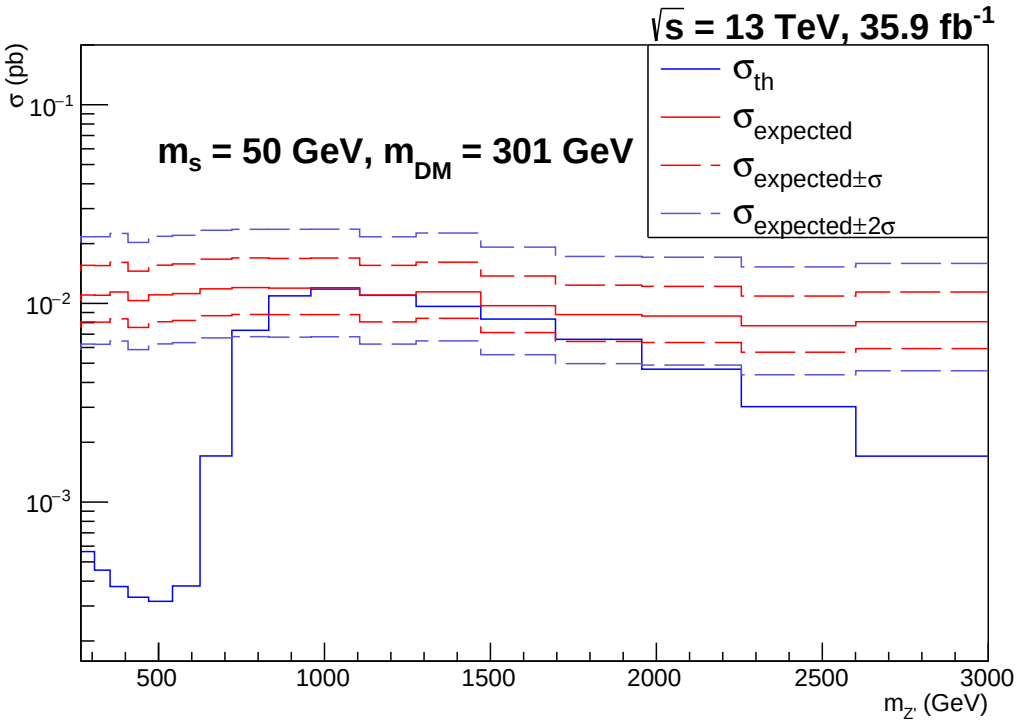

Figure A.2: Expected 95% CL limits for $m_s = 50$ GeV, $g_x = 1.0$ and $g_q = 0.25$ with $m_{\mathrm{DM}} = 301$ GeV.

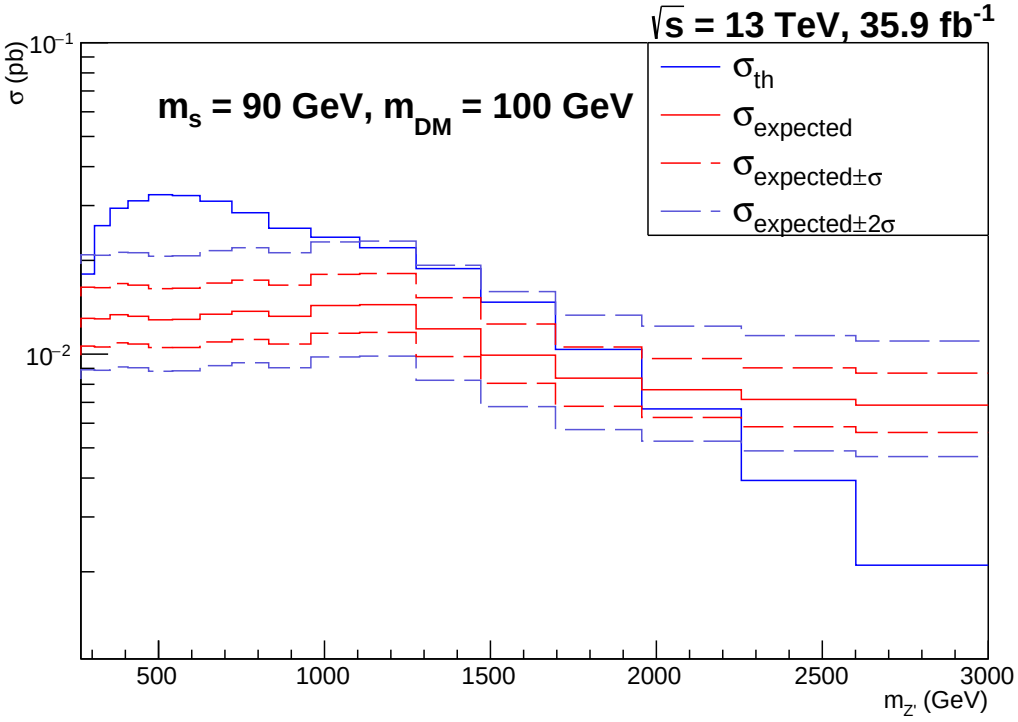

Figure A.3: Expected 95% CL limits for $m_s = 90$ GeV, $g_x = 1.0$ and $g_q = 0.25$ with $m_{\mathrm{DM}} = 100$ GeV.

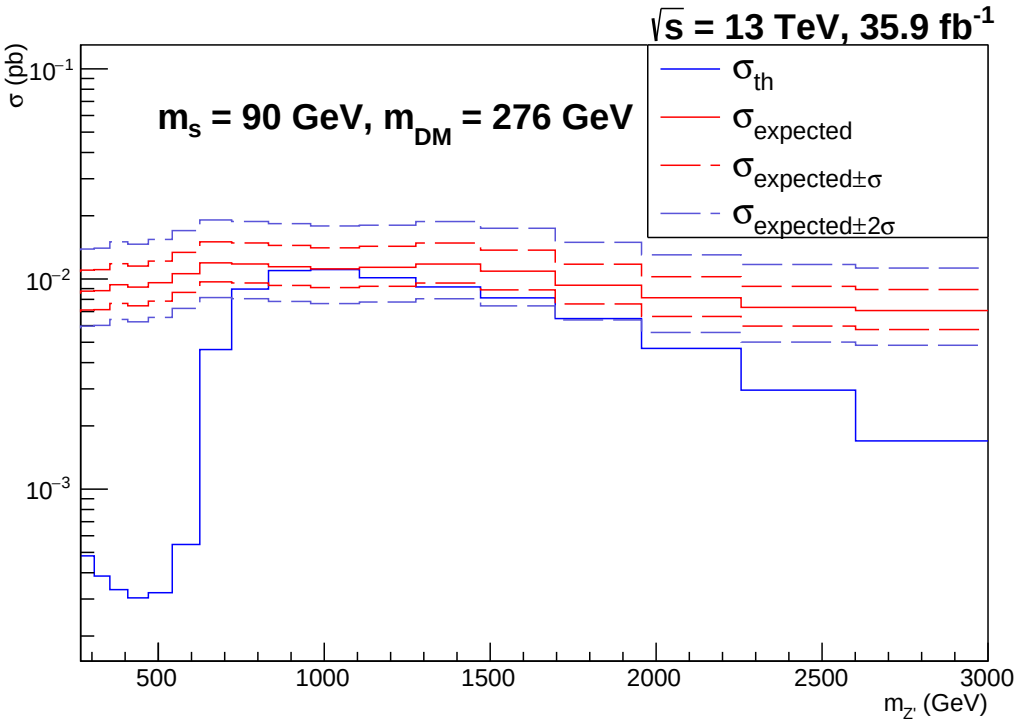

Figure A.4: Expected 95% CL limits for $m_s = 90$ GeV, $g_x = 1.0$ and $g_q = 0.25$ with $m_{\mathrm{DM}} = 276$ GeV.

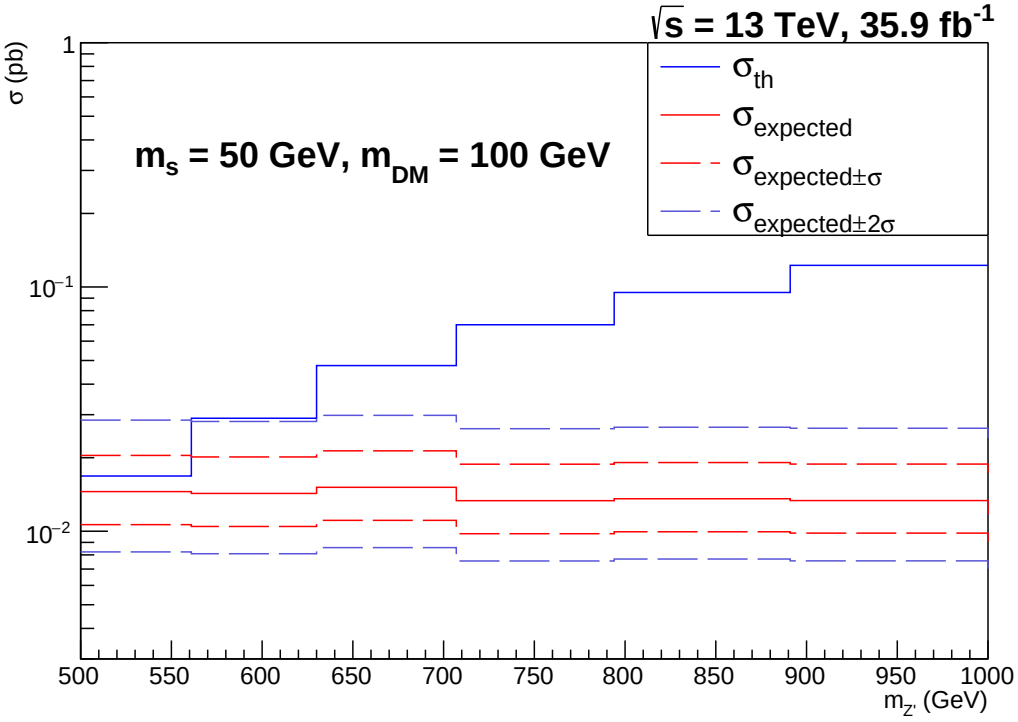

Figure A.5: Expected 95% CL limits for $m_s = 50$ GeV, $g_x < (4\pi)^{1/2}$ and $g_q = 0.25$ with $m_{\mathrm{DM}} = 100$ GeV.

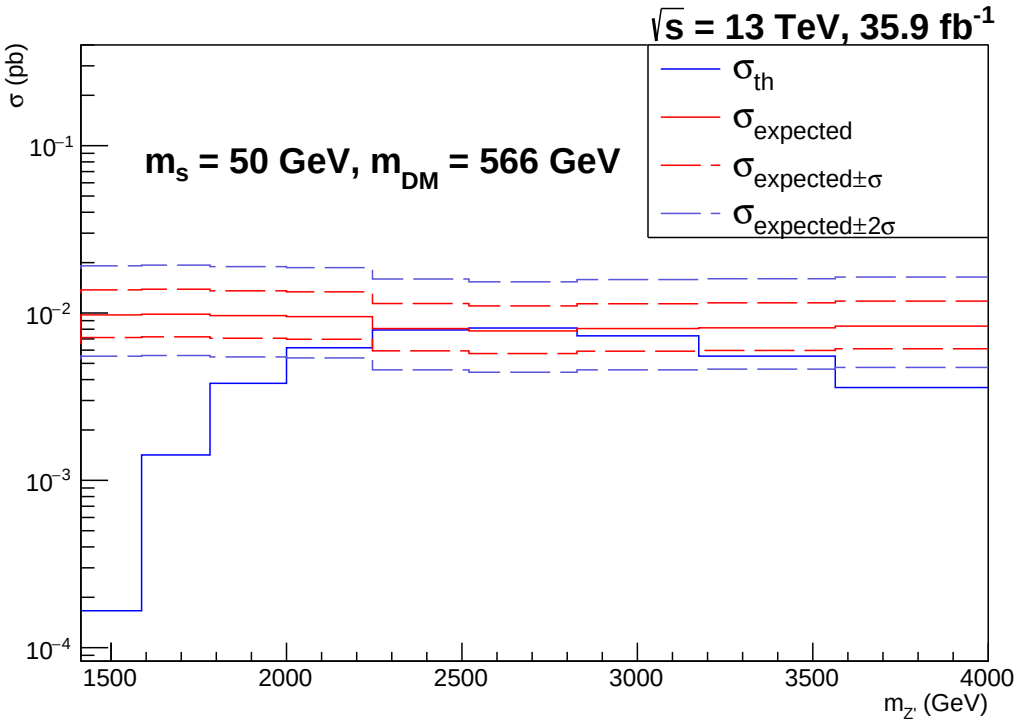

Figure A.6: Expected 95% CL limits for $m_s = 50$ GeV, $g_x < (4\pi)^{1/2}$and $g_q = 0.25$ with $m_{\mathrm{DM}} = 566$ GeV.

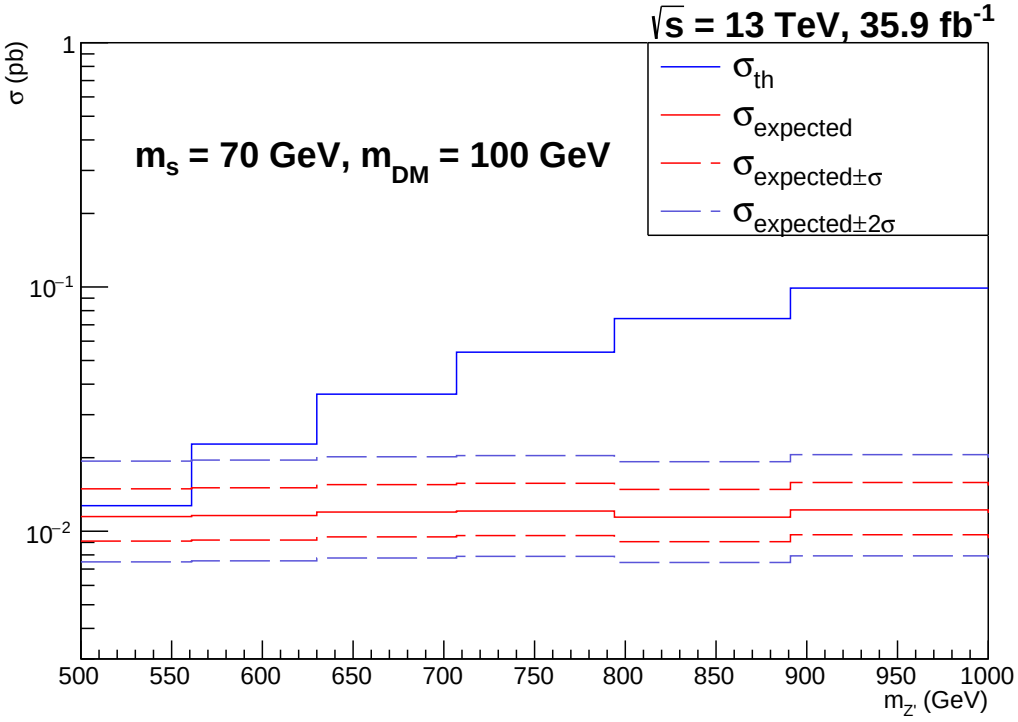

Figure A.7: Expected 95% CL limits for $m_s = 70$ GeV, $g_x < (4\pi)^{1/2}$ and $g_q = 0.25$ with $m_{\mathrm{DM}} = 100$ GeV.

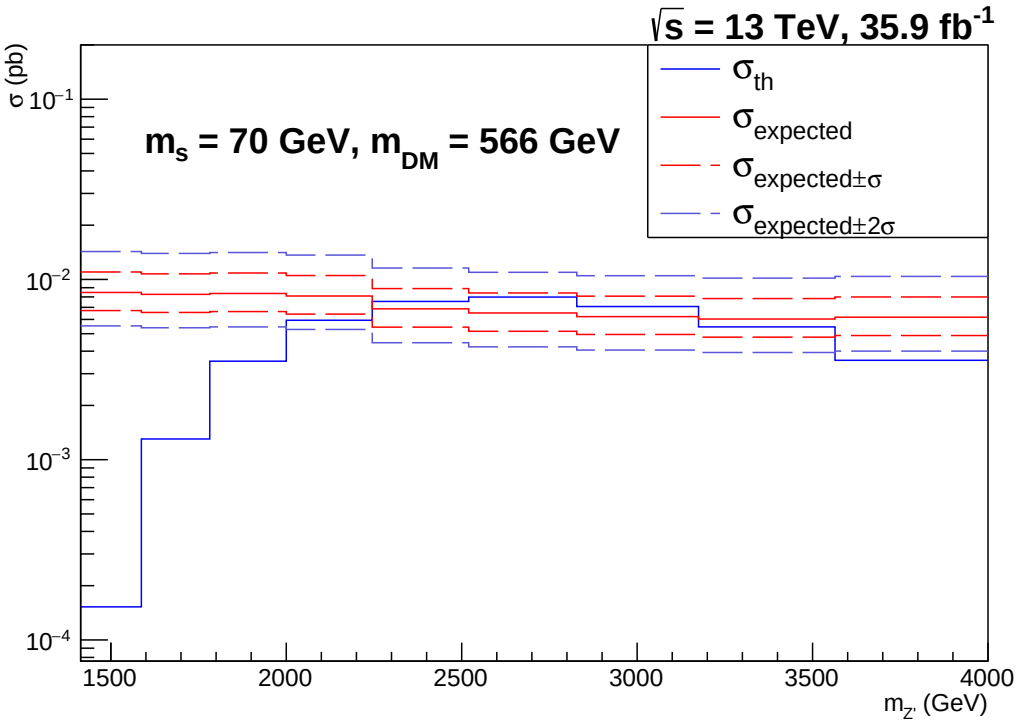

Figure A.8: Expected 95% CL limits for $m_s = 70$ GeV, $g_x < (4\pi)^{1/2}$ and $g_q = 0.25$ with $m_{\mathrm{DM}} = 566$ GeV.

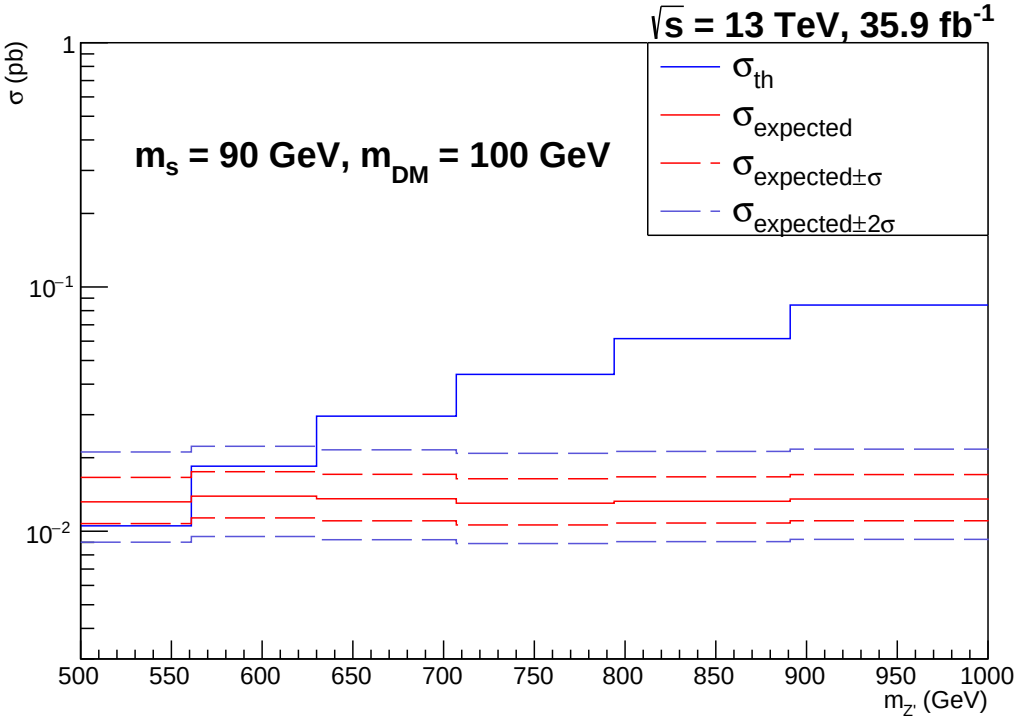

Figure A.9: Expected 95% CL limits for $m_s = 90$ GeV, $g_x < (4\pi)^{1/2}$ and $g_q = 0.25$ with $m_{\mathrm{DM}} = 100$ GeV.

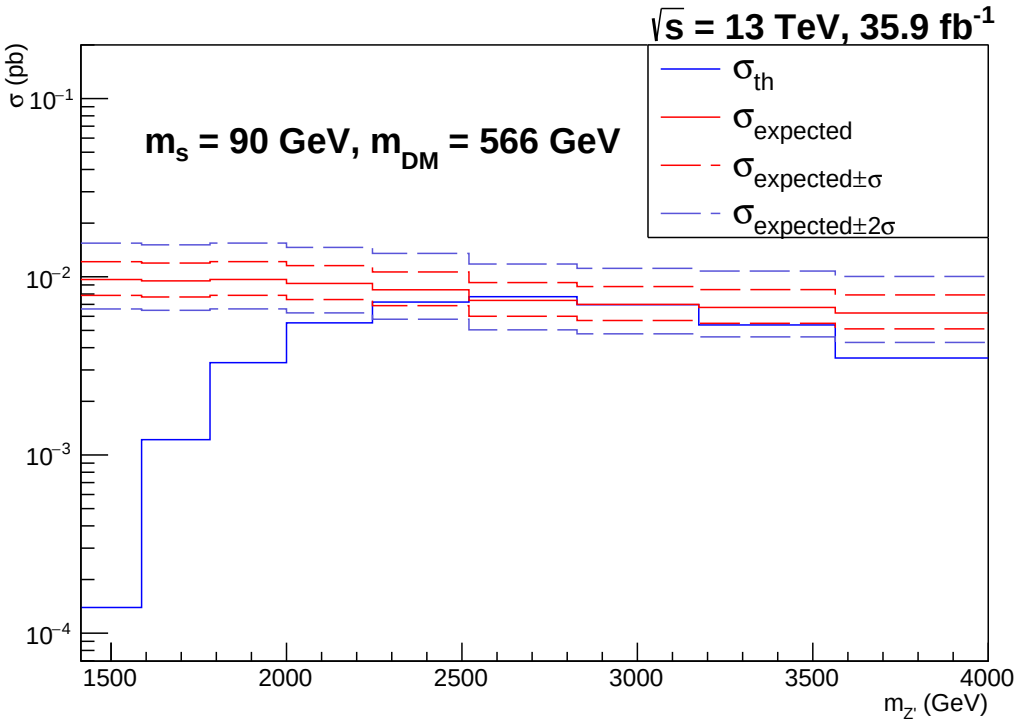

Figure A.10: Expected 95% CL limits for $m_s = 90$ GeV, $g_x < (4\pi)^{1/2}$ and $g_q = 0.25$ with $m_{\mathrm{DM}} = 566$ GeV.

B Exclusion limits at fixed m_{DM} for different signal samples according to the α_T multi-jet search

Figure B.1 to Figure B.4 are from signals with $m_s = 50$ GeV, $g_x = 1$ and $g_q = 0.25$. Figure B.5 to Figure B.8 are from signals with $g_x < (4\pi)^{1/2}$ and $g_q = 0.25$.

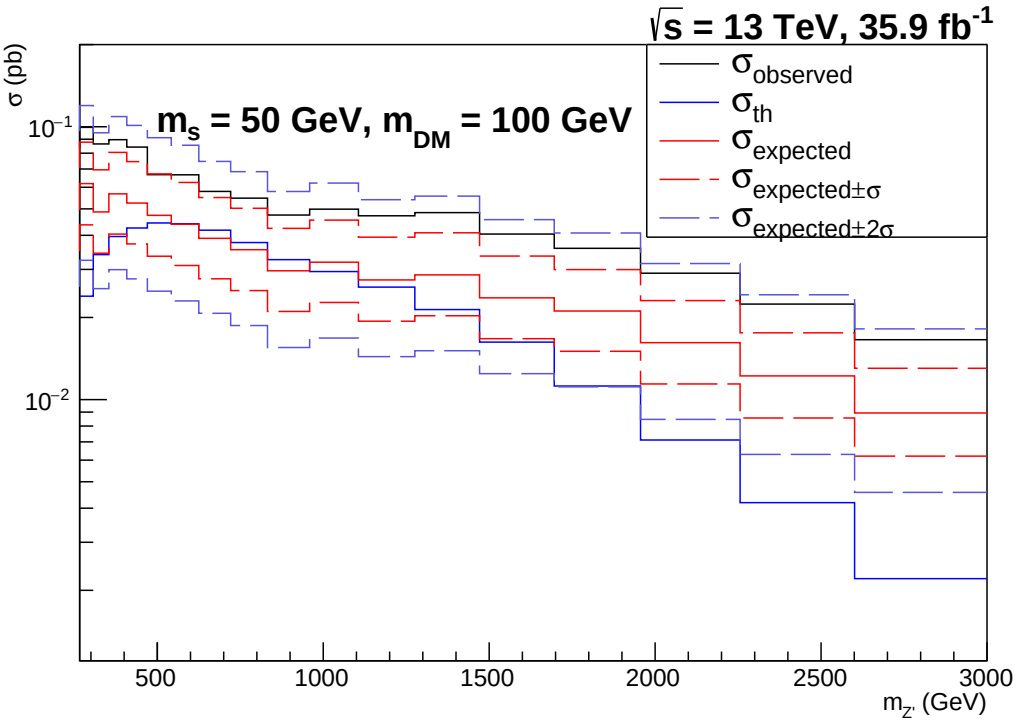

Figure B.1: Expected and observed 95% CL limits for $m_s = 50$ GeV, $g_x = 1.0$ and $g_q = 0.25$ with $m_{\mathrm{DM}} = 100$ GeV.

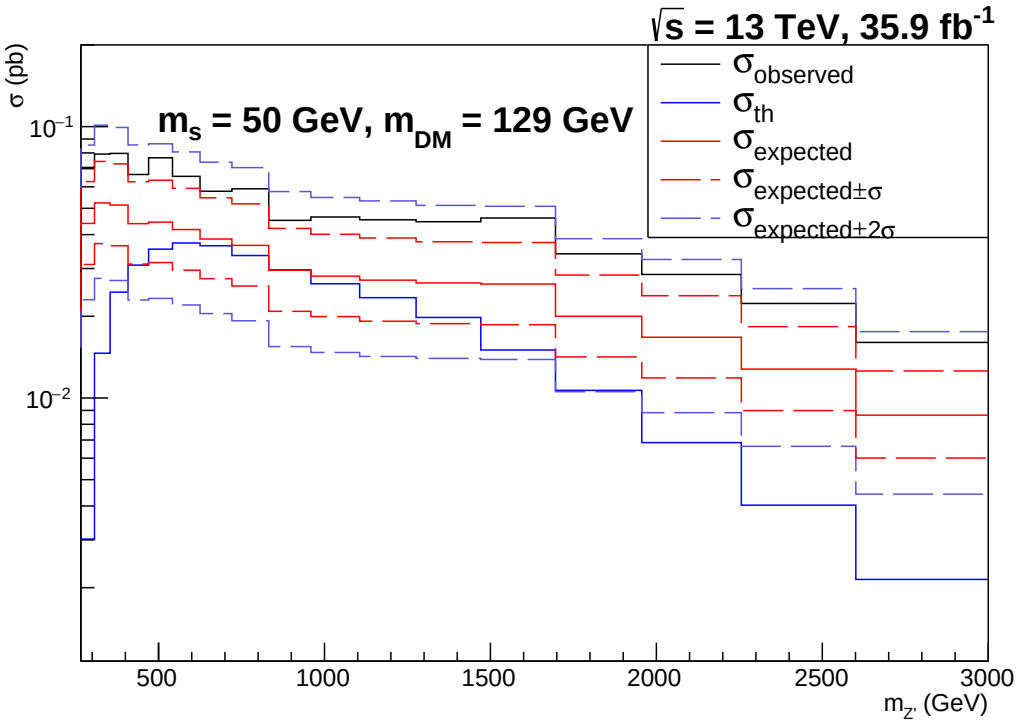

Figure B.2: Expected and observed 95% CL limits for $m_s = 50$ GeV, $g_x = 1.0$ and $g_q = 0.25$ with $m_{\mathrm{DM}} = 129$ GeV.

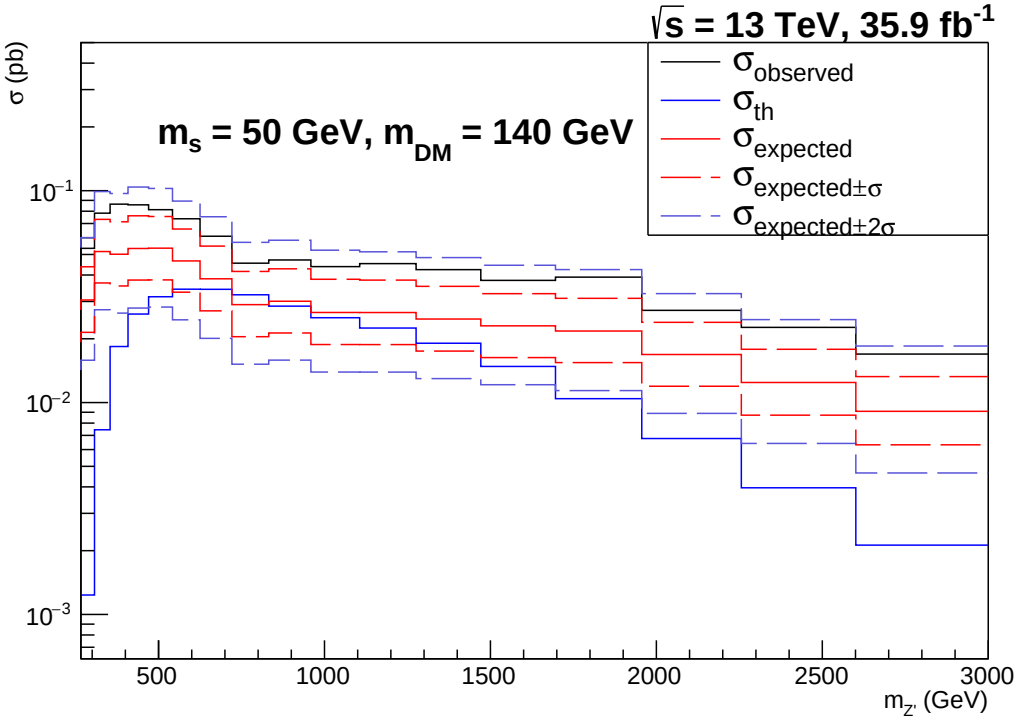

Figure B.3: Expected and observed 95% CL limits for $m_s = 50$ GeV, $g_x = 1.0$ and $g_q = 0.25$ with $m_{\mathrm{DM}} = 140$ GeV.

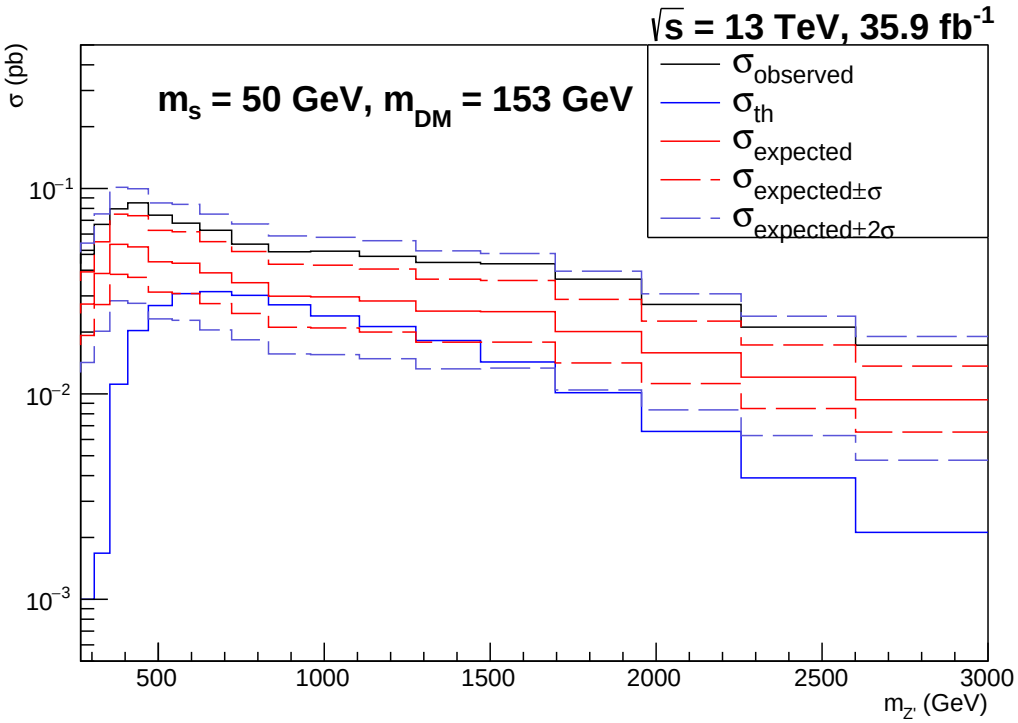

Figure B.4: Expected and observed 95% CL limits for $m_s = 50$ GeV, $g_x = 1.0$ and $g_q = 0.25$ with $m_{\mathrm{DM}} = 153$ GeV.

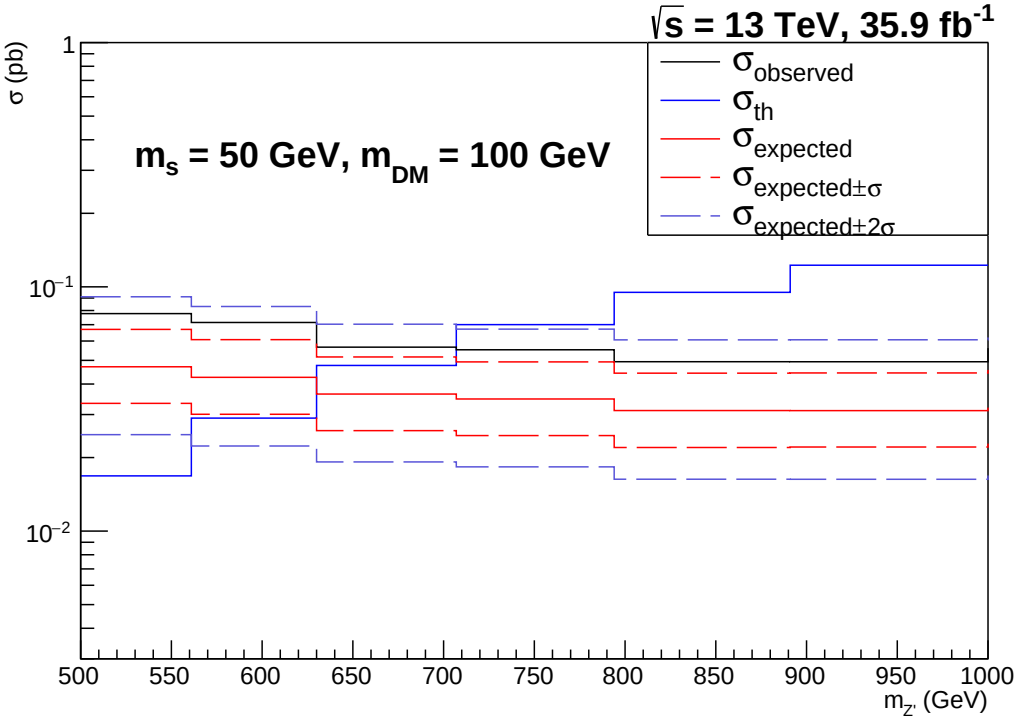

Figure B.5: Expected and observed 95% CL limits for $m_s = 50$ GeV, $g_x < (4\pi)^{1/2}$ and $g_q = 0.25$ with $m_{\mathrm{DM}} = 100$ GeV.

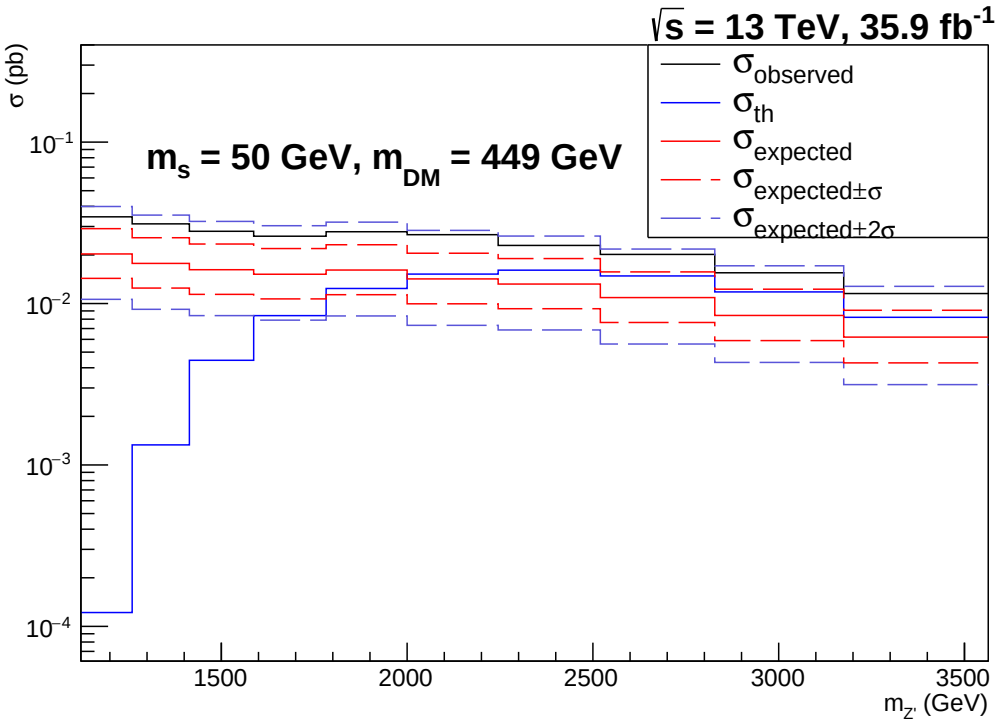

Figure B.6: Expected and observed 95% CL limits for $m_s = 50$ GeV, $g_x < (4\pi)^{1/2}$and $g_q = 0.25$ with $m_{\mathrm{DM}} = 449$ GeV.

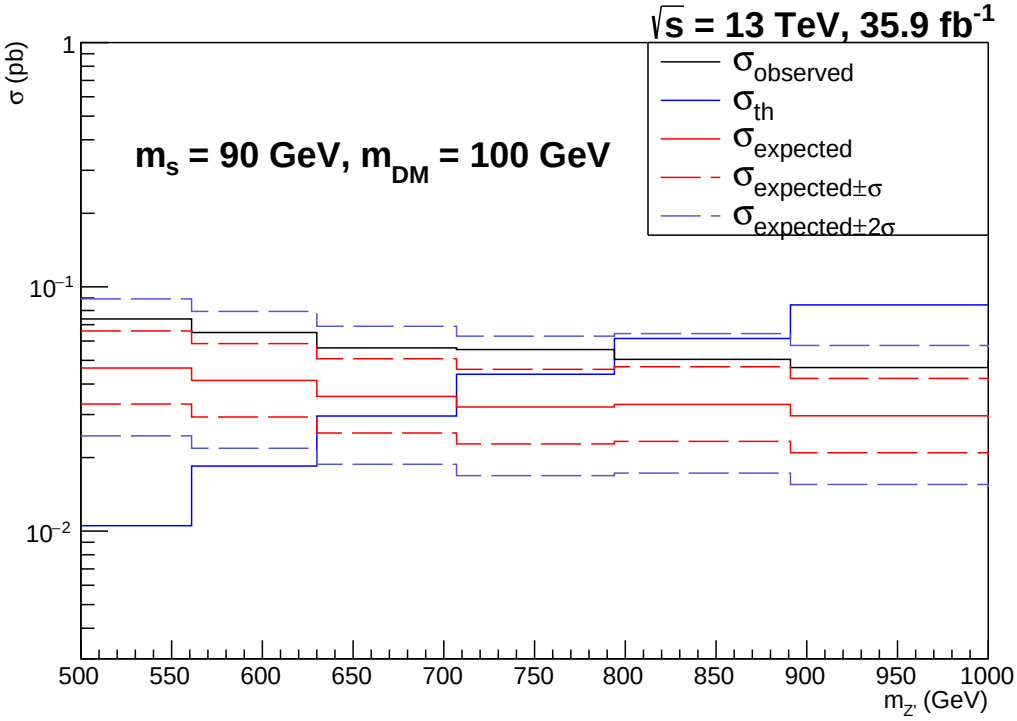

Figure B.7: Expected and observed 95% CL limits for $m_s = 90$ GeV, $g_x < (4\pi)^{1/2}$ and $g_q = 0.25$ with $m_{\mathrm{DM}} = 100$ GeV.

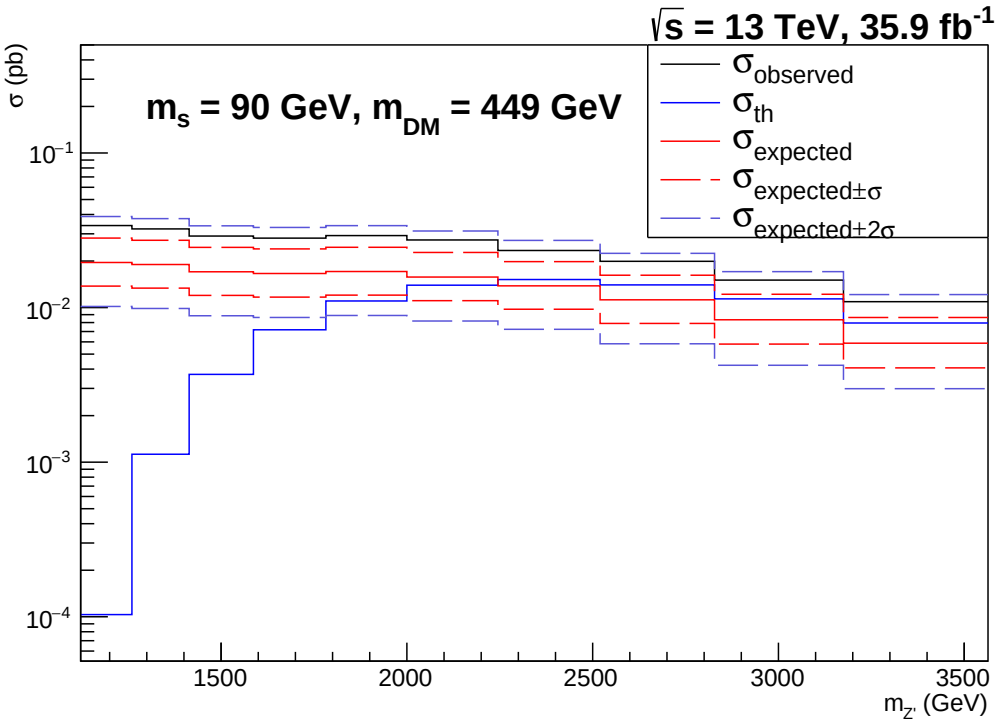

Figure B.8: Expected and observed 95% CL limits for $m_s = 90$ GeV, $g_x < (4\pi)^{1/2}$ and $g_q = 0.25$ with $m_{\mathrm{DM}} = 449$ GeV.